Stony Brook University

DEFECT STRUCTURES AND GROWTH MECHANISMS OF $B_{12}As_2$ EPILAYERS GROWN ON 6H-SiC AND 15R-SiC SUBSTRATES

A Dissertation Presented

by

Hui Chen

to

The Graduate School

in Partial Fulfillment of the

Requirements

for the Degree of

Doctor of Philosophy

in

Materials Science and Engineering

Stony Brook University

December 2008

Stony Brook University

The Graduate School

Hui Chen

We, the dissertation committee for the above candidate for the

Doctor of Philosophy degree, hereby recommend

acceptance of this dissertation.

Michael Dudley – Dissertation Advisor
Professor, Department of Materials Science and Engineering
Stony Brook University

Jonanthan C. Sokolov – Chairperson of defense
Professor, Department of Materials Science and Engineering
Stony Brook University

Yimei Zhu
Ph.D., Senior Scientist, Center for Functional Nanomaterials
Brookhaven National Laboratory

Lijun Wu
Ph.D., Science Associate, Department of Condensed Matter Physics and Materials Science
Brookhaven National Laboratory

This dissertation is accepted by the Graduate School

Lawrence Martin
Dean of the Graduate School

Abstract of the Dissertation

Defect Structures and Growth Mechanisms of $B_{12}As_2$ Epilayers Grown on 6H-SiC and 15R-SiC Substrates

by

Hui Chen

Doctor of Philosophy

in

Materials Science and Engineering

Stony Brook University

2008

$B_{12}As_2$ possesses the extraordinary properties, such as wide bandgap of 3.47eV and unique 'self heal' ability from electron irradiation damage, which make it attractive for the applications in space electronics, high temperature semiconductors and in particular, beta cells, devices capable of producing electrical energy by coupling a radioactive beta emitter to a semiconductor junction. Due to the absence of native substrates, $B_{12}As_2$ has been grown on substrates with compatible structural parameters via chemical vapor deposition. To date, growth on Si with (100), (110) and (111) orientation and (0001) 6H-SiC has been attempted. However, structural variants, including rotational and translational variants, have been observed in the epilayers and are expected to have a detrimental effect on device performance which has severely hindered progress of this material to date. In addition, none of the earlier reports provide a detailed atomic level study of defect structures in the films and growth mechanisms remain obscure. The focus of this thesis is to study defect structures in $B_{12}As_2$ films grown on different SiC substrates using synchrotron x-ray topography, high resolution transmission microscopy as well as other characterization techniques. The goals of the studies are to understand the generations of the defects present in $B_{12}As_2$ films and their growth mechanisms so as to develop strategies to reduce defect densities and obtain better film quality for future device fabrication. The following detailed studies have been carried out:

1) The microstructures in $B_{12}As_2$ epitaxial layers grown on on-axis c-plane (0001) 6H-SiC substrates were analyzed in detail. Synchrotron white beam X-ray topography (SWBXT) and scanning electron microscopy (SEM) revealed a mosaic structure consisting of a solid solution of twin and matrix epilayer domains. The epitaxial relationship was determined to be $(0001)_{B12As2}<11\bar{2}0>_{B12As2}||(0001)_{6H\text{-}SiC}<11\bar{2}0>_{6H\text{-}SiC}$.

$B_{12}As_2$ twinned domains were found in the epilayer and the twin relationship consisted of a 180° rotation about $[0001]_{B12As2}$. High resolution transmission electron microscopy (HRTEM) observation revealed an evolution of the film microstructure from an ~200nm thick disordered mosaic transition layer to a more ordered structure. Observing the structural projections of the film lower surface and the substrate upper surface, generated by CaRine 4.0 crystal visualization software, eight possible nucleation sites were found to be available on the substrate surface by considering the stable bonding configurations between the boron triangles at the bottom of the boron icosahedra, and the Si dangling bonds on the Si oriented (0001) 6H-SiC substrate surface. The transition layer was suggested to arise from the coalescence of translationally and rotationally variant domains nucleated at the various nucleation sites on the (0001) 6H-SiC surface. Boundaries between translationally variant domains were shown to have unfavorable high-energy bonding configurations while the formation of a $1/3[0001]_{B12As2}$ Frank partial dislocation enabled elimination of these high energy boundaries during mutual overgrowth. In consequence, the film quality beyond thicknesses of ~200nm can be improved as the translational variants grow out leaving only the twin variants. (0003) twin boundaries in the regions beyond 200nm are shown to possess fault vectors such as $1/6[\bar{1}100]_{B12As2}$ which originates from the mutual shift between the nucleation sites of the respective domains.

2) The effect off-cut angle on substrate surface on the growth of $B_{12}As_2$ epitaxial layer was studied using a 3.5° off-cut (0001) 6H-SiC substrate. A combined characterized technique composed of SWBXT, SEM, conventional and HRTEM was employed. Similar to the growth on on-axis c-plane 6H-SiC, the epitaxial relationship is identified to be $(0001)_{B12As2}<11\bar{2}0>_{B12As2}||(0001)_{6H\text{-}SiC}<11\bar{2}0>_{6H\text{-}SiC}$. It is also revealed that the epilayer consists of a solid solution of $B_{12}As_2$ twinned domains. The 3.5° off-cut angle breaks the surface symmetry of c-plane 6H-SiC, however, the width of each single terrace is large enough to provide eight possible nonequivalent nucleation sites for the growth of $B_{12}As_2$. In consequence, there could be eight possible structural variants in the film which indicates that the 3.5° offcut angle has little effect in the reduction of possible structural variants in the epilayer and thus may not be an excellent substrate to grow high quality $B_{12}As_2$ film.

3) Investigation of the microstructures of $B_{12}As_2$ epitaxial layers grown on m-plane 6H-SiC substrates has been studied. A mosaic structure formed by six types of domains, including (1-21) $B_{12}As_2$, (2-12) $B_{12}As_2$, (353) $B_{12}As_2$ and their respective {111} twins, was found in the epilayer. The choice of the various growth orientations in the $B_{12}As_2$ film were proposed to arise from the following factors: (1) the tendency for $B_{12}As_2$ to grow with {1-21} low energy surface facets; (2) the tendency to minimize the in-plane lattice mismatch between $B_{12}As_2$ planes oriented approximately parallel to the SiC (0001) planes so as to alleviate local strain in the film/substrate interface; (3) the tendency to nucleate on 3-3 symmetric closed-packed atomic steps exposed on the substrate surface after hydrogen etching.

4) Epitaxial growth of single crystalline $B_{12}As_2$ was discovered and investigated on m-plane 15R-SiC inclusions in a 6H-SiC substrate wafer. SEM showed only one type

of triangular feature on the smooth surface of the film which indicated single growth orientation of $B_{12}As_{2.}$ This is confirmed by SWBXT and cross-sectional HRTEM which revealed untwinned (353) orientated $B_{12}As_2$, with significantly improved macroscopic properties as confirmed by Raman spectroscopy. The corresponding growth model involving the bonding configuration between the film and the substrate was developed. It was found that the choice of the unique film orientation substantially resulted from the tendency to nucleate in $(111)_{B12As2}$ orientation on $(474)_{15R\text{-}SiC}$ close-packed facets that are exposed on the m-plane 15R-SiC surface. This indicates that m-plane 15R-SiC could be a potentially excellent substrate to grow high quality $B_{12}As_2$ for future device fabrication.

Dedicated to

My lovely parents

我可爱的父母

Table of Contents

List of Acronyms

As	arsenic
B	boron
C	carbon
CVD	chemical vapor deposition
HRTEM	high-resolution transmission microscopy
FPD	frank partial dislocation
SAD	selective area diffraction
SEM	scanning electron microscope
SF	stacking fault
Si	silicon
SWBXT	synchrotron white beam X-ray topography
TB	twin boundary
TEM	transmission electron microscope
XRT	X-ray topography

List of Symbols

A	site A in the ABC layered structure
B	site B in the ABC layered structure
C	site C in the ABC layered structure
d	lattice spacing of crystallographic plane
f	focus condition in HRTEM
m	symmetry of 2D point with a mirror plane

List of Figures

List of Tables

Acknowledgments

First I would like to give my deep and sincere gratitude to Prof. Michael Dudley, my Ph.D. advisor, for providing me this great opportunity to work in the field of crystal characterization. His wide knowledge and helpful guidance have been of great value for me. No doubt his understanding, encouragement and personal guidance have always been providing an excellent basis for my Ph.D. research.

Second, I would like to thank my lovely parents for their strong support throughout my Ph. D study. Without them, I would not have been able to complete my graduate studies.

I would like to thank Prof. Jonathan Sokolov, for being one of my defense committee members.

I would thank Dr. Yimei Zhu and Dr. Lijun Wu for being my defense committee members and their invaluable help on HRTEM simulation. And thanks to Dr. Lihua Zhang and Dr. Dong Su for their great help on HRTEM sample preparation and imaging.

I would like to thank Prof. James H. Edgar for supplying useful samples and instructive discussion on the epitaxial growth of $B_{12}As_2$. Thanks are also given to Prof. Martin Kuball for his collaboration in measuring the optical properties of $B_{12}As_2$ samples.

I would also like to thank my colleagues: Dr. Yi Chen, Dr. Guan Wang, Dr. Balaji Raghothamachar, Dr. Jie Bai, Ms. Yu Zhang, Mr. Ning Zhang, Mr. Vishwanath Sakar, Mr. Guannan Chen, Mr. Shayan and Mr. Yingmin Wang for their help during my research.

Financial support from the National Science Foundation Materials World Network Program under Grant No.0602875 and by the Engineering and Physical Science Research Council (EPSRC) under Grant No. EP/D075033/1 under the NSF-EPSRC Joint Materials Program is acknowledged. The SWBXT was carried out at Stony Brook Topography Facility (Beamline X19C) at the National Synchrotron Light Source (NSLS), Brookhaven National Laboratory (BNL), which is supported by the U.S. Department of Energy (D.O.E.) under Grant No. DE-AC02-76CH00016. HRTEM was carried out (in part) at the Center for Functional Nanomaterials, BNL, which is supported by the U.S. Department of Energy, Division of Materials Sciences and Division of Chemical Sciences, under Contract No. DE-AC02-98CH10886.

Publications

1. **H. Chen,** Y. Zhang and M. Dudley *et al***,** "Twinning mechanism of $B_{12}As_2$ epitaxial layers grown on m-plane 6H-SiC", ***J. Appl. Phys.,*** (2008) (submitted)
2. **H. Chen,** G. Wang, Y. Zhu and M. Dudley *et al***,** "Single-crystalline $B_{12}As_2$ on m-plane (1-100)15R-SiC", ***Appl. Phys. Lett.,*** 92 (23), 231917 (2008)
3. **H. Chen,** G. Wang, Y. Zhu and M. Dudley *et al***,** "Single-crystalline $B_{12}As_2$ on m-plane (1-100)15R-SiC", ***Appl. Phys. Lett.,*** 92 (23), 231917 (2008)
4. **H. Chen,** G. Wang, Y. Zhu and M. Dudley *et al***,** "Defect structures in $B_{12}As_2$ epitaxial layers grown on (0001)6H-SiC", ***J. Appl. Phys.,*** 103 (12), 123508 (2008)
5. J. Pomeroy, M. Kuball and **H. Chen** *et al*, "An investigation of phonon decay in $B_{12}As_2$ by Raman scattering spectroscopy", ***J. Appl. Phys.,*** 103 (9), 093537 (2008)
6. **H. Chen,** G. Wang and M. Dudley *et al***,** "Characterization and growth mechanism of $B_{12}As_2$ epitaxial layers grown on (1-100) 15R-SiC", ***Mater. Res. Soc. Symp. Proc.,*** 1069-D08-03 (2008)
7. G. Dhanaraj, Y. Chen and **H. Chen** *et al*, "Chemical vapor deposition of silicon carbide epitaxial films and their defect characterization", ***J. Elec. Mater.,*** 136 (4), 332, (2007)
8. **H. Chen**, G. Wang and Y. Chen *et al*, "The formation mechanism of carrot defects in SiC epifilms", ***Mater. Res. Soc. Symp. Proc.,*** 911, 163 (2006)
9. **H. Chen**, B. Raghothamachar and W. Vetter *et al*, "Effects of defect types on the performance of devices fabricated on a 4H-SiC homoepitaxial layer", ***Mater. Res. Soc. Symp. Proc.,*** 911, 169 (2006)
10. G. Dhanaraj, Y. Chen and **H. Chen** *et al*, **"**Growth mechanism and dislocation characterization of silicon carbide epitaxial films**", *Mater. Res. Soc. Symp. Proc.,*** 911, 157 (2006)
11. Y. Chen, **H. Chen** and N. Zhang *et al*, "Investigation of low angle grain boundaries in hexagonal silicon carbide", ***Mater. Res. Soc. Symp. Proc.,*** 955, 261 (2006)
12. Y. Chen, G. Dhanaraj and **H. Chen** *et al*, "Chemical Vapor Deposition and Defect Characterization of Silicon Carbide Epitaxial Films", ***Mater. Res. Soc. Symp. Proc.,*** 891, 591 (2006)
13. J. C. Rojo, S. Liang and **H. Chen** *et al*, "Physical vapor transport crystal growth of ZnO", ***Proc. SPIE,*** 6122, 61220Q (2006)

14. **H. Chen,** N. Zhang and Y. Zhang *et al***,** "Formation mechanism of carrot defects in 4H-SiC homoepitaxial layers", ***Appl. Phys. Lett.,*** (2008) (submitted)

Fields of Study

This section summarizes my major research accomplishments. Defect structures and growth mechanisms of $B_{12}As_2$ epilayers on various SiC substrates have been studied in depth. Based on the numerous results obtained during my research, the most significant accomplishments which are expected to have the biggest impact on the crystal growth process and the need for defect density reduction as well as those constituting major contributions to techniques for characterization are summarized below.

1) HRTEM simulation along [11-20] zone axis has been performed on the films grown on different SiC substrates. Based on the observation from the growth on c-plane 6H-SiC, structural projections of $B_{12}As_2$ atomic structure have been accurately assigned to the projections in the HRTEM images. This enables the possible detailed investigation of defect analysis in the $B_{12}As_2$ films grown on the various types of SiC substrates at an atomic resolution and paves a way to gain deeper insight into the growth mechanisms of these films.

2) Detailed atomic level studies of defect structures in the $B_{12}As_2$ films on a series of SiC substrates have been carried out using the combined technique of Normaski optical microscopy, scanning electron microscopy, synchrotron white beam X-ray topography, conventional and high resolution transmission electron microscopy. Epitaxial relationships corresponding to the growth on different substrates have been unambiguously determined which provide the basis to study and compare the difference between the growth mechanisms on these substrates.

3) The effects of different substrates on the epitaxial growth have been studied in depth by generating structural projections of SiC and $B_{12}As_2$, utilizing the crystal visualization software, CaRine4.0. This provides guidance to searching for better substrates to obtain better film quality with less structural variants present in the film.

4) The growth mechanisms involving atomic bonding configurations in the $B_{12}As_2$ epilayers and $B_{12}As_2$/SiC interfaces on the various substrates have been proposed. For instance, for the growth on on-axis c-plane 6H-SiC, a model consisting of eight possible nonequivalent nucleation sites on the substrate surface has been proposed, which predicts a significantly less number of possible structural variants than the one from a model proposed in earlier work. This reduction in number of nucleation sites from our modified model has been illustrated by considering possible bonding configuration in the film/substrate interface.

5) Single crystalline growth on m-plane 15R-SiC inclusions embedded in an m-plane 6H-SiC wafer has been discovered. A model illustrating the atomic bonding configuration across the film/substrate interface has been constructed to interpret single growth orientation of $B_{12}As_2$ on the m-plane 15R-SiC. This shreds light on improving the film quality by choosing a potentially excellent substrate, such as m-plane 15R-SiC.

1. Introduction

1.1. Background of $B_{12}As_2$

The broad applications of wide bandgap semiconductors in high-power and high frequency electronics, short wavelength optoelectronics, and chemical, biological and radiation sensors has led to an explosion of research into SiC[1], AlN, GaN[2] and ZnO[3] etc. Thus far boron-based wide bandgap semiconductors have been almost completely ignored especially the icosahedral structure boron-rich compounds, such as α–boron (B_{12}), $B_{12}P_2$ and $B_{12+x}C_{3-x}$. These icosahedral borides with a rhombohedral structure hold a special place within chemistry and do not follow the general bonding rules[4]. They are composed of 12-atom clusters of boron atoms in which each boron atom resides on a vertex of an icosahedron. The internal bonding of the icosahedron is based on an electron-deficient three-center bonding scheme whereby two electrons are shared among three boron atoms. The excellent strength of the three-center bonds endows these icosahedral borides extraordinary strength and high melting temperatures.

$B_{12}As_2$ is a member of the icosahedral boride family based on clusters of boron atoms and two-atom As-As chains as shown in Fig. 1. It has a wide bandgap of 3.47eV[5] and high melting point of around 2027°C[6], which suggests it can be used as a very high-temperature semiconductor. It's also useful for devices operating in high electron radiation environments due to its self-healing resistance to radiation damage[4-11]. In addition, a unique potential application of $B_{12}As_2$ is for betavoltaic cell, a power device capable of directly producing electrical energy by coupling a radioactive beta emitter to a rectifying semiconductor junction[12-14]. Betavoltaic cells take advantage of the superior energy density available in nuclear decay compared to chemical sources and have potential for power cells with increased lifetimes, which are measured on a scale of years rather than days or weeks. For most of the beta cells, which have been made from Si and Ge, their lifetime may be short in that power output rapidly decreases associated with the accumulation of radiation damage[15]. Therefore, $B_{12}As_2$ with strong radiation hardness becomes a very attractive candidate for the application of beta cells. Further possibilities for this material include neutron detectors, as boron has a large neutron capture cross section of around 4000b, and also thermoelectric devices for converting waste heat into electricity[16, 17].

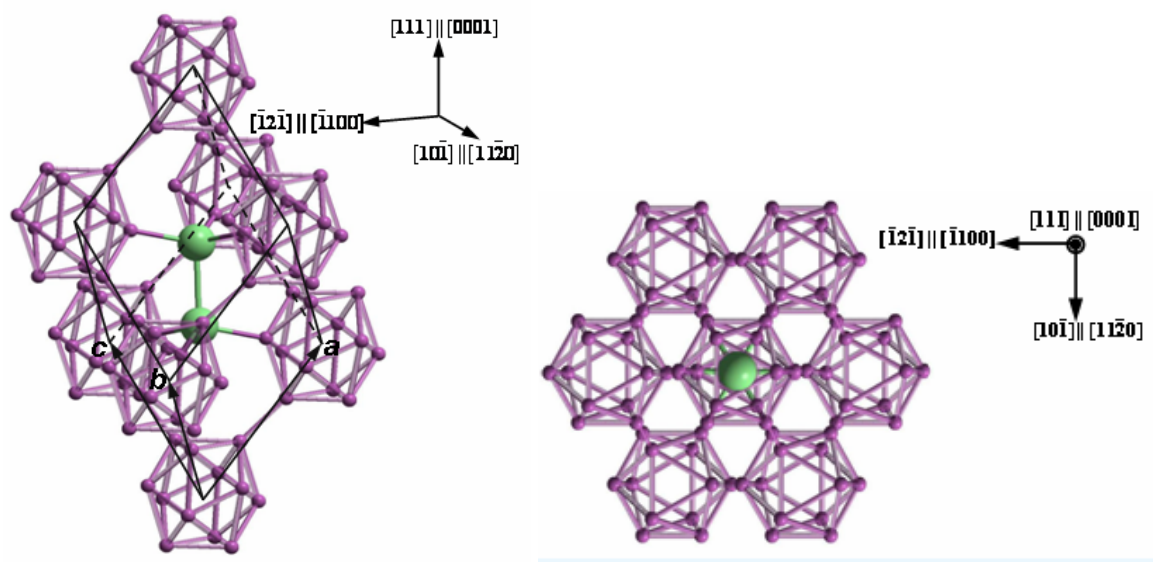

(a) (b)

Fig. 1 (a) Side view of $B_{12}As_2$ unit cell showing boron icosahedra (B atoms are the smaller spheres) and an As-As chain (As atoms are the larger spheres). The structure can be equivalently referred to either a rhombohedral or hexagonal unit cell. *a*, *b* and *c* indicate the rhombohedral unit cell axes. The [111], [$1\bar{2}1$] and [$10\bar{1}$] directions indicated, referred to the rhombohedral cell, are equivalent to [0001], [$1\bar{1}00$] and [$11\bar{2}0$], respectively, in the hexagonal cell. (b) Plan view of the structure of $B_{12}As_2$ unit cell.

The current absence of native substrates of $B_{12}As_2$ necessitates the growth of films by heteroepitaxy on lattice matched substrates. Epitaxial growth on Si substrates of various orientations has been attempted by Xu *et al*[18], but two or more growth orientations have been found which may have an adverse effect on the electrical properties of $B_{12}As_2$ films. Thus finding a more suitable substrate than Si has become an important factor to improve $B_{12}As_2$ film quality. Looking into the crystal structure of $B_{12}As_2$, though belonging to $\boldsymbol{R\bar{3}m}$ space group which is a type of rhombohedral structures, it can be represented with a hexagonal cell (a =0.615 nm, c=1.191 nm). This observation suggests the potential for heteroepitaxial growth of $B_{12}As_2$ on a surface that also possesses hexagonal symmetry. Recently, epitaxial growth on 6H-SiC is facilitated since the room-temperature in-plane lattice parameters of (0001) 6H-SiC (a=0.308 nm, c =1.51 nm) are approximately one half those of (0001) $B_{12}As_2$ (Fig. 2) and there are a number of reports of epitaxial films grown on such substrates[7, 12, 13, 19].

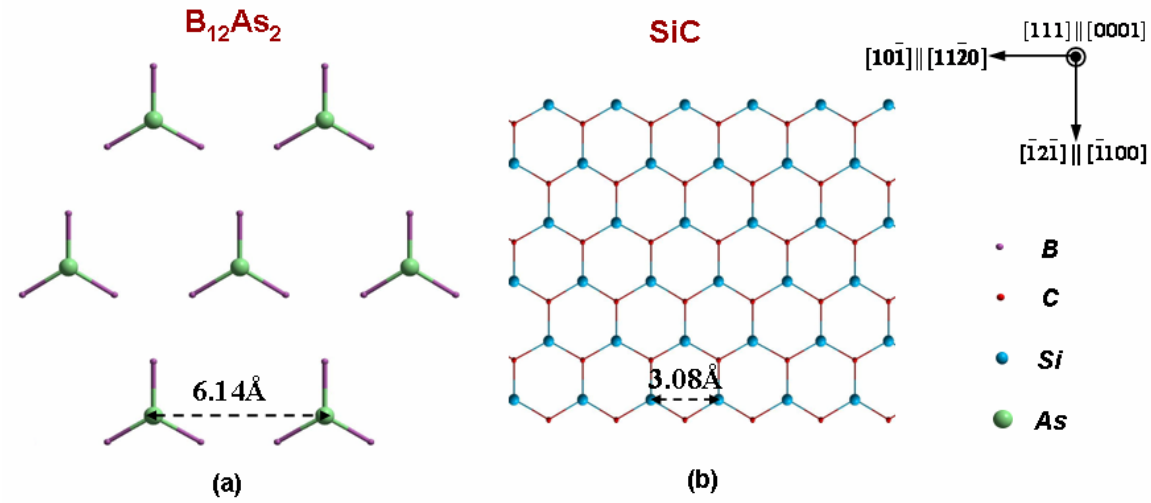

Fig. 2 Plan view of (0001) $B_{12}As_2$ surface and (0001) 6H-SiC surface. The in-plane lattice mismatch between the two materials is around 0.3%.

For films grown on 3.5° off-axis and on-axis (0001) 6H-SiC. Wang *et al* observed polycrystalline grains with preferred orientation of $[0001]_{B12As2}//[0001]_{6H\text{-}SiC}$ and $[10\bar{1}0]_{B12As2}//[10\bar{1}0]_{6H\text{-}SiC}$ [12]. Vetter *et al* confirmed this orientation relationship for films grown on on-axis substrates although double positioning twins were also observed with one occurring more frequently than the other[13]. R. Nagarajan *et al* found that the distribution of double positioning twins varied with different AsH_3:B_2H_6 flow ratios[19]. Michael *et al* theoretically predicted the existence of a number of possible $B_{12}As_2$ structural variants based on the variety of non-equivalent nucleation sites available on the (0001) SiC surface. These were referred to as chemical, translational and rotational variants although this analysis did not take into account the influence of the possible bonding configurations between the $B_{12}As_2$ and the SiC surface, a subject which will be addressed in Chapter 3. Double positioning twins were observed but no evidence was found for any preferred growth. Diffuse boundaries observed within the twin grains were tentatively interpreted as boundaries between translational variants. In addition, a boron carbide reaction layer was observed between the $B_{12}As_2$ layer and the 6H-SiC substrate[7]. In the field of device fabrication, a beta cell having a semiconductor junction that incorporates $B_{12}As_2$ film on 6H-SiC substrate (Fig. 3) has been developed by Aselage *et al*[Error! Bookmark not defined.], but the presence of twin boundaries may impede and even preclude the growth of semiconductor quality films of $B_{12}As_2$.

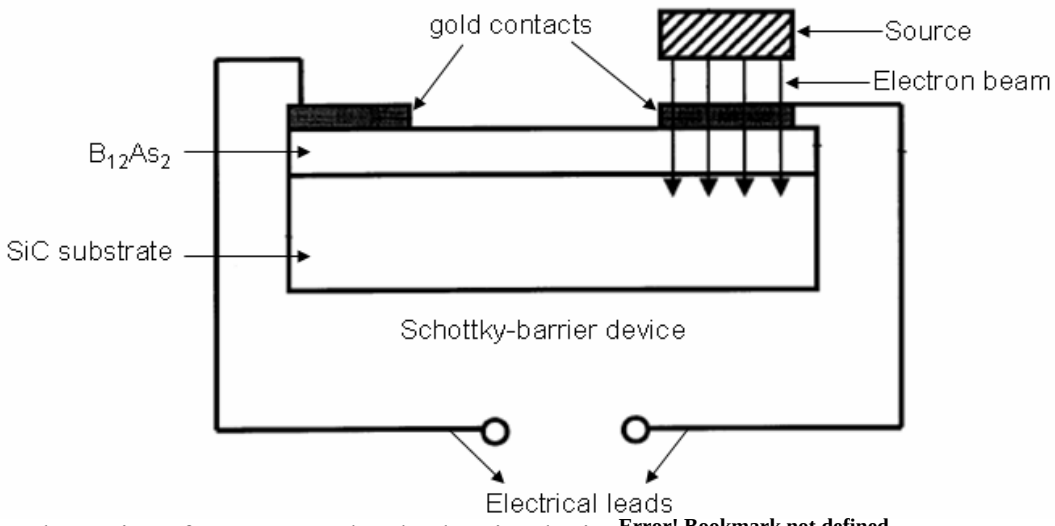

Fig. 3 Schematics of a $B_{12}As_2$ Schottky-barrier device**Error! Bookmark not defined.**.

1.2. Motivation

As discussed above, for the growth of $B_{12}As_2$ on Si with (100), (110) and (111) orientation and c-plane (0001) 6H-SiC, rotational and translational variants were both predicted and observed. According to our previous work on 4H-SiC Schottky diodes, defects associated with rotational and translational variants would deteriorate electrical properties of devices (Appendix I). To avoid the presence of these variants which may largely degrade device performance, it is necessary to study the formation mechanisms of the defects in the $B_{12}As_2$ films. However, none of the earlier reports provide a detailed atomic level study of defect structures in epitaxially grown $B_{12}As_2$. Thus the primary motivation for our research in this area is to investigate the defect structures and explore growth mechanisms of $B_{12}As_2$ grown on various SiC substrates on an atomic scale, which may shred light on the development of strategies to minimize the densities of the defects so as to grow high quality single crystalline $B_{12}As_2$ films and reduce the adverse effects of the defects on device performance.

2. Investigation methods

In the present work, the combined use of Normaski optical microscopy, SWBXT, SEM, HRTEM and CaRine4.0 crystal modeling software has been employed for the characterization of defect structures in $B_{12}As_2$ films and the investigation of growth mechanisms on different substrates.

2.1. Normaski optical microscopy

Nomarski optical microscopy is a convenient method to observe unstained and transparent samples by offering differential interference contrast. Compared to traditional optical microscopy, it works on the principle of interferometry to gain information about the optical density of the sample. The enhanced contrast gives the appearance of a three-dimensional physical relief corresponding to the variation of optical density of the sample, emphasising lines and edges. In this work, Normaski optical microscopy is used to observe the defect features on the surfaces of the $B_{12}As_2$ epilayers grown on different SiC substrates.

2.2. SWBXT

With its high strain sensitivity, high intensity, suitable spatial resolution and broad spectral range, synchrotron white beam X-ray topography (SWBXT) has been a powerful non-destructive tool to macroscopically investigate the crystallographic orientations and defect structures of various crystals, such as SiC[20-23]. Basically, there are three types of SWBXT techniques, consisting of back reflection, transmission and grazing incidence geometries. In this work, two types of SWXBT, transmission mode and grazing incidence mode, are utilized to determine the film/substrate epitaxial relations for the studied samples. For transmission mode SWBXT, the X-ray film is placed behind the sample to record the diffraction pattern as shown in Fig. 4(a). The recorded diffraction patterns contain the information from both substrate and the epilayer. In grazing incidence geometry, the x-ray recording film is hanged closely parallel to the lightly tilted sample surface, as illustrated in Fig. 4(b). With the tilting angle, this geometry increases the x-ray penetration length and meanwhile reduces the x-ray penetration depth. As a result, the recorded information is mostly from the near-surface regions. Consequently, grazing incidence topography is especially ideal to obtain accurate defect distribution in the epilayer and helps distinguish the defect information in the epilayer from that in the substrate.

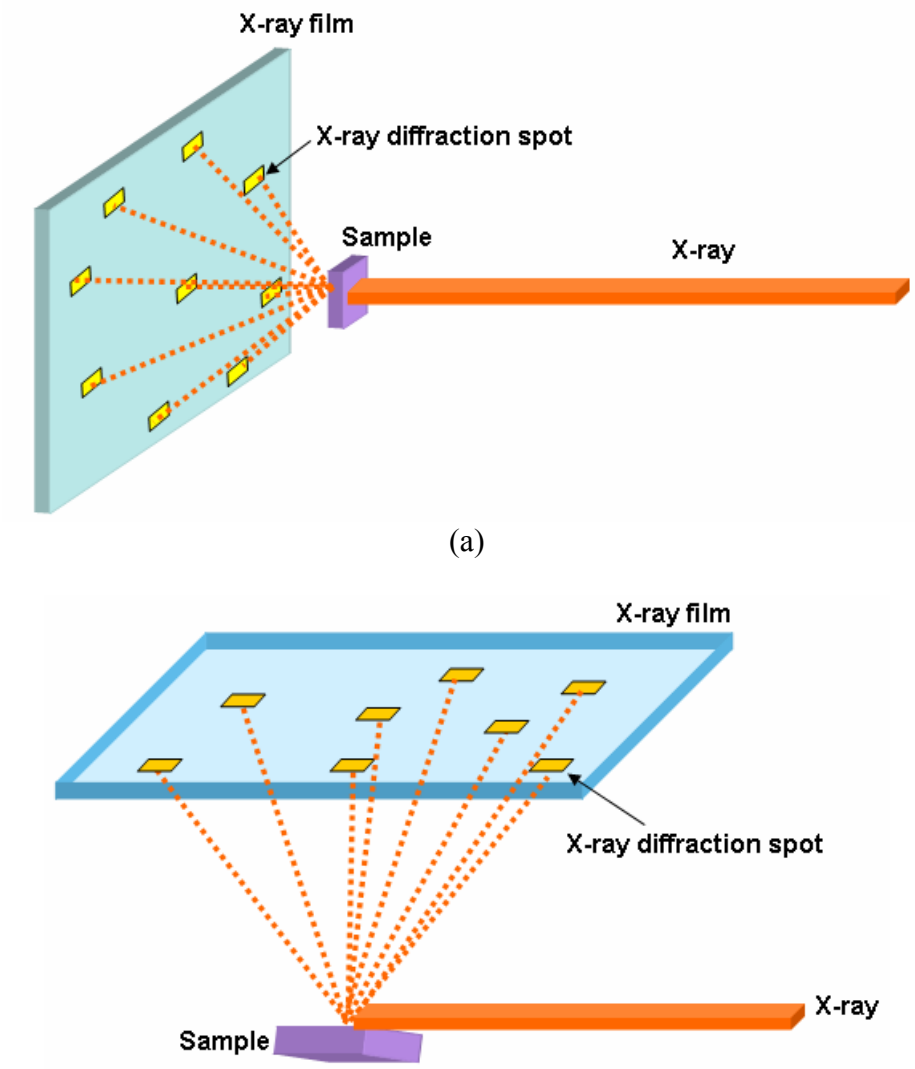

Fig. 4 Schematics of (a) transmission SWBXT and (b) grazing incidence SWBXT.

2.3. SEM

Scanning electron microscopy (SEM) is a type of electron microscopy methods, which images the sample surface by scanning it with a high-energy beam of electrons in a raster scan pattern. It offers a wide range of depth of field and is widely employed to observe sample surface. In this work, SEM is adopted to image the global surface morphologies of $B_{12}As_2$ films grown on different SiC substrates.

2.4. TEM

Transmission electron microscopy (TEM) is a microscopy technique whereby an electron beam passes through and interacts with an ultra thin specimen. It has been widely used in material science, especially in terms of developing images of crystals to study their

internal structures, interactions and defects. Among various TEM techniques, high resolution TEM (HRTEM) has become a critical imaging tool to understand material properties by studying material structures at the level of atomic resolution. In this work, all of the HRTEM observation has been done along [10-1] zone axis (equivalent to [11-20] in hexagonal system), from which $B_{12}As_2$ twin boundaries are expected to be well discerned according to the visualization obtained from CaRine4.0 crystal visualization software. In contrast, [1-21] (equivalent to [1-100] in hexagonal system) is not selected to be a viewing direction for HRTEM in that the projection of the $B_{12}As_2$ twin domains along [1-100] zone axis of $B_{12}As_2$ makes no difference so that $B_{12}As_2$ twin boundaries won't be able to be observed along this axis. The comparison between the crystal visualization projected from [11-20] and [1-100] is shown in Fig. 5(a)-(d).

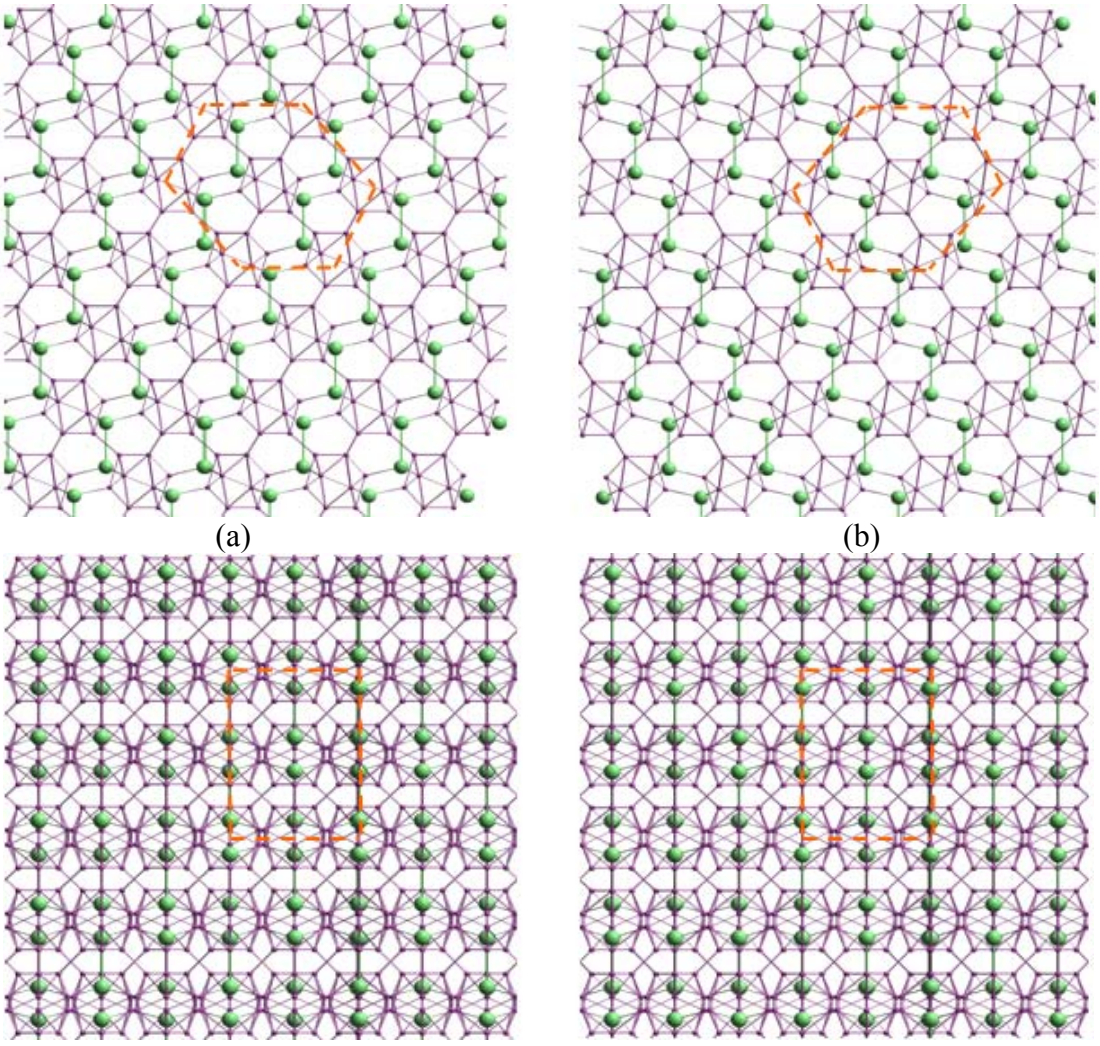

Fig. 5 Projection of $B_{12}As_2$ atomic structure viewed along $[1\bar{1}20]$ (Fig. (a)) and its twinned orientation [-1-120] (Fig. (b)) as well as [1-100] (Fig. (c)) and its twinned orientation, [-1100] (Fig. (d)).

2.5. CaRine Crystallography software

CaRine is a powerful crystallography software which has been developed since 1989 and more and more widely used for crystal visualization. It provides multiple flexible ways to generate structural projections of various crystals. In present work, the software is employed to generate crystal projections of $B_{12}As_2$ and SiC from various viewing directions, as exampled in Fig. 5(a)-(d).

2.6. TEM sample preparation

In this work, two methods are adopted for TEM sample preparation, which includes dimpling and T-tool wedge polishing. Fig. 6(a)-(e) shows the schematics of sample preparation for a TEM specimen. As shown in Fig. 6(a), the original sample wafer contains an epilayer (generally a few μm thick) grown on a substrate (a few hundred μm thick). Two pieces (~1.5mm x 1mm) are cut from the wafer (Fig. 6(b)) and then stuck with each other by putting each epilayer face to face via a very thin layer of TEM glue. Thus a cross-sectional 'sandwich' is formed as shown in Fig. 6(c). After mechanical polishing using a set of TEM T-tool with a series of diamond lapping films, the thickness of the sandwich is reduced to ~3μm (Fig. 6(d)). Then the sample is further thinned via dimpling technique and ion mill. Finally a hole is generated in the center of the sandwich. Regions around the hole have thicknesses of less than 30nm and are highly electron transparent to be ideally used for HRTEM imaging (Fig. 6(e)).

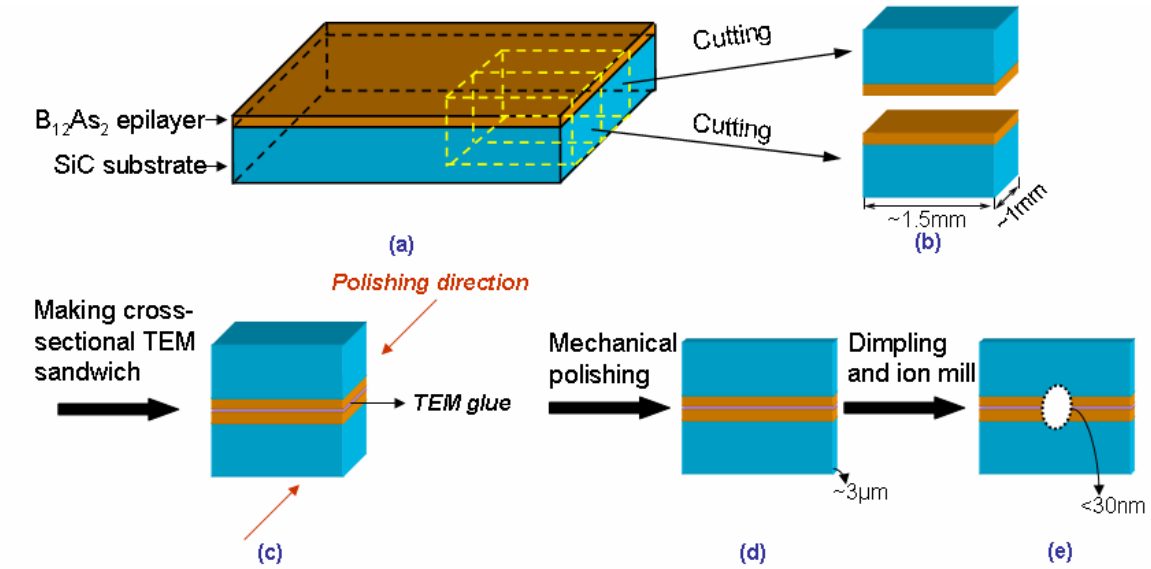

Fig. 6 TEM sample preparation procedures.

3. $B_{12}As_2$ grown on on-axis c-plane (0001)6H-SiC

3.1. Outline

A detailed analysis of the microstructure in $B_{12}As_2$ epitaxial layers grown by CVD on (0001) 6H-SiC substrates is presented. Synchrotron white beam x-ray topography (SWBXT) enabled macroscopic characterization of the substrate/epilayer ensembles and revealed the presence of a quite homogenous solid solution of twin and matrix epilayer domains forming a submicron mosaic structure. The basic epitaxial relationship was found to be $(0001)_{B12As2}<1\bar{1}20>_{B12As2}||(0001)_{6H\text{-}SiC}<1\bar{1}20>_{6H\text{-}SiC}$ and the twin relationship comprised a 180° (or equivalently 60°) rotation about $[0001]_{B12As2}$ in agreement with previous reports. Cross-sectional high resolution transmission electron microscopy (HRTEM) revealed the presence of an ~200nm thick, disordered transition layer which is shown to be created by the coalescence of a mosaic of translationally and rotationally variant domains nucleated at the various types of nucleation site available on the (0001) 6H-SiC surface. In this transition layer, competition between the growth of the various domains is mediated in part by the energy of the boundaries created between them as they coalesce. Boundaries between translationally variant domains are shown to have unfavorable bonding configurations and hence high energy. These high energy boundaries can be eliminated during mutual overgrowth by the generation of a $1/3[0001]_{B12As2}$ Frank partial dislocation which effectively eliminates the translational variants. This leads to an overall improvement in film quality beyond thicknesses of ~200nm as the translational variants grow out leaving only the twin variants. (0003) twin boundaries in the regions beyond 200nm are shown to possess fault vectors such as $1/6[1\bar{1}00]_{B12As2}$ which are shown to originate from the mutual shift between the nucleation sites of the respective domains.

3.2. Introduction

Previous effort on CVD growth of $B_{12}As_2$ on c-plane (0001) 6H-SiC has observed rotational and translational variants in the epilayers[Error! Bookmark not defined.]. However, the formation mechanism of these structural variants, which could be vital to guide better crystal growth, has remained unclear. In addition, there has been no systematic analysis of the defect structures in the films at an atomic scale. In order to better understand the defect structure and growth mechanism which are helpful to find possible solutions to improving film quality, $B_{12}As_2$ films grown on c-plane (0001) 6H-SiC substrates are investigated.

3.3. Experimental

(0001) 6H-SiC substrates were used for the CVD growth of $B_{12}As_2$. The $B_{12}As_2$ films were synthesized with gaseous precursors of 1% B_2H_6 in H_2 and 2% AsH_3 in H_2. The films were deposited at 1450°C and 100 Torr of reactor pressure for 30 minutes. The rhombohedral epitaxial films of $B_{12}As_2$ had a nominal thickness of 3 μm. The cross-sectional TEM samples were made parallel to $(1\bar{1}20)_{6H\text{-}SiC}$, which is parallel to $(1\bar{1}20)_{B12As2}$, since this orientation clearly reveals the $B_{12}As_2$ twin boundaries. Note that indices referenced to the four index hexagonal system are utilized. These can easily be related to the three index rhombohedral system using the standard relationship such that $[1\bar{1}20]_{B12As2}$ is parallel to $[10\bar{1}]_{B12As2}$,

$[0001]_{B12As2}$ is parallel to $[111]_{B12As2}$, and $(0003)_{B12As2}$ is equivalent to $(111)_{B12As2}$ (see Fig. 1). The sample was mechanically thinned and polished using the standard T-tool technique employing 30 μm, 15 μm, 6 μm, 3 μm, 1 μm and 0.5 μm diamond lapping films and then ion milled to electron transparency. Conventional TEM observation was performed on a Philips CM12 transmission electron microscope with an accelerating voltage of 120KeV. High resolution TEM was carried out using a JEOL 3000EX system with an electron voltage of 300keV. SWBXT was performed on as-grown films at the Stony Brook synchrotron topography facility at the National Synchrotron Light Source. The white beam x-ray had wavelength spectrum ranging from 0.01Å to 2.00Å, in which the beam peak had a wavelength of 0.8 Å. The grazing incidence Laue patterns were recorded on Kodak SR5 x-ray film at a sample to film distance of 15cm. Structural projections were produced using the commercial software package CaRine 4.0.

3.4. Results and discussion

3.4.1. Optical microscopy, SWBXT and SEM results

Fig. 7 shows a grazing incidence synchrotron x-ray Laue pattern from a $B_{12}As_2$ epitaxial layer grown on a c-plane 6H-SiC substrate recorded with the epilayer nearly parallel to the X-ray beam. The $B_{12}As_2$ produced diffuse diffraction spots and detailed indexing analysis not only confirms the expected $(0001)_{B12As2}<1\bar{1}\bar{2}0>_{B12As2}||(0001)_{6H\text{-}SiC}<1\bar{1}\bar{2}0>_{6H\text{-}SiC}$ in epitaxial relationship[Error! Bookmark not defined., Error! Bookmark not defined.], but also shows that the $B_{12}As_2$ is present in two distinct orientations related by a 180^o twin (or equivalently 60^o) rotation about the $(0001)_{B12As2}$ plane normal. The strong, well-defined 6H-SiC diffraction spots are labeled with hexagonal *hkil* indices without subscripts while the more diffuse $B_{12}As_2$ spots are labeled with hexagonal *hkil* indices with subscripts of roman numerals *I* or *II* indicating matrix or twin orientation (in some cases the matrix and twin reflections coincide). Although the film completely covers the substrate, the area of the $B_{12}As_2$ diffraction spots appears different from that of the SiC spots due to the presence of mosaicity in the film. This leads to an overall divergence in the diffracted beams emanating from both the matrix and twin regions. The overall appearance of the $B_{12}As_2$ matrix and twin diffraction spots is consistent with a mosaic and quite homogenous solid solution of twin and matrix domains which are of a size that is below the spatial resolution of X-ray topography (a few microns). This was corroborated by Normaski optical observation (Fig. 8) and SEM (Fig. 9) which reveals a composite structure comprising two types of equilateral triangular feature, each with dimensions of several μm, which are mutually rotated by 180^o about the surface normal in agreement with previous observations[Error! Bookmark not defined.]. These triangular grains correspond to twin related $B_{12}As_2$ domains. The morphology of the triangular features was determined using orientation information provided by SWBXT and found to consist of a flat $(0001)_{B12As2}$ facet bounded by three equivalent $(1\bar{1}00)_{B12As2}$ facets. Further microstructural information, in particular concerning the boundaries between the various domains, was provided by conventional and HRTEM studies carried out on cross-sectional samples.

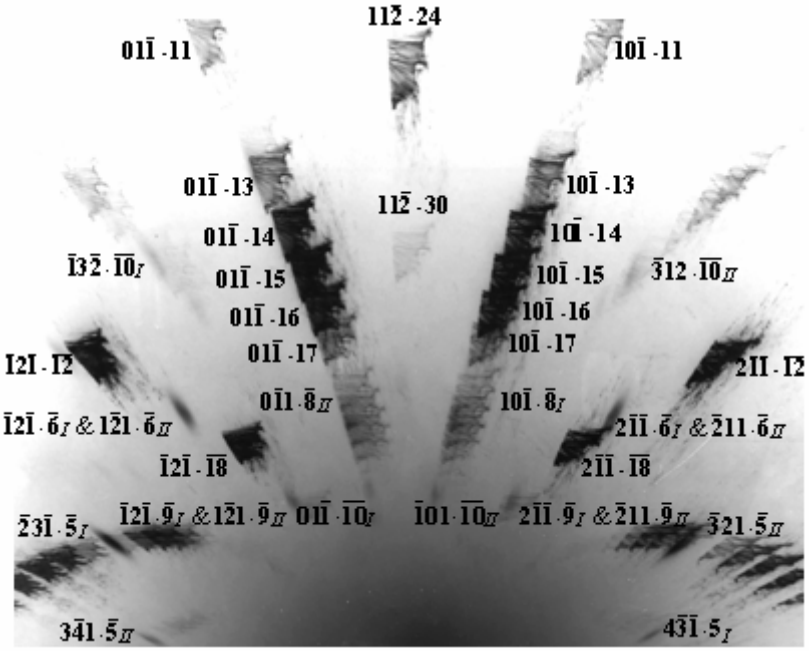

Fig. 7 Indexed grazing incidence SWBXT Laue pattern recorded from the $B_{12}As_2$ film grown on a c-plane 6H-SiC substrate.

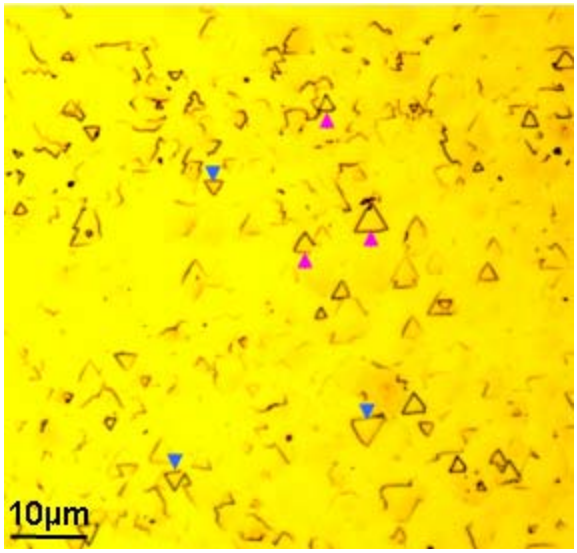

Fig. 8 Optical observation revealing two types of equilateral triangular features present on the surface of $B_{12}As_2$ film. The triangular features marked with blue arrows have an apex pointing downward while the ones marked with purple arrows have an apex pointing upwards.

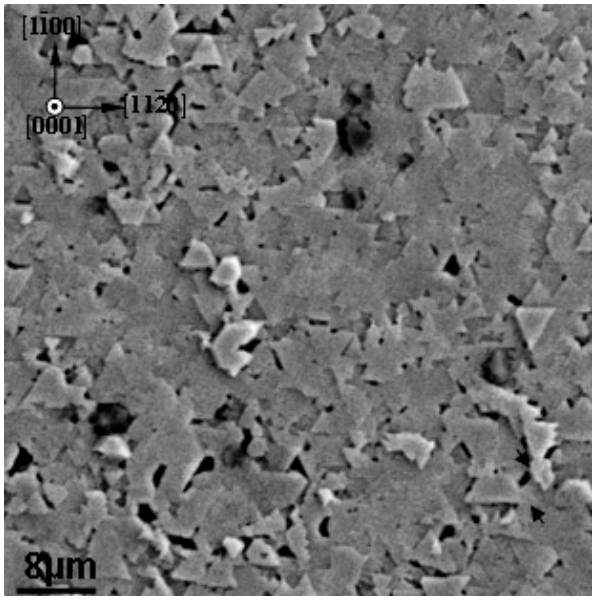

Fig. 9 SEM image showing the surface morphology of the $B_{12}As_2$ film grown on c-plane 6H-SiC.

3.4.2. TEM results and HRTEM simulation

Conventional cross-sectional TEM observation along the [$11\bar{2}0$] zone axis (Fig. 10(a)) reveals a transition layer located between the film and the substrate. Fig. 10(b) and (c) show selective area diffraction (SAD) patterns recorded from a local area in the $B_{12}As_2$ film and the 6H-SiC substrate respectively, confirming the epitaxial relationship determined from SWBXT**.** Compared to the epilayer and the substrate, the SAD pattern recorded from the transition layer shows relative disorder (see Fig. 11(a)). Detailed simulation of Fig. 11(a), shown in Fig. 11(b)-(d), reveals that the transition layer consists of an overlap of twinned $B_{12}As_2$ domains with some strain.

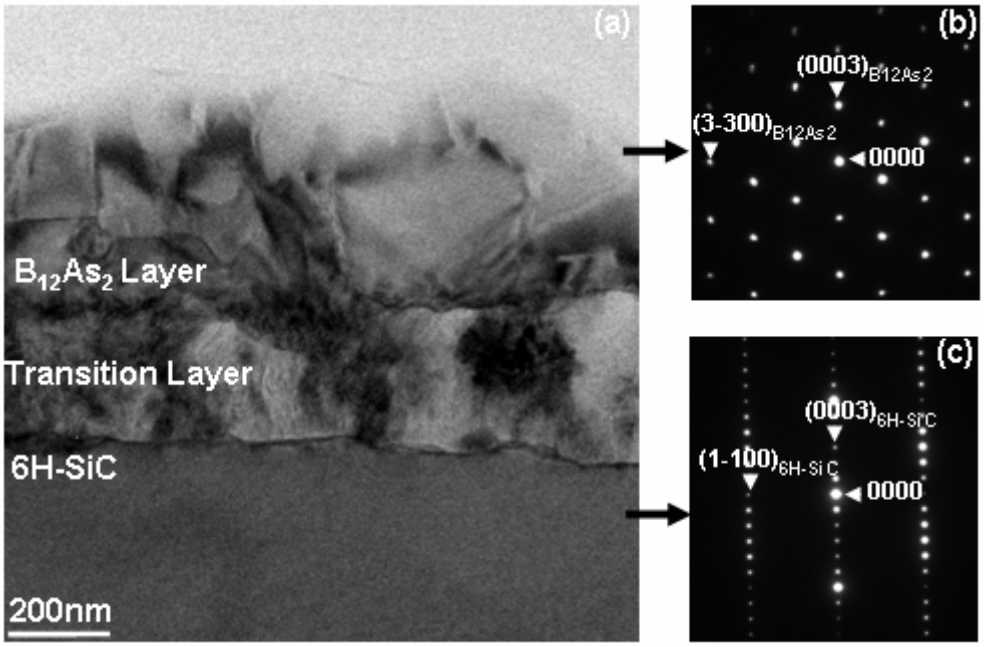

Fig. 10 (a) Cross-sectional TEM image recorded along $[1\bar{1}20]$ revealing a transition layer located between the $B_{12}As_2$ layer and the 6H-SiC substrate. (b) SAD pattern of the $B_{12}As_2$ epilayer recorded along the $[1\bar{1}20]$ zone axis. (c) SAD pattern of the 6H-SiC substrate recorded along the $[1\bar{1}20]$ zone axis.

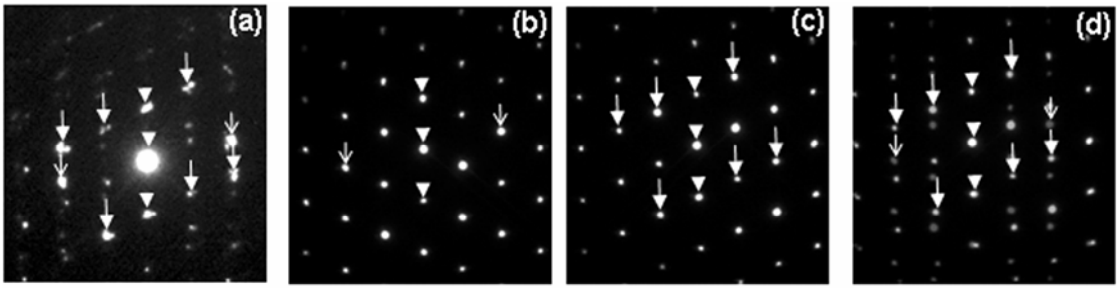

Fig. 11 (a) SAD pattern of the transition layer recorded along the $[1\bar{1}20]$ zone axis; (b) Simulated SAD pattern of one of the $B_{12}As_2$ twin domains; (c) Simulated SAD pattern of the other $B_{12}As_2$ twin domain; (d) Simulated SAD pattern resulted from (b) and (c) showing an overlapped pattern of $B_{12}As_2$ twinned domains. The spots indicated by ⩔ and ▼ represent diffraction spots from matrix and twin domains, respectively. The diffraction spots indicated by ▼ represent diffraction spots common to both matrix and twin.

HRTEM was subsequently employed to provide information on the atomic configurations present in the various domains and the boundaries between them. However, HRTEM images do not always correspond to intuitive projections of the crystal lattice. The contrast and the shape of the features shown in HRTEM images often vary as the defocus condition and sample thickness change. Examples can be seen from Fig. 12(a)-(d), which were recorded from a defect-free region of the $B_{12}As_2$ film viewed along $[1\bar{1}20]$. Obviously, with the change of defocus, the discerned features change as well. As a consequence, it's necessary to bridge the gap between the recorded HRTEM images (which is the intensity

corresponding the electron wave function modified by the objective lens) and the crystal itself. Multislice simulation[24] is an effective method to investigate and accurately assign the atomic origins to the various features observed on HRTEM images (Appendix III). Fig. 13 shows multislice simulation carried out over a range of sample thicknesses and defocus values for $B_{12}As_2$ imaging viewed along $[11\bar{2}0]$. Fig. 14(a) shows a blow-up region from Fig. 12(b). Comparing to both the results of multislice simulation (Fig. 14(b)) and the projections of the crystal structure carried out using CaRine4.0 (Fig. 14(c)). One could find good agreement for sample thicknesses in the range of 8.6 to 12.0 nm (with the best fit at 8.6nm (Fig. 14(b)) and a defocus of 3nm. Detailed comparison between the observed and simulated images and the CaRine projections indicates that the bright spots marked by the dotted circles in both experimental and simulated images as well as in the structural projection arise from neighboring B columns, while those marked by the solid circles arise from columns comprising As atoms and the B atoms which project closest to them. Using a similar approach, HRTEM of the transition layer and the subsequently grown region of epilayer was used to investigate the detailed atomic configurations present in the various domains and at the various interfaces between them. In addition, comparison of the HRTEM images with models of the potential bonding configurations available at the various nucleation sites on the (0001) 6H-SiC surface sheds considerable light on the nucleation and growth mechanisms of the $B_{12}As_2$ film.

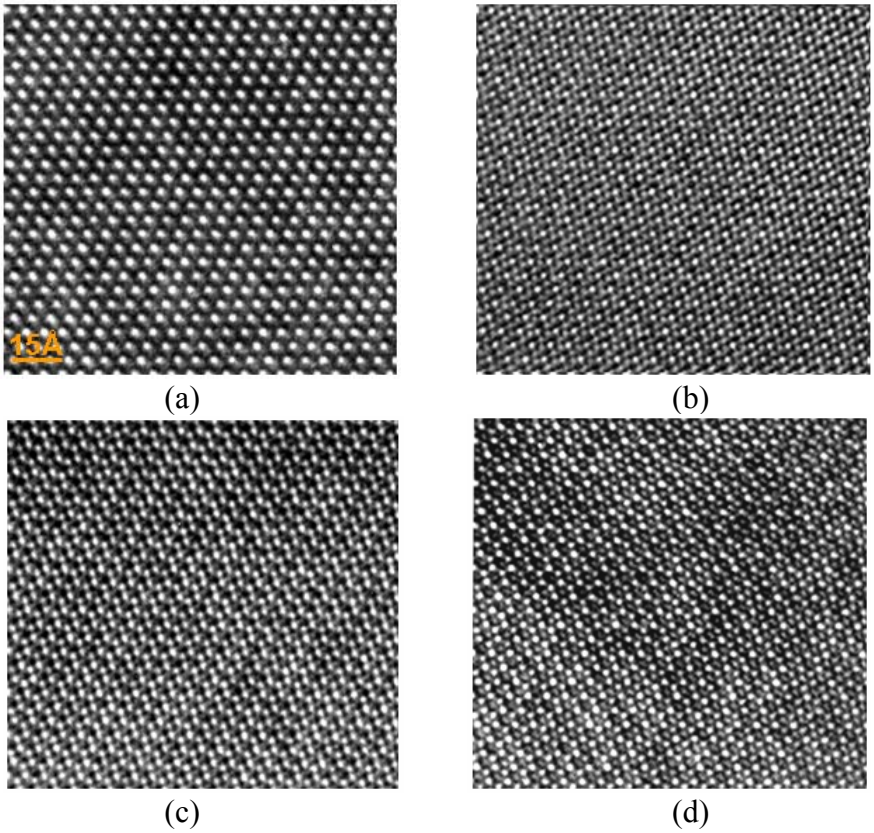

Fig. 12 HRTEM images recorded from a defect-free $B_{12}As_2$ region of under different focuses. (a) f=+114nm; (b) f=+76nm; (c) f=–18nm; (d)f=–48nm.

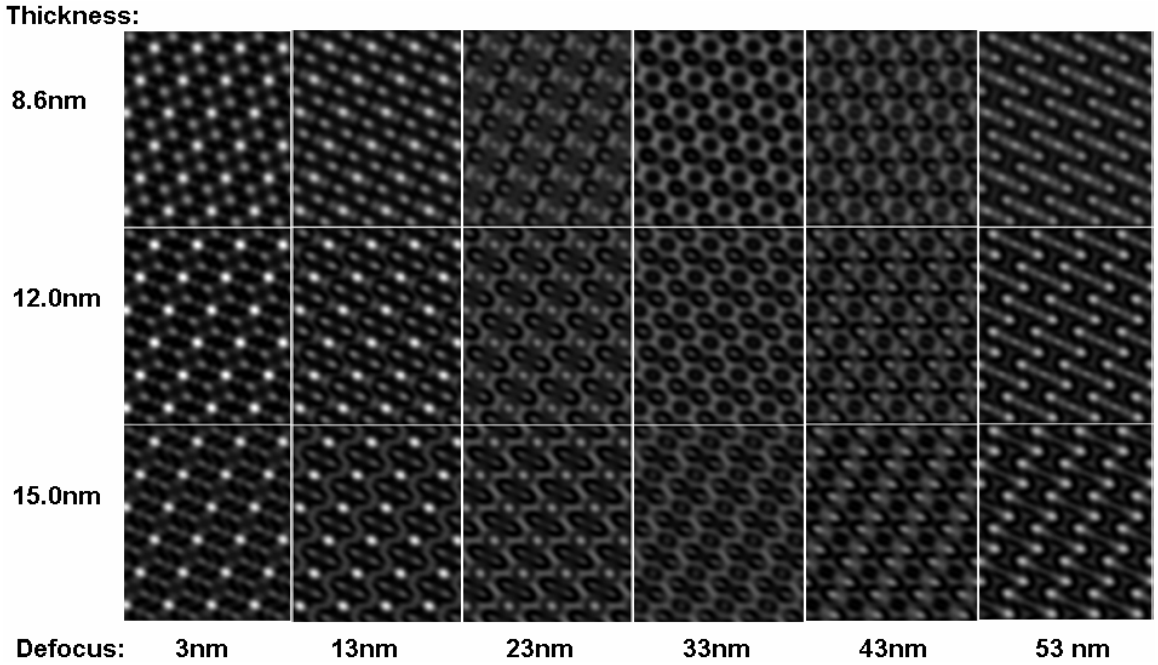

Fig. 13 Multislice simulation over a range of sample thicknesses and defocus values for $B_{12}As_2$ HRTEM imaging viewed along $[11\bar{2}0]$.

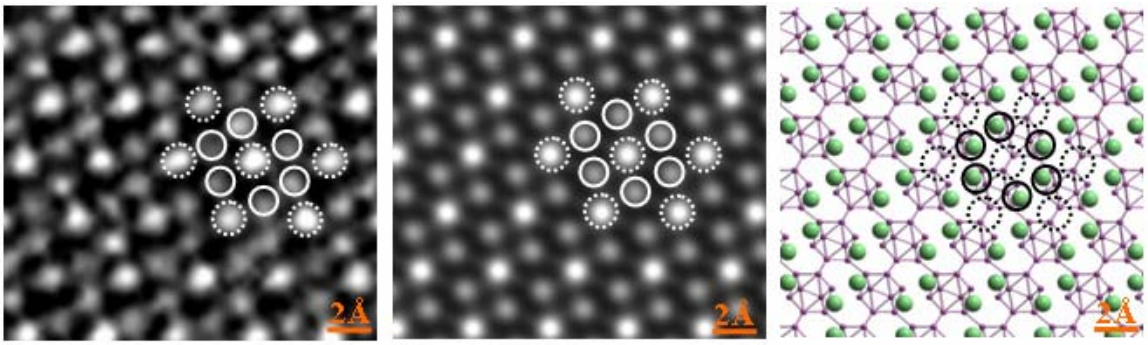

(a) (b) (c)

Fig. 14 (a) Experimental HRTEM image recorded from a defect-free region of the $B_{12}As_2$ film viewed along $[11\bar{2}0]$; (b) Simulated HRTEM image of the $B_{12}As_2$ film corresponding to (a) with defocus=3nm and sample thickness=8.6nm; (c) Atomic configuration of the $B_{12}As_2$ structure with the same projection direction as (a).

3.4.3. Growth mechanism and translational/rotational variants

In the previously reported analysis of possible structural variants in this system (Michael *et al*[Error! Bookmark not defined.]), choice of nucleation sites was based on alignment of the three-fold [0001] axes running through the centers of the icosahedra with the various axes of three-fold symmetry on the SiC (0001) surface. While this approach provides the basic framework for selection of nucleation sites, it's proposed here that the number of possible nucleation sites is reduced compared to this analysis based on consideration of the possible bonding configurations between the epilayer and substrate. If the $B_{12}As_2$ adopts (0001) orientation on the (0001) SiC substrate, it is instructive to consider the dangling bond

configurations presented by the $(000\bar{3})_{B12As2}$ planes (Fig. 15(a))towards the substrate surface (Fig. 15(b)). The triangular configurations of boron atoms that constitute the lower ends of the icosahedra each present a triangular set of boron dangling bonds. These triangular configurations of boron atoms form a hexagonal network which can be accommodated on the substrate surface by the triangular Si dangling bond configurations presented at sites such as those labeled A_1 in Fig. 15(c). Simultaneously, the As dangling bonds (one of which is also shown on Fig. 15(a)) can be accommodated by the Si dangling bonds which are located at the centers of those triangular configurations, made up from A_1 sites, which have their apexes pointing up (see Fig. 15(c)). Since all dangling bonds on both the upper substrate and lower epilayer surfaces are accommodated in this scheme, it appears that this is a highly plausible bonding configuration. For this same orientation of B triangle (i.e. with apex pointing up), there are three other possible sites which allow similar bonding to the Si atoms, shown in Fig. 15(c) as A_2, A_3 and A_4, which are shifted by $1/6<11\bar{2}0>_{B12As2}$ from the "A_1" sites. These constitute translational variants. B triangles in twinned orientation (i.e. with apexes pointing down) can be bonded in a similar way to Si triangles on the four sites marked as A'_5, A'_6, A'_7 and A'_8 in Fig. 15(d), which are shifted by multiples of $1/12<1\bar{1}00>_{B12As2}$ from the "A_1" sites. This makes a total of eight distinct nucleation sites, a number smaller than that proposed by Michael *et al*. This reduction in number of nucleation sites predicted by our modified model can be illustrated by considering, for example, the three so-called chemical variants proposed by Michael *et al* which position the B triangles over Si, C and interstice sites. Of these, according to our bonding analysis, only the interstice site can accommodate the three boron dangling bonds presented at the lower end of the icosahedron as well as the As dangling bonds. At the Si site, the boron atom bonds are oriented towards the C atoms which are buried below the surface and have no dangling bonds. At the C site, the boron atom bonds are oriented towards the interstices between the Si atoms which can provide no bonds. Thus, the Si and C chemical variants can be eliminated. In a similar way, imposing bonding restrictions onto the rotational and translational variants depicted in Michael *et al* also reduces their numbers.

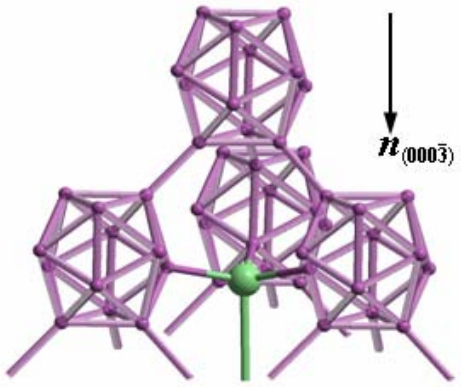

(a)

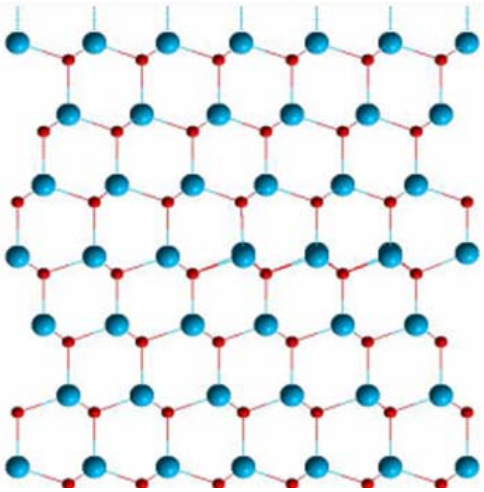

(b)

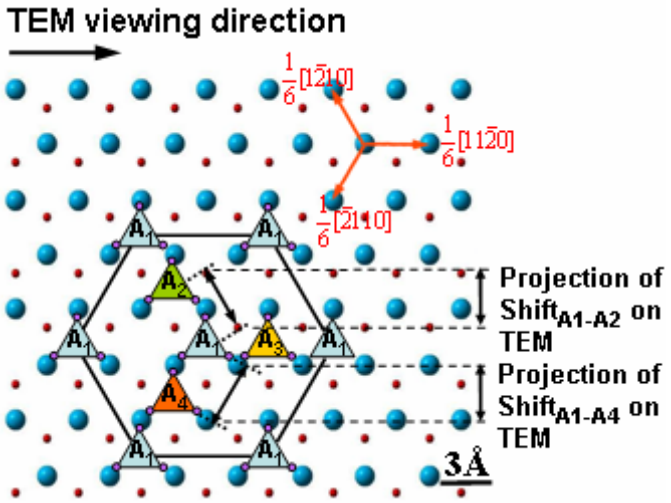
TEM viewing direction
$\frac{1}{6}[1\bar{2}10]$
$\frac{1}{6}[11\bar{2}0]$
$\frac{1}{6}[\bar{2}110]$
Projection of Shift$_{A1-A2}$ on TEM
Projection of Shift$_{A1-A4}$ on TEM
3Å

(c)

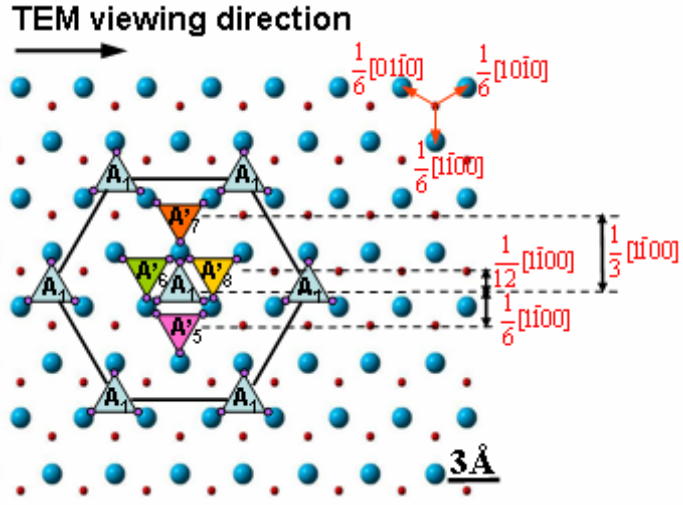
TEM viewing direction
$\frac{1}{6}[01\bar{1}0]$
$\frac{1}{6}[10\bar{1}0]$
$\frac{1}{6}[1\bar{1}00]$
$\frac{1}{12}[1\bar{1}00]$
$\frac{1}{3}[1\bar{1}00]$
$\frac{1}{6}[1\bar{1}00]$
3Å

(d)

Fig. 15 (a) Schematic highlighting the dangling bond configurations presented by the $(000\bar{3})_{B12As2}$ plane. Note the triangular configurations of boron dangling bonds at the lower ends of the icosahedra as well as the arsenic dangling bond; (b) Plan view of four possible translationally variant $B_{12}As_2$ nucleation sites (A_1, A_2, A_3 and A_4) on Si-face (0001) 6H-SiC. Si and C atoms are represented by large and small spheres, respectively. In each case, the sets of three B dangling bonds protruding from the B triangles form bonds to the Si atoms which also form a triangular configuration. Projections of the shifts observed via TEM are labelled; (c) Plan view of the four possible translationally variant nucleation sites (A'_5, A'_6, A'_7 and A'_8) for $B_{12}As_2$ in twinned orientation. The projections of possible shifts on TEM are marked as $1/12[1\bar{1}00]$, $1/6[1\bar{1}00]$ and $1/3[1\bar{1}00]$ respectively.

Since, according to the above detailed analysis, there are eight possible nucleation sites it is perhaps not surprising that there is some degree of disorder in the $B_{12}As_2$ film close to the film/substrate interface as the islands that nucleate at these various sites coalesce and begin to overgrow each other. This is consistent with the conventional TEM observation of the ~200nm thick transition layer close to the interface (Fig. 10)

3.4.4. Evidence of translational and rotational variants

Direct evidence for the co-existence of the $1/6<11\bar{2}0>_{B12As2}$ translational variants of Fig. 15(c) can be found in the HRTEM images recorded from the transition layer region such as Fig. 16(a). The complex structure observed on this image suggests that it may be due to the overlap between more than one variant. This is confirmed by considering the overlap between two translational variants mutually shifted by a $1/6[1\bar{2}10]_{B12As2}$ translation as shown in the CaRine projection model in Fig. 16(b). Further confirmation is provided by the Moiré pattern formed by the overlap, along the $[11\bar{2}0]_{B12As2}$ electron imaging direction, between HRTEM images (recorded from a perfect $B_{12}As_2$ region) mutually shifted by a $1/6[\bar{1}2\bar{1}0]_{B12As2}$ translation, as shown in Fig. 16(c). Regions comprising overlapped translational variants were restricted to the transition layer with somewhat larger size domains of rotational variants dominating the film at thicknesses beyond ~200nm. In order to understand why and how the translational variants apparently grow out following around 200nm of growth, it is instructive to consider the possible bonding configurations that might arise during the lateral coalescence of two translational variants.

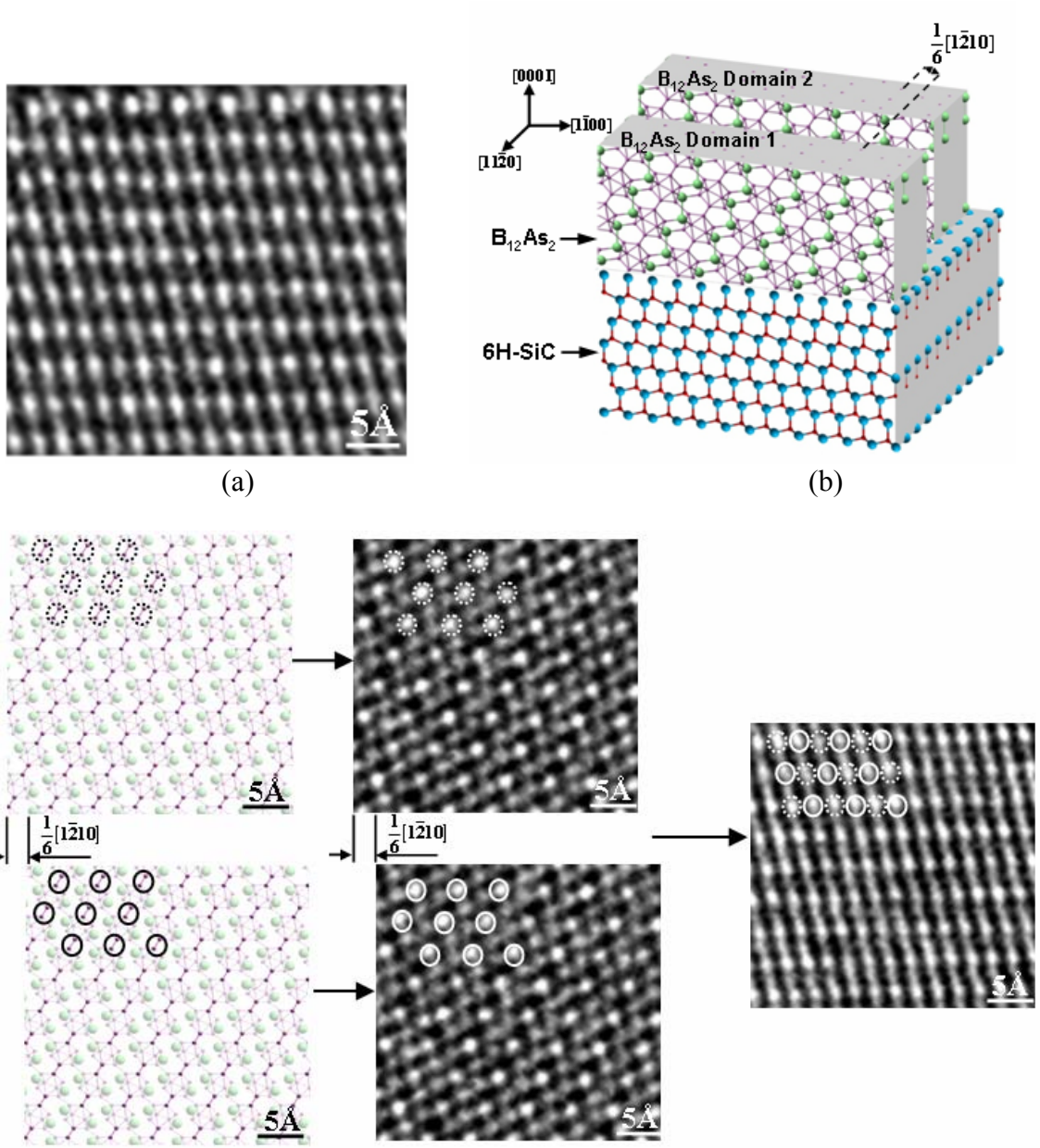

Fig. 16 (a) HRTEM observation of the transition layer viewed along the $[1\bar{2}0]_{B12As2}$ zone axis; (b) Crystal visualization of translation variants with $1/6[1\bar{2}10]$ mutual shift arising from nonequivalent nucleation sites on the substrate; (c) Moiré pattern formed by overlapping two $B_{12}As_2$ HRTEM images taken along $[1\bar{2}0]$ direction mutually shifted by $1/6[1\bar{2}10]$compared with CaRine projections. According to the HRTEM simulation in Fig. 14, the solid circles in Fig. 16(c) correspond to the projection of neighboring B columns from $B_{12}As_2$ Domain1 while the dotted circles correspond to those from Domain2.

In order to visualize this, it is useful to consider $B_{12}As_2$ as an (0001) layered structure comprising the hexagonal networks of boron triangles which were depicted in Fig. 17(b). If the first layer is accommodated at A_1 sites, successive layers are accommodated at sites

comprising stacking positions B_1 and C_1, as shown schematically in perspective in Fig. 17(a) and in projection on the left hand side of Fig. 17(b). This *ABC* stacking sequence is somewhat analogous to that encountered in face centered cubic type structures although here the structure is not close packed since, within a given layer (say A_1), the icosahedra are connected via bonds to arsenic atoms located at positions which project along [0001] to a second position (say C_1) in the stacking sequence. These arsenic atoms then connect along [0001] to other arsenic atoms in the same stacking position which connect triangular configurations of icosahedra in the third position (say B_1) in the stacking sequence. Thus, A_1 and B_1, B_1 and C_1, and C_1 and A_1 layers are connected via arsenic atom pairs that are located respectively in the C_1, A_1 and B_1 stacking positions. For comparison purposes, the right hand side of Fig. 17(b) shows the stacking sequence for one of the translational variants ($A_2B_2C_2$). As these initially nucleated layers attempt to coalesce during growth, considerable bonding problems arise from the steric hindrance between boron icosahedra in the adjacent A_1 and A_2 stacking positions (see, for example, the interface schematically represented as a dashed line in Fig. 17(b)). Similar problems occur in at the lateral interfaces between the subsequently stacked B_1 and B_2 and C_1 and C_2 layers. Such problems can be ameliorated by shifting the structure of one of the variants by 1/3[0001], such that, for example, A_1 becomes adjacent to B_2 at the lateral interface (see Fig. 17(c)) or equivalently C_2 (Fig. 17(d)). Similar shifts are experienced in all subsequent layers, enabling the boron icosahedra (and the As atoms) to bond to each other in a much more stable configuration, albeit distorted. This 1/3[0001] shift can be produced by the creation of a Frank partial dislocation with b=1/3[0001] which can be produced by the collapse of layers in one of the variants as they overgrow each other as shown in Fig. 18(a). This provides the mechanism by which the translational variants can be effectively eliminated during growth. An example of such a Frank partial dislocation (FPD) can be seen in the HRTEM image recorded from the transition region shown as Fig. 18(b). Fig. 18(c) shows the postulated translational domain configuration. When these domains meet each other, FPDs are expected be present so as to provide reasonable bonding configurations across the junctions where the domains join.

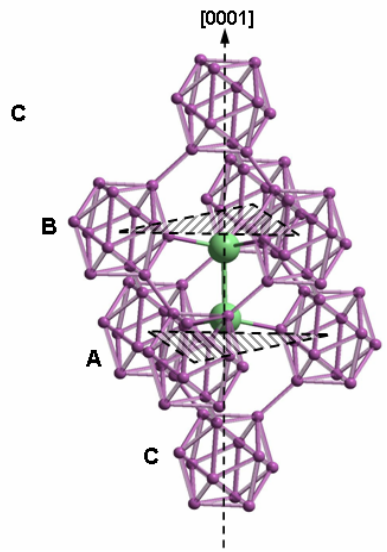

(a)

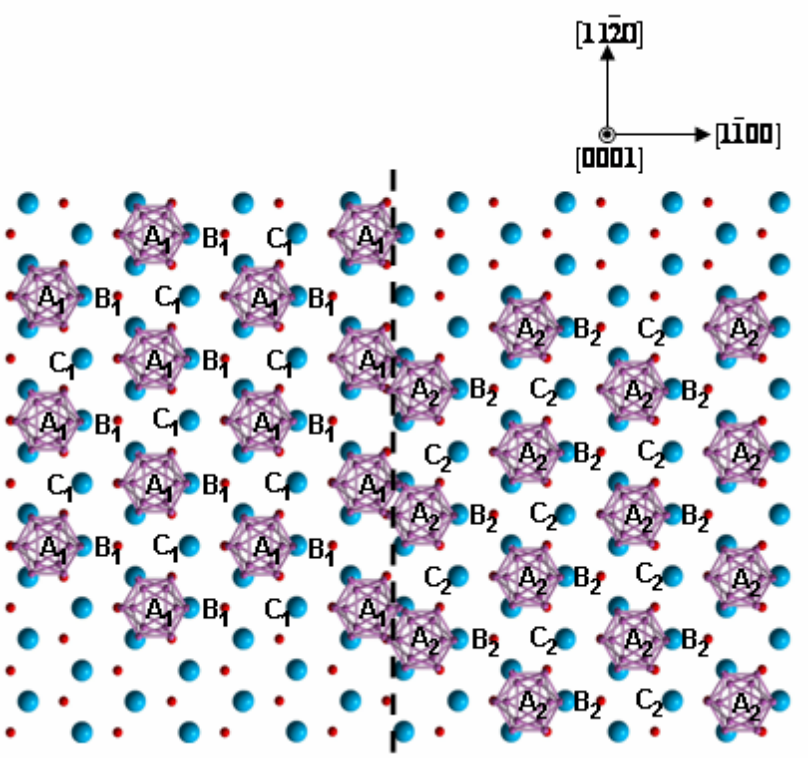
[11$\bar{2}$0]
[1$\bar{1}$00]
[0001]
A1
B1
C1
A2
B2
C2

(b)

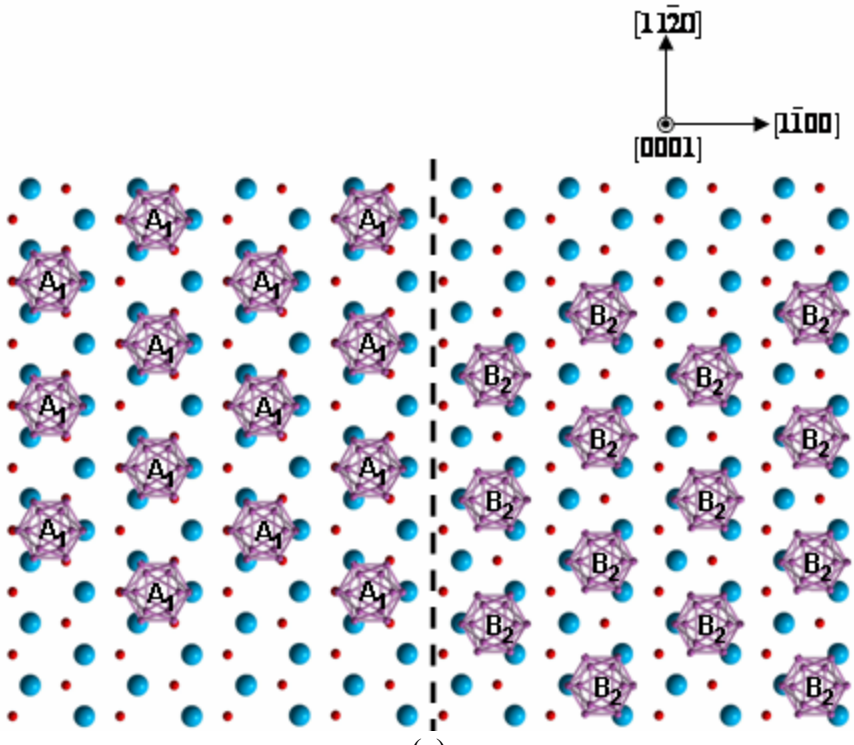
[11$\bar{2}$0]
[1$\bar{1}$00]
[0001]
A1
B2

(c)

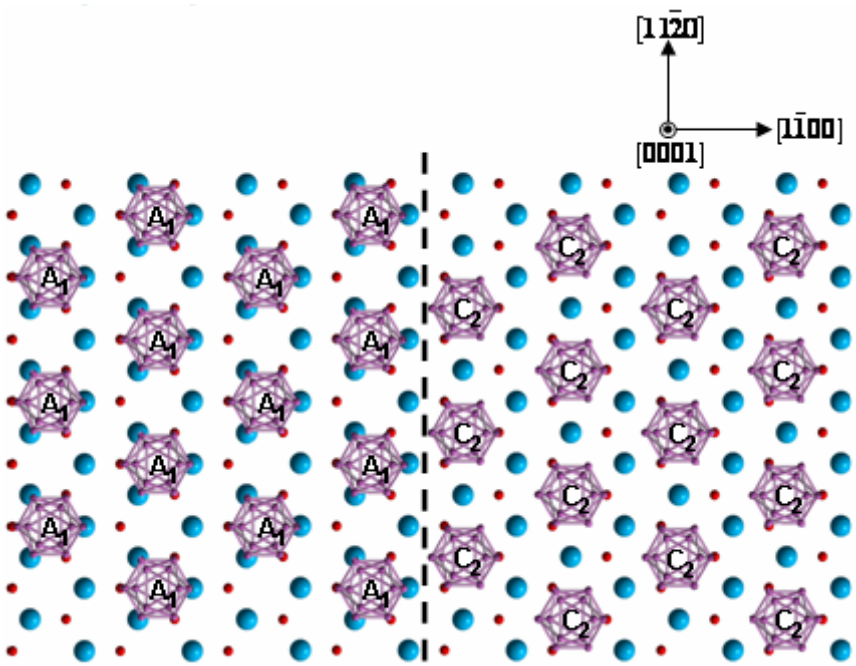

(d)

Fig. 17 (a) Representation of the structure of $B_{12}As_2$ showing that it can be considered as an (0001) layered structure with the boron icosahedra forming equilateral triangular nets as represented by the stacking positions "*A*" (at the apexes of the shaded triangle in layer "*A*". Successive layers adopt similar configurations with the boron icosahedra occupying the stacking positions *B* and *C*; (b) Projection of the stacking positions of the boron triangles on the $(0001)_{SiC}$ substrate surface. Left hand side shows the boron triangles located at sites of type A_1 (see Fig. (6)) and the right hand side shows boron triangles located at sites of type A_2. The stacking positions of the subsequently stacked layers B_1 and C_1 and B_2 and C_2 are also shown. The dotted line dividing the two regions schematically represents a lateral boundary between the translational domains which are mutually shifted by $1/6[1\bar{2}10]$; (c) same region following a 1/3[0001] shift of the right hand $B_{12}As_2$ domain aligning A_1 with B_2 and enabling stable bonding between the two $B_{12}As_2$ domains. (d) Same regions following an equivalent 1/3[0001] shift of the right $B_{12}As_2$ domain aligning A_1 with C_2 and again enabling equivalently stable bonding between the two $B_{12}As_2$ domains.

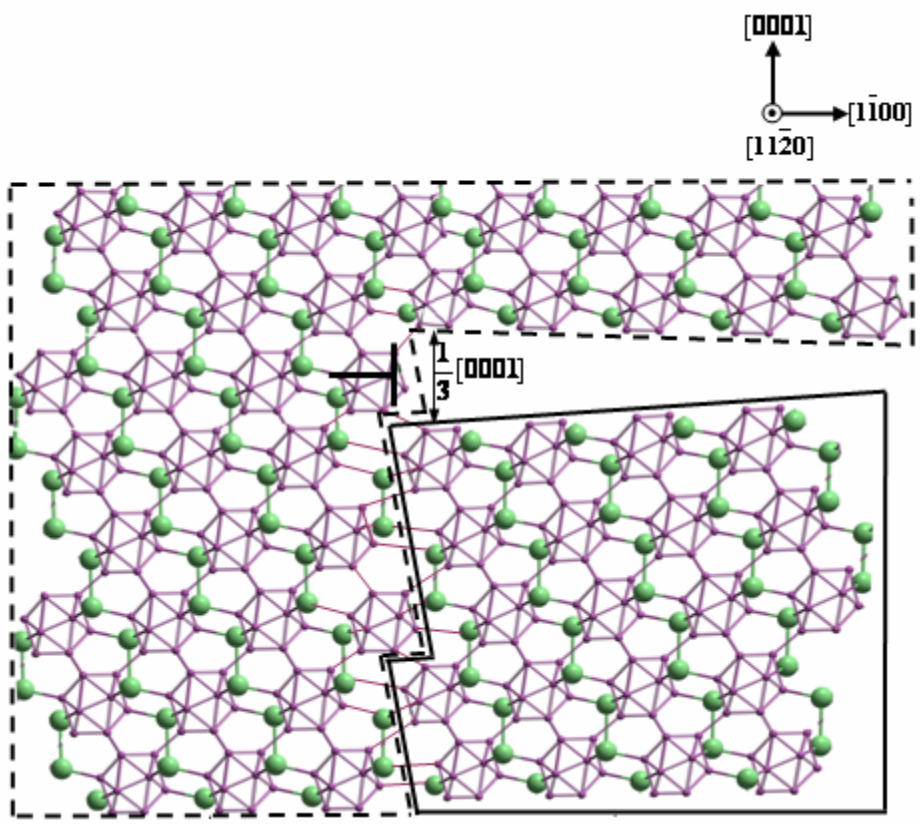
[0001]
[1$\bar{1}$00]
[11$\bar{2}$0]
$\frac{1}{3}$[0001]

(a)

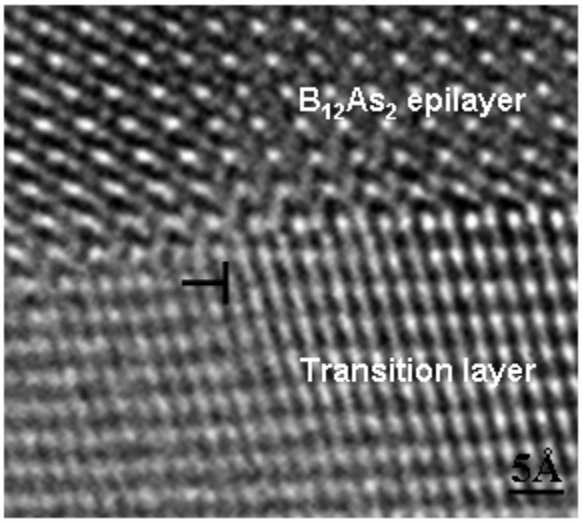
$B_{12}As_2$ epilayer
Transition layer
5Å

(b)

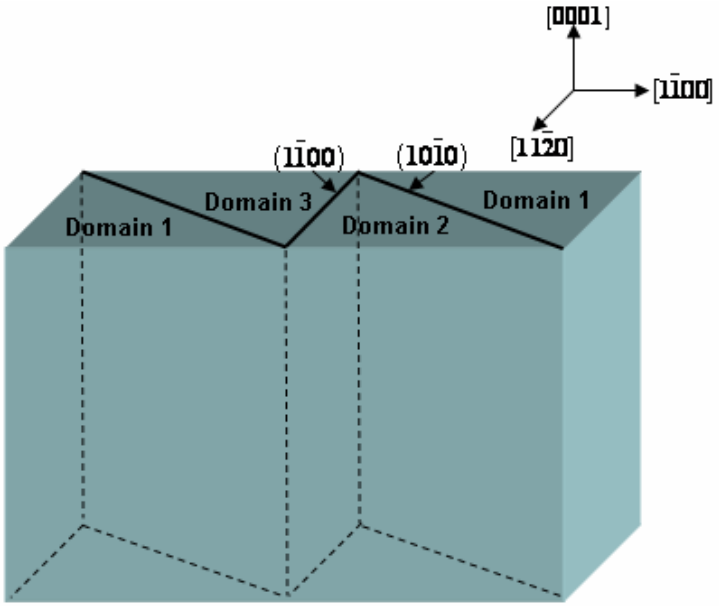

(c)

Fig. 18 (a) Crystal visualization, viewed along the [$11\bar{2}0$] electron imaging direction, showing how a Frank partial dislocation can produce the 1/3[0001] shift. (b) HRTEM image recorded along [$11\bar{2}0$] zone axis showing a Frank partial dislocation in the interface between the transition layer and the $B_{12}As_2$ epilayer at the junction between two translational variants; (c) Schematic of $B_{12}As_2$ translational domain configuration, showing the possible domain configuration corresponding to Fig. 18(b).

While the creation of $1/3[0001]_{B12As2}$ Frank partial dislocations enables the elimination of the translational variants no such solution can be found for the bonding problems created by lateral coalescence of twin variants. These latter boundaries tend to be diffuse and wavy and persist until one twin variant is able to overgrow the other enabling the creation of the much more stable (0003) twin boundaries (TBs). Such an example is shown in Fig. 19. The curvy twin boundary TBI is present in the vertical junction where the $B_{12}As_2$ matrix and twin join together. This type of TBs has high energy and unstable, it can not exist stably with a vertical linear plane, which then gives rise to its zigzag-like feature. In contrast, TBII, (0003) twin boundary, has much lower energy and thus is more stable. The existence of such rotational variants in these films can actually be predicted from the theory of degenerate epitaxy, which treats the growth of a lower symmetry epitaxial film on a higher symmetry substrate[25, 26]. This theory, which is based on two dimensional point group analysis of the substrate and epilayer surfaces, predicts the existence of two rotational variants (Table 1) for the growth of *3m* symmetry (0001) $B_{12}As_2$ (Fig. 20(a)) on *6mm* symmetry (0001) 6H-SiC (Fig. 20(b)). These rotational variants are related by a symmetry operation which exists in the substrate but not in the film ($\{11\bar{2}0\}$ mirror planes exist in both $B_{12}As_2$ and 6H-SiC while $\{1\bar{1}00\}$ mirror planes exist only in 6H-SiC).

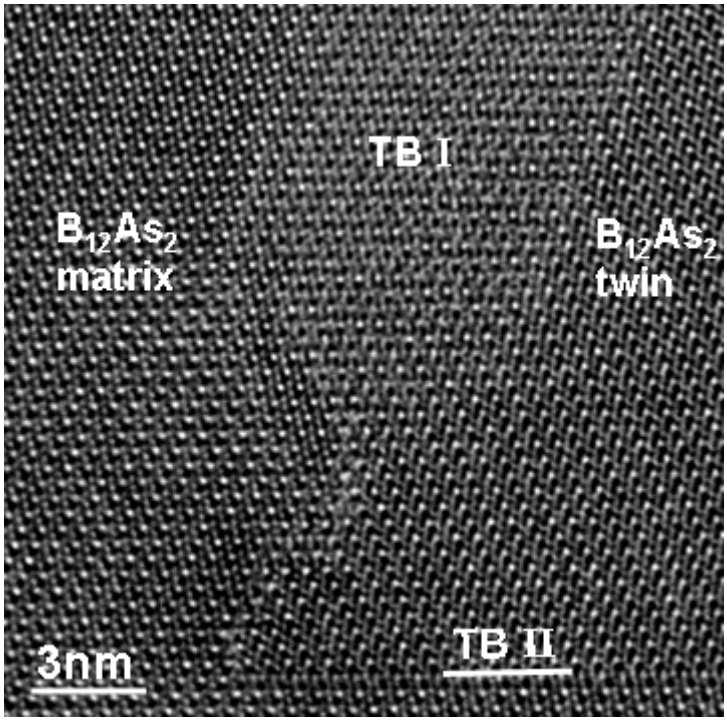

Fig. 19 HRTEM image showing zigzag like twin boundary existing in the vertical interface where the $B_{12}As_2$ matrix and twin join together.

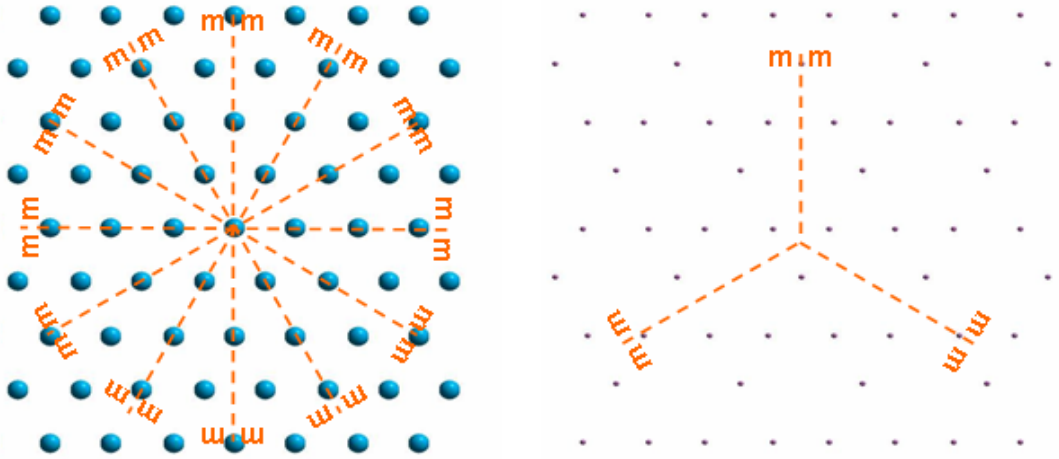

(a) (b)

Fig. 20 (a) The projection of Si-face 6H-SiC (0001) surface showing *6mm* symmetry; (b) The projection of $B_{12}As_2$ (111) surface showing *3m* symmetry.

Table 1 The number of variants formed in epitaxial growth, listed by symmetry of the substrate, S, and epilayer, E, and with the global symmetry given in parentheses.[Error! Bookmark not defined.]

E	S	1	m	2	2mm	3	3m	4	4mm	6	6mm
1		1	2	2	4	3	6	4	8	6	12
m		1	1	2	2	3	3	4	4	6	6
2		1	2	1	2	3	6	2	4	3	6
2mm		1	1	1	1	3	3	2	2	3	3
3		1	2	2	4	1	2	4	8	2	4
3m		1	1	2	2	1	1	4	4	2	2
4		1	2	1	2	3	6	1	2	3	6
4mm		1	1	1	1	3	3	1	1	3	3
6		1	2	1	2	1	2	2	4	1	2
mm		1	1	1	1	1	1	2	2	1	1

While rotational variants are readily observable on HRTEM images, detailed observation of the atomic configurations across (0003) twin boundaries (TBs) can provide verification of the twin nucleation sites on the SiC surface. Fig. 21(a) shows a HRTEM image recorded from a region of the $B_{12}As_2$ film close to the interface containing an (0003) twin boundary with the simulated images shown as insets. Fig. 21(b) is the magnified image of the enframed dotted region in Fig. 21(a). If this boundary originated from the overgrowth of a twinned island across an untwinned island, the shifts between the twin and matrix nucleation sites should be manifested in the (0003) twin boundary. The projected shifts in the twin plane along the TEM viewing direction would be either $1/12[\,1\bar{1}00\,]_{B12As2}$, $1/6[\,1\bar{1}00\,]_{B12As2}$ or $1/3[\,1\bar{1}00\,]_{B12As2}$ as shown in Fig. 15(d). The twin boundary shown in Fig. 21(a) exhibits a shift of around 1.78Å, corresponding to $1/6[\,1\bar{1}00\,]_{B12As2}$, thus confirming the formation mechanism. Such shifts were commonly observed in twin boundaries throughout the film. This type of twin boundary can be referred to as a "faulted twin boundary". The detailed atomic and bonding configurations across such twin boundaries are discussed in the following.

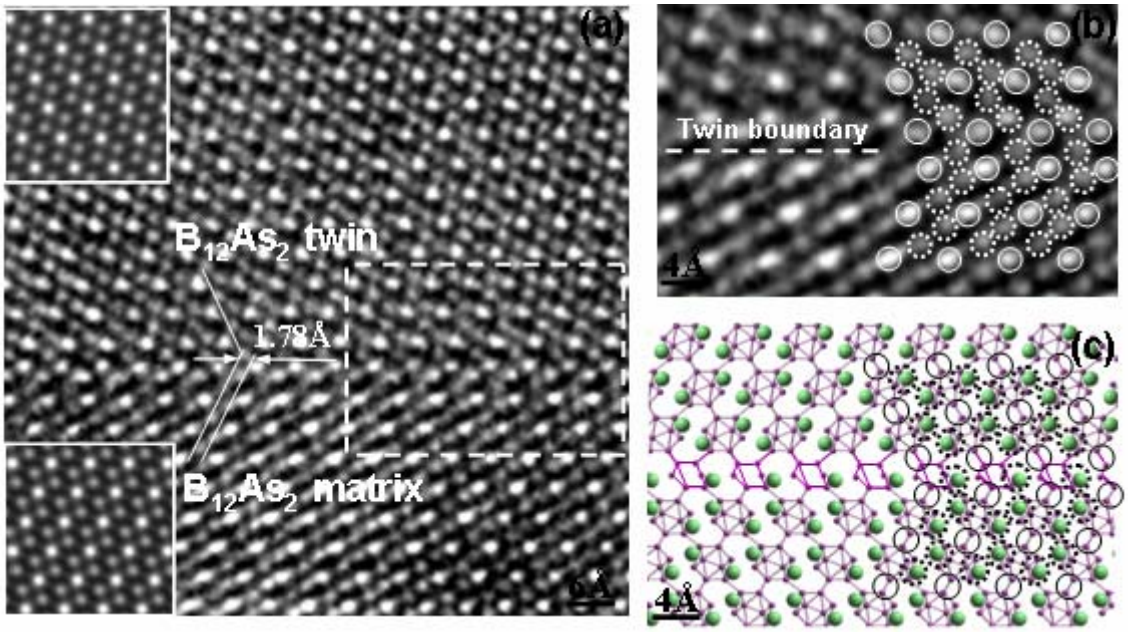

Fig. 21 (a) High resolution TEM image, taken along $[1\bar{2}0]_{6H\text{-}SiC}$ zone axis, recorded from a defective region in the $B_{12}As_2$ film containing a (0003) twin boundary with $1/6[\bar{1}100]_{B12As2}$ projected shift. The left two inserts in (a) are the simulated $B_{12}As_2$ HRTEM images for matrix and its twin with defocus=3nm and sample thickness=8.6nm; (b) Enlarged HRTEM image of the enframed dotted region in (a); (c) Corresponding crystal visualization to (b) showing the postulated atomic configuration across the (0003) $B_{12}As_2$ twin boundary. The solid circles stand for the projection of neighboring B columns, the dotted ones for the projection of columns comprising As and their nearest B neighbors.

In addition to providing information on the nucleation sites, HRTEM of the twin boundaries in comparison with CaRine structural projections enables the possible bonding configurations across the observed (0003) twin boundaries to be assessed. For the faulted twin boundary exhibiting the $1/6[\bar{1}100]_{B12As2}$ shift, the structure proposed in Fig. 21 (c) maintains reasonable bonding and agrees well with the HRTEM observations. In this structure, boron forms 9 atom clusters in the shape of a triaugmented triangular prism (one of the Johnson figures[27], similar to the icosahedron). For those twinned domains nucleated on sites shifted by $1/12[\bar{1}100]_{B12As2}$ with respect to the matrix, as viewed along $[1\bar{2}0]$, the magnitude of this shift (~0.9Å) is beyond the HRTEM resolution (~1.3Å) and would be difficult to discern on the HRTEM images. Twin boundaries exhibiting little or no shift were relatively uncommon in the film although an example of such a twin boundary is shown in Fig. 22(a)-(b) along with the suggested atomic configuration (Fig. 22(c)). To maintain reasonable bonding, arsenic atoms in the $B_{12}As_2$ matrix are directly bonded to arsenic atoms from the twin. Boron icosahedra from the matrix and the twin are bonded to each other across the twin boundary.

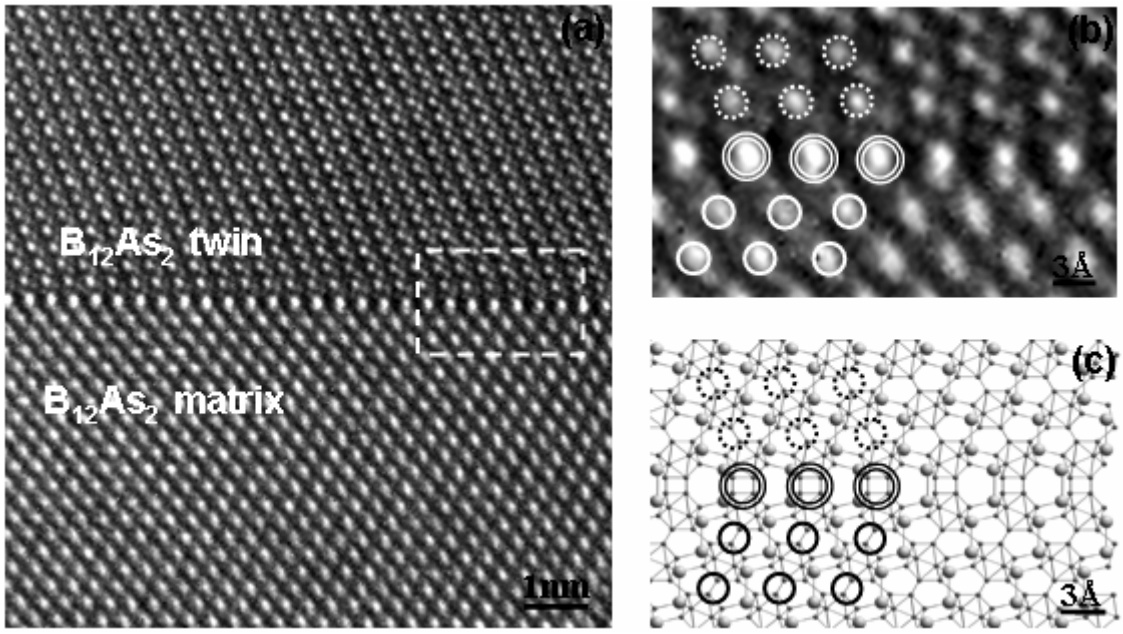

Fig. 22 (a) High resolution TEM image, taken along $[1\bar{2}\bar{1}0]_{6H\text{-}SiC}$ zone axis, recorded from another defective region in the $B_{12}As_2$ film containing an (0003) twin boundary with $1/12[\bar{1}100]_{B12As2}$ projected shift; (b) Enlarged HRTEM image of the enframed dotted region in (a); (c) Crystal visualization corresponding to (b) showing the postulated atomic configuration across the (0003) $B_{12}As_2$ twin boundary. The dotted circles correspond to the projection of the neighboring B columns in the $B_{12}As_2$ twin, the single solid circles to the projection of neighboring B columns in the $B_{12}As_2$ matrix and the double solid circles to the columns comprising bonded B atoms that make up the $B_{12}As_2$ twin boundary.

3.5. Conclusions

The microstructure in $B_{12}As_2$ epitaxial layers grown by CVD on (0001) 6H-SiC substrates has been analyzed in detail. SWBXT enabled macroscopic characterization of the substrate/epilayer ensembles and revealed the presence of a quite homogenous solid solution of twin and matrix epilayer domains forming a submicron mosaic structure. The growth orientation of the epilayer with respect to the substrate was determined to be $(0001)_{B12As2}<1\bar{2}\bar{1}0>_{B12As2}||(0001)_{6H\text{-}SiC}<1\bar{2}\bar{1}0>_{6H\text{-}SiC}$. $B_{12}As_2$ twinned domains were found in the epilayer and the twin relationship consisted of a 180° (or equivalently 60°) rotation about $[0001]_{B12As2}$ in agreement with previous reports. HRTEM observation revealed an evolution of the film microstructure from an ~200nm thick disordered mosaic transition layer to a more ordered structure. The transition layer was suggested to arise from the coalescence of translationally and rotationally variant domains nucleated at the various nucleation sites on the (0001) 6H-SiC surface. Eight possible types of nucleation sites were found to be available on the substrate surface based on analysis of the stable bonding configurations between the boron triangles at the bottom of the boron icosahedra, and the Si dangling bonds on the Si oriented (0001) 6H-SiC substrate surface. In the transition layer, competition between the growth of the various domains is mediated in part by the energy of the boundaries created between them as they coalesce. Boundaries between translationally variant domains are shown to have unfavorable high-energy bonding configurations while

the formation of a $1/3[0001]_{B12As2}$ Frank partial dislocation enabled elimination of these high energy boundaries during mutual overgrowth. Consequently the film quality beyond thicknesses of ~200nm can be improved as the translational variants grow out leaving only the twin variants. (0003) twin boundaries in the regions beyond 200nm are shown to possess fault vectors such as $1/6[1\bar{1}00]_{B12As2}$ which are shown to originate from the mutual shift between the nucleation sites of the respective domains.

4. $B_{12}As_2$ grown on 3.5° off-axis c-plane (0001)6H-SiC

4.1. Outline

The microstructure in a $B_{12}As_2$ epitaxial layer grown by CVD on a 3.5° off-cut (0001) 6H-SiC substrate is examined by using SWBXT, SEM, conventional and high resolution TEM. It is revealed that the epilayer contains a solid solution of twin and matrix $B_{12}As_2$ domains forming a mosaic structure. The basic epitaxial relationship is similar to the one grown on on-axis c-plane 6H-SiC, which is $(0001)_{B12As2}<11\bar{2}0>_{B12As2}||(0001)_{6H\text{-}SiC}<11\bar{2}0>_{6H\text{-}SiC}$.

4.2. Introduction

Growth of a lower symmetry epilayer on a higher symmetry substrate often produces a mixture of structural variants (rotational and translational) in the film, a phenomenon which has been referred to as degenerate epitaxy[Error! Bookmark not defined., Error! Bookmark not defined.]. A numeration of these variants can be obtained by analysis of the 2D point groups of the substrate surface and the epilayer surface which grows on the particular substrate orientation. For the growth on c-plane 6H-SiC, as analyzed in Chapter 3, only polycrystalline films with a high density of defects and numerous $B_{12}As_2$ twin boundaries are possible, as the films adopt multiple orientations (involving both translational and rotational) relative to the single terrace substrate with equal possibilities. Consequently, breaking up the symmetry of substrate surface to diminish the generation of structural variants is an important strategy to grow single crystalline $B_{12}As_2$. Such a symmetry reduction on the substrate surface could be achieved by the presence of an off-cut angle, which offers multiple atomic terraces instead of one single terrace on the substrate surface. In addition, the application of offcut can significantly narrow the area of each terrace and thus may limit the number of possible structural variants. Thus the use of offcut substrates potentially enables manipulation of the relative populations of the multiple variants. Such a study on offcut (0001) 6H-SiC substrates has so far been unsuccessful[Error! Bookmark not defined., Error! Bookmark not defined.], but the growth mechanism on the offcut substrates remains unknown. In this chapter, an offcut c-plane 6H-SiC has been used to study the effect of offcut substrate surface on the defect structure in the epifilm.

4.3. Experimental

3.5° off-cut c-plane (0001) 6H-SiC substrates were used for the CVD growth of $B_{12}As_2$. The $B_{12}As_2$ films were synthesized with gaseous precursors of 1% B_2H_6 in H_2 and 2% AsH_3 in H_2. The films were deposited at 1300°C and 500 Torr of reactor pressure for 30 minutes. The epitaxial films of $B_{12}As_2$ had a nominal thickness of 0.5 μm. The cross-sectional TEM samples were made parallel to $(11\bar{2}0)$. The indices referenced to the four index hexagonal system are also utilized for microstructure analysis. The sample was mechanically thinned and polished, using the standard T-tool employing 30 μm, 15 μm, 6 μm, 3 μm, 1 μm and 0.5 μm diamond lapping films, until the sample thickness reached ~60μm. Then it was further thinned to less than 5μm thick by using traditional dimpling method. Finally it was ion milled to electron transparency. High resolution TEM was carried

out using a JEOL 2100F system with an electron voltage of 200keV. SWBXT was performed on as-grown films at the Stony Brook synchrotron topography facility at the National Synchrotron Light Source. The transmission Laue patterns were recorded on Kodak SR5 x-ray films at a sample to film distance of 15cm. Structural projections were produced using the commercial software package CaRine 4.0.

4.4. Results and discussion

4.4.1. SWBXT and SEM results

Fig. 23(a)-(d) show the SEM observation from two local areas on the surface of the film. It reveals a composite structure consisting of two types of equilateral triangular feature, each with dimensions of several μm, which are mutually rotated by 180° about the [111] surface normal. These triangular grains indicate the presence of twin related $B_{12}As_2$ domains. The morphology of the triangular features was determined using orientation information provided by SWBXT and found to contain a flat (0001) $_{B12As2}$ facet bounded by three equivalent $(1\bar{1}00)_{B12As2}$ facets. This observation is similar to the one from the growth on on-axis c-plane 6H-SiC. Fig. 24 shows a transmission incidence SWBXT Laue pattern from the sample recorded with the epilayer as the X-ray exit surface. Detailed indexing analysis shows the epitaxial film/substrate relationship of $(0001)_{B12As2}<11\bar{2}0>_{B12As2}||(0001)_{6H\text{-}SiC}<11\bar{2}0>_{6H\text{-}SiC}$ and the $B_{12}As_2$ is present in two distinct orientations related by a 180° twin rotation about the (0001) $_{B12As2}$ plane normal. The strong, well-defined diffraction spots come from the 6H-SiC substrate ad are labeled with hexagonal *hkil* indices without subscripts while the more diffuse spots come from $B_{12}As_2$ and are labeled with hexagonal *hkil* indices with subscripts of roman numerals *I* or *II* indicating matrix or twin orientation (in some cases the matrix and twin reflections coincide). Obviously the area of the $B_{12}As_2$ diffraction spots appears different from that of the SiC spots, which is suggested due to the presence of mosaicity and high density of defects in the film. This leads to an overall divergence in the diffracted beams emanating from both the matrix and twin regions. The intensities of diffraction spots from the $B_{12}As_2$ matrix and twin are comparable, thus the overall appearance of the $B_{12}As_2$ matrix and twin diffraction spots is consistent with a mosaic and quite homogenous solid solution of twin and matrix domains which are of a size that is below the spatial resolution of X-ray topography (a few microns). In order to acquire further microstructural information for the study of growth mechanism on such an off-cut substrate, TEM imaging, in particular, HRTEM, have been carried out on (11-20) cross-sectional samples.

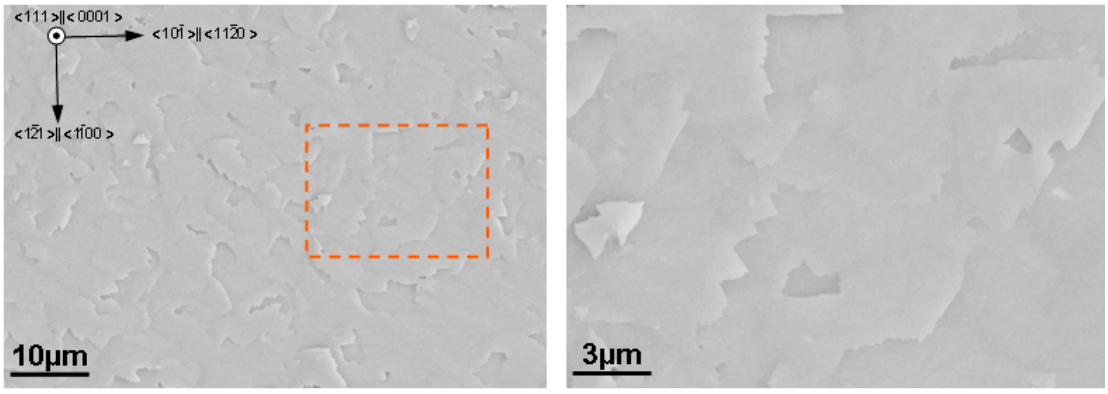

(a) (b)

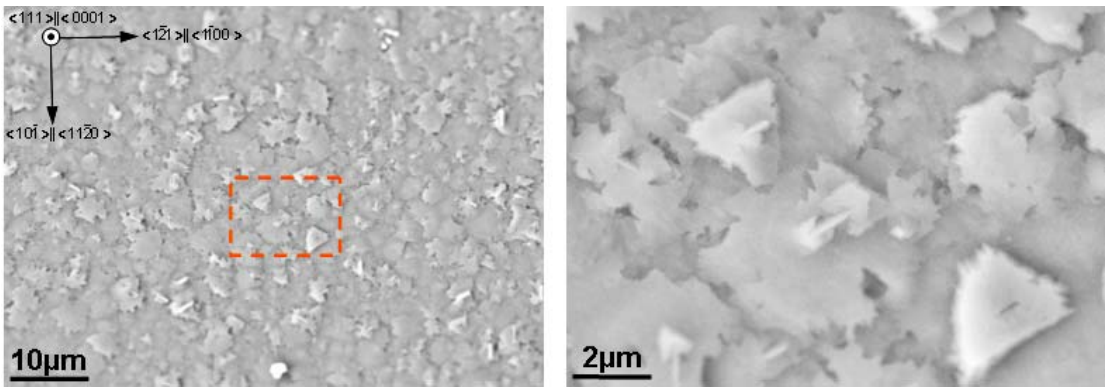

(c) (d)

Fig. 23 SEM images showing the surface morphologies of two local areas, each of which shows the presence of two types of triangular defects.

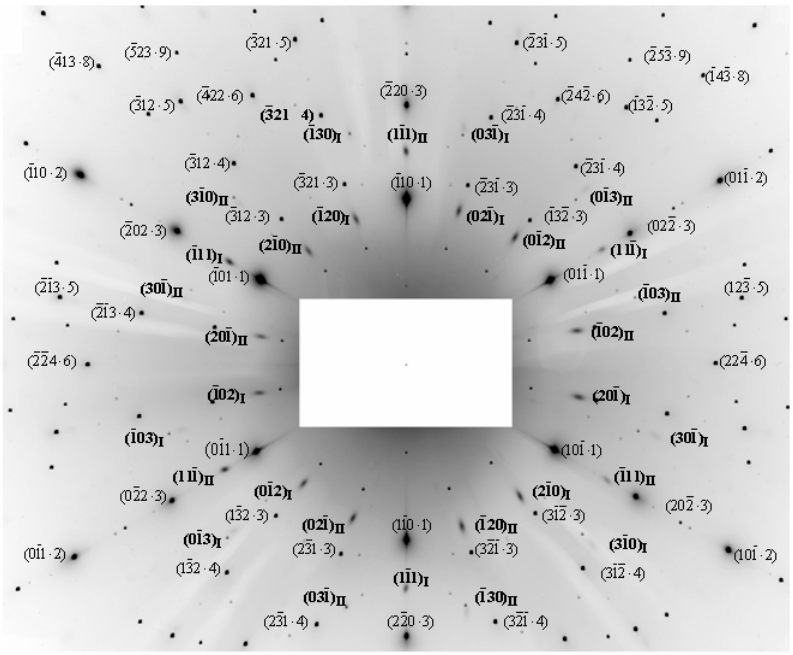

Fig. 24 Transmission SWBXT Laue pattern of the sample with $B_{12}As_2$ epilayer grown on offcut c-plane 6H-SiC.

4.4.2. TEM results

Fig. 25(a)-(c) shows conventional cross-sectional TEM observation on a TEM foil made from the offcut sample with a epilayer grown on 3.5° offcut c-plane 6H-SiC, viewed along the [$11\bar{2}0$] zone axis. Detailed measurements from the SAD patterns recorded from a local area in the $B_{12}As_2$ film (Fig. 25(b)) and the 6H-SiC substrate (Fig. 25(c)) confirm the epitaxial relationship determined from SWBXT observation, which is $(0001)_{B12As2}<11\bar{2}0>_{B12As2}||(0001)_{6H\text{-}SiC}<11\bar{2}0>_{6H\text{-}SiC}$. Furthermore, simulation of SAD patterns

in Fig. 26(a)-(d) reveals that the $B_{12}As_2$ layer is composed of an overlap of twinned $B_{12}As_2$ domains.

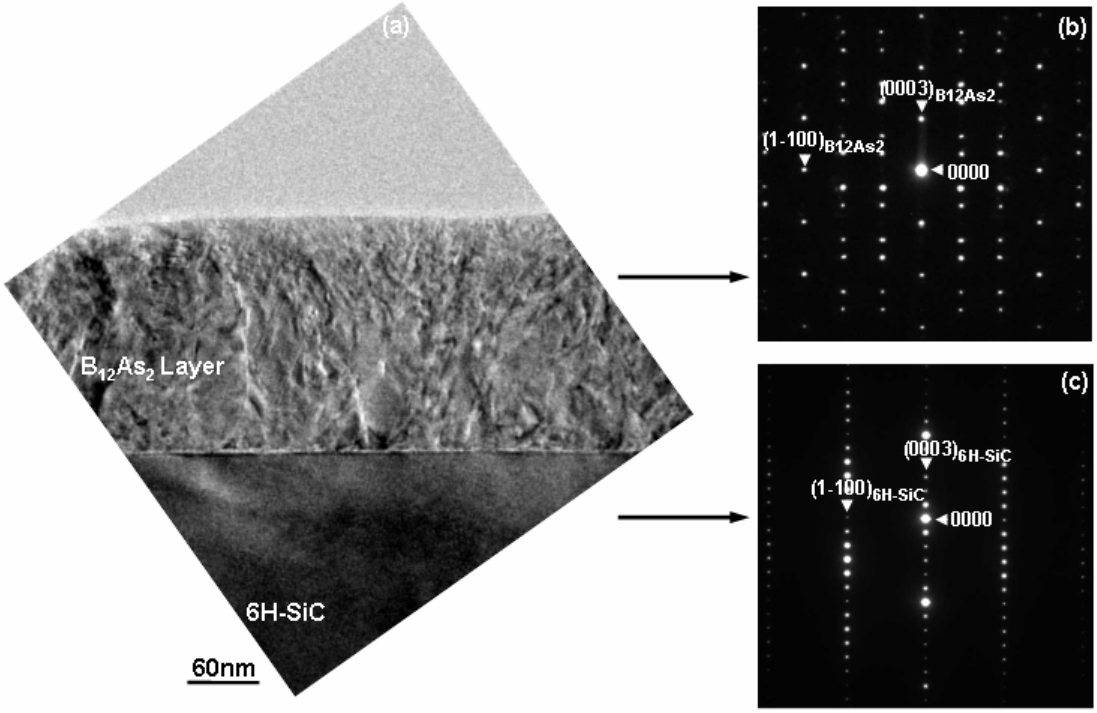

Fig. 25 (a) Cross-sectional TEM image from a sample with $B_{12}As_2$ grown on 3.5° offcut c-plane 6H-SiC, recorded along $[11\bar{2}0]$. (b) SAD pattern of the $B_{12}As_2$ epilayer recorded along the $[11\bar{2}0]$ zone axis. (c) SAD pattern of the 6H-SiC substrate recorded along the $[11\bar{2}0]$ zone axis.

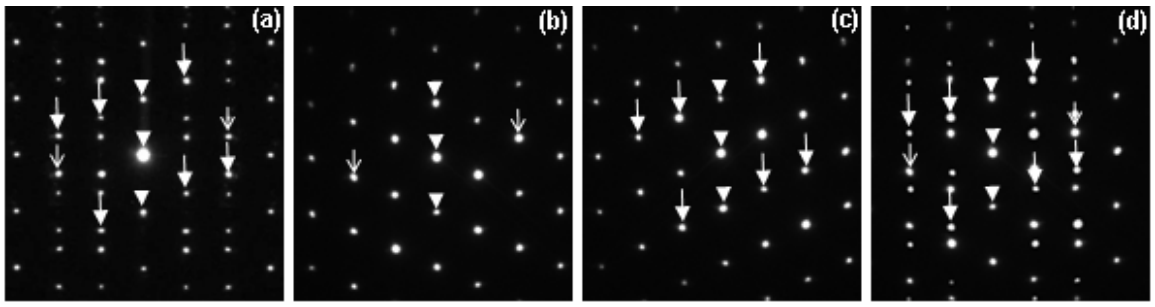

Fig. 26 (a) Experimental SAD pattern of the epilayer recorded along the $[11\bar{2}0]$ zone axis; (b) Simulated SAD pattern of one of the $B_{12}As_2$ twin domains; (c) Simulated SAD pattern of the other $B_{12}As_2$ twin domain; (d) Simulated SAD pattern resulted from the overlap of (b) and (c) showing a combined pattern of $B_{12}As_2$ twinned domains. The spots indicated by ⩛ and ▼ represent diffraction spots from matrix and twin domains, respectively. The diffraction spots indicated by ▼ represent diffraction spots common to both matrix and twin.

HRTEM is utilized to provide information on the atomic configurations present in the various domains and the boundaries between them. Fig. 27(a)-(b) show the cross-sectional

HRTEM observation recorded from an area near the film/substrate interface. Compared with the observation in Fig. 11(a)-(d), the HRTEM projection in Fig. 27(b) displays more complicated features which indicate possible overlap between more than one $B_{12}As_2$ structural variants (as proposed in Chapter 3) projected along [11-20] zone axis. This is confirmed by considering the overlap between two rotational variants, related by a 180^o twin rotation about the (0001) $_{B12As2}$ plane normal, mutually shifted by a $1/6[1\bar{1}00]_{B12As2}$ translation as shown in Fig. 28(a)-(d). The bright spots marked by the dotted circles in both the structural projection image (Fig. 28(a)) and the experimental image (Fig. 28(b)) arise from neighboring B columns in one of the $B_{12}As_2$ twin domains. Meanwhile, the ones marked by the solid circles in both the structural projection image (Fig. 28(c)) and the experimental image (Fig. 28(d)) arise from neighboring B columns in the other $B_{12}As_2$ twin domain. The Moiré pattern can be thus formed by the overlap, along the $[11\bar{2}0]_{B12As2}$ electron imaging direction, between the HRTEM images mutually shifted by a $1/6[1\bar{1}00]_{B12As2}$ translation, as shown in Fig. 28(e). Though a horizontal shift exists between the two rotational variants, the circled regions in the twin domains can exactly superimpose on each other, which then give rise to the much stronger projections surrounded by the solid circles than other features in Fig. 28(e). This is consistent with the experimental observation from the circled projections in Fig. 27(b). Two types of twin boundaries, the unstable high energy TBI and stable low energy TBII ({111} twin boundary), which have been discussed in Chapter 3, are also discerned in the growth on this offcut sample (Fig. 29).

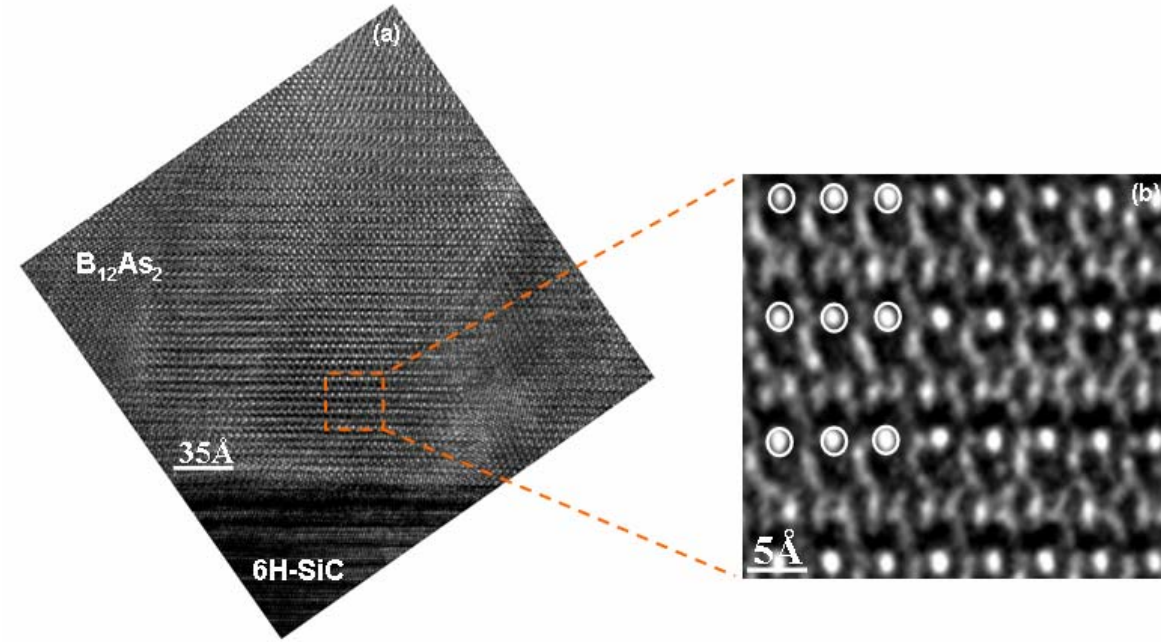

Fig. 27 (a) HRTEM image taken along [11-20] showing the film/substrate interface. (b) Amplified image of the enframed dotted region in (a).

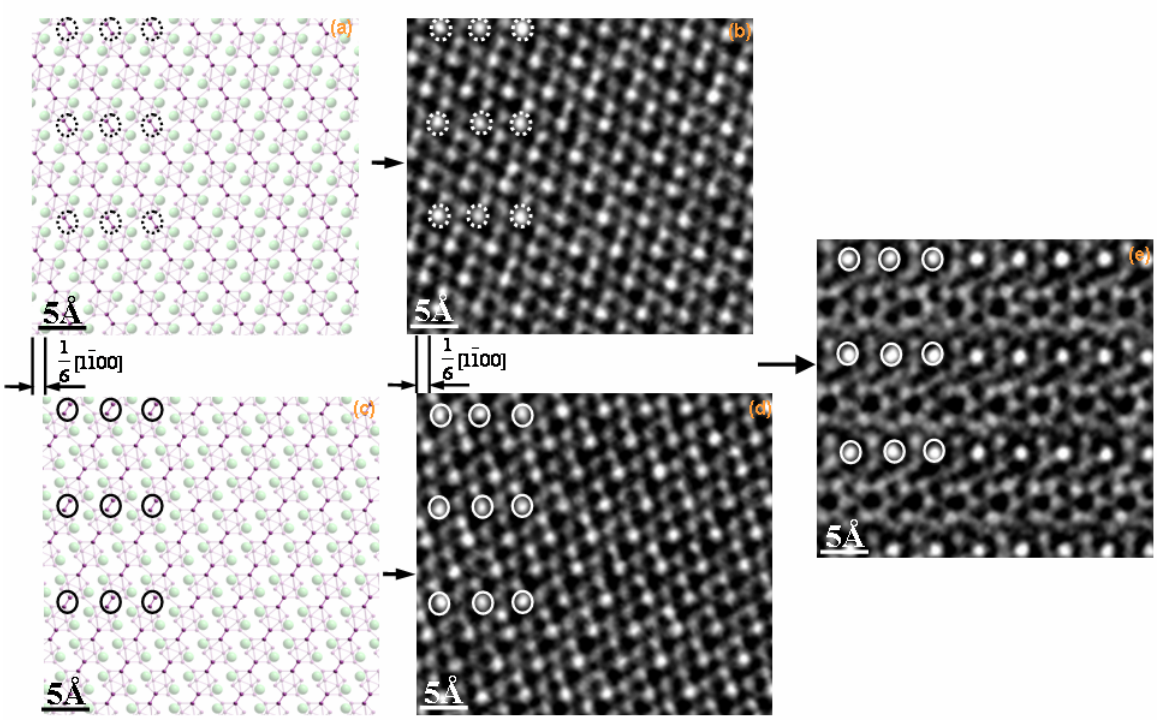

Fig. 28 (a) Crystal visualization of a $B_{12}As_2$ domain projected along [11-20]. (b) Corresponding HRTEM image, taken along [11-20], to Fig. (a). (c) Crystal visualization of a twinned $B_{12}As_2$ domain projected along [11-20]. (d) Corresponding HRTEM image to Fig. (c). (e) Simulated Moiré pattern produced from the superimposition of Figs. (b)&(e), each of which has a 1/6[1-100] mutual shift with respect to each other.

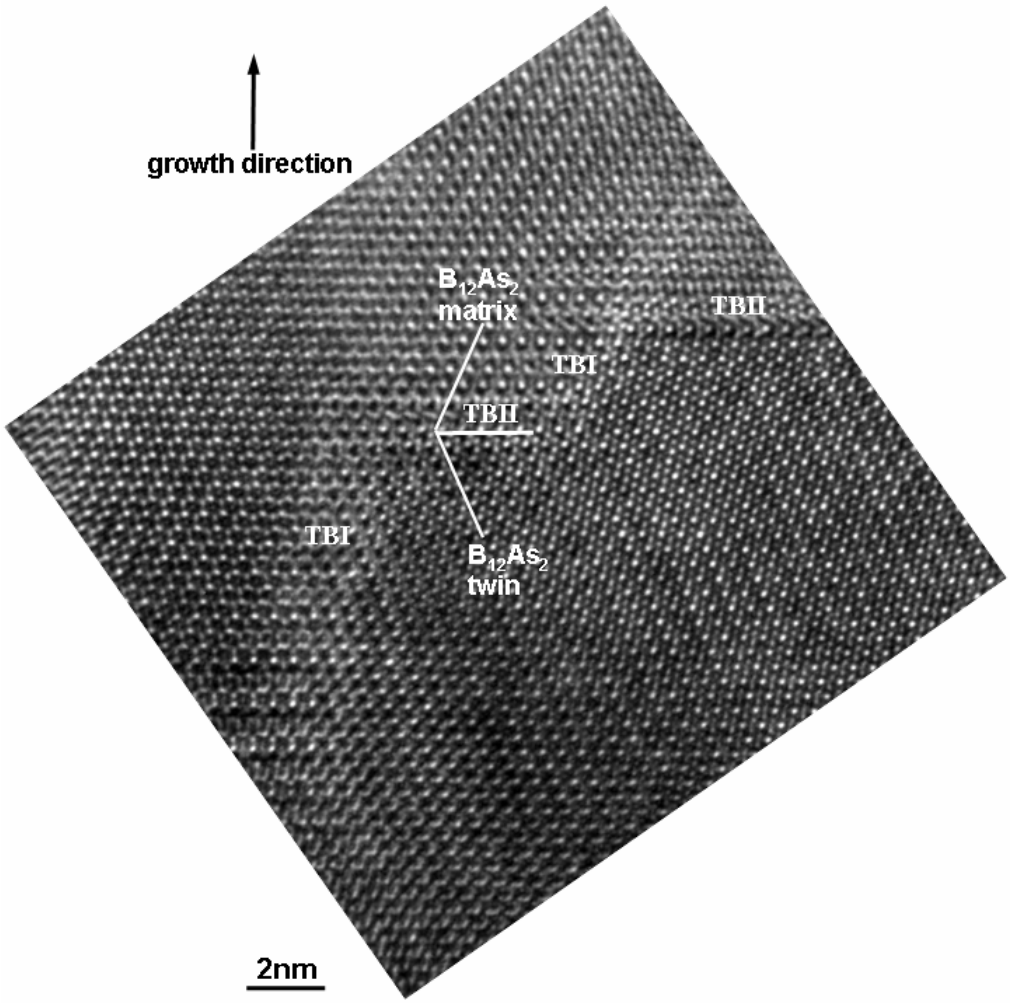

Fig. 29 HRTEM image taken along [11-20] showing two types of $B_{12}As_2$ twin boundaries (TBs) in the epilayer grown on 3.5° offcut c-plane 6H-SiC.

4.4.3. Growth mechanism

In order to understand why and how the structural variants are still present in the epilayer after adopting an offcut angle on the substrate surface, it is important to consider the possible bonding configurations between the film and the substrate. Using a similar approach, HRTEM of the epilayer is used to investigate the detailed atomic configurations present in the various domains and at the various interfaces between them. In addition, comparison of the HRTEM images with models of the potential bonding configurations available at the various nucleation sites on the offcut (0001) 6H-SiC surface provides deeper insight into the nucleation and growth mechanisms of the $B_{12}As_2$ film.

Looking into the nature of the substrate surface, one can find that periodic step risers, which connect each neighboring (0001) closed packed terraces, have to appear on the substrate surface to compensate the 3.5° off-cut angle. If a step riser with one Si-C bilayer height is considered, it is expected that each step appears periodically on the substrate surface with a width of 15 layers each of which is spaced by (3-300) planes (Fig. 30(a)-(b)).

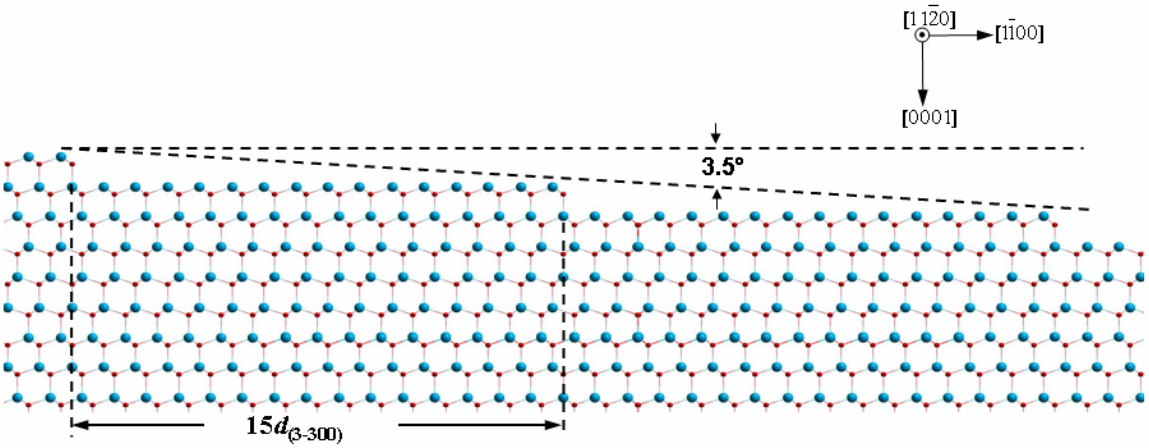

(a)

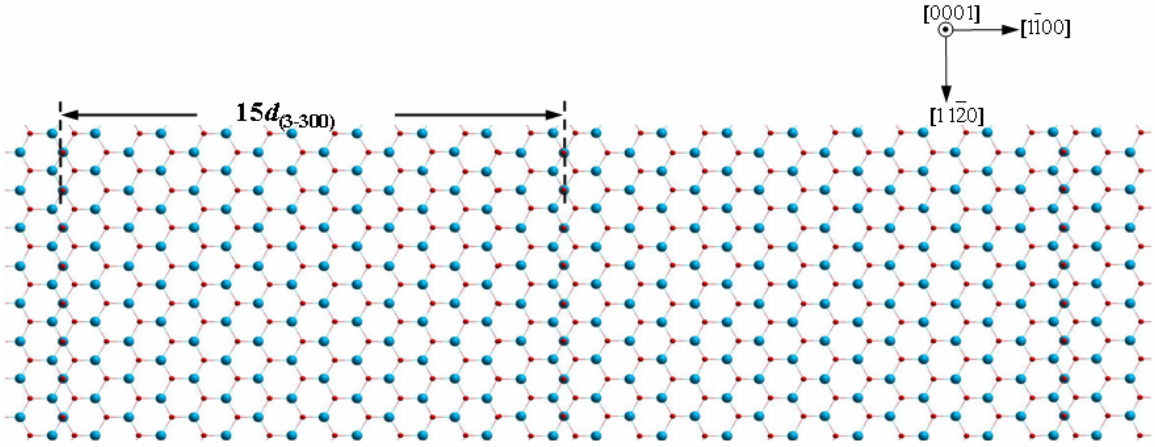

(b)

Fig. 30 (a) [11-20] projection of 3.5° offcut c-plane 6H-SiC substrate showing the periodic atomic steps on its surface. (b) Plan view of 3.5° offcut c-plane 6H-SiC substrate surface.

A similar approach related to the possible nucleation sites for the growth of $B_{12}As_2$, presented in Chapter 3.4.3., can also be adopted for the growth on each terrace exposed on the offcut substrate surface. If the substrate surface is Si-faced, one can expect triangular Si dangling bonds exposed on the substrate surface which can offer possible bonding configuration for $B_{12}As_2$ to nucleate. As stated in Chapter 3.4.3., the triangular configurations of boron atoms that constitute the lower ends of the icosahedra can offer a triangular set of boron dangling bonds. These triangular configurations of boron atoms form a hexagonal network which can be bonded by the triangular Si configurations presented at sites such as those labeled A_1 in Fig. 31(a). Simultaneously, the As atoms can be bonded (which has been shown on Fig. 15(a)) by the Si atoms located at the centers of those triangular configurations, made up from A_1 sites, which have their apexes pointing left (Fig. 31(a)). In consequence, all of the dangling bonds on both the substrate surface and the epilayer surface can be accommodated and thus such a scheme of bonding configuration is reasonable. For this same orientation of B triangle (i.e. with apex pointing left), there are three other possible sites which allow similar bonding to the Si atoms, shown in Fig. 31(a) as A_2, A_3 and A_4, each of

which has a mutual shift of $1/6<11\bar{2}0>_{B12As2}$ from the A_1 sites. On the other hand, B triangles in twinned orientation (i.e. with apexes pointing right) can be bonded in a similar way to Si triangles on the four sites marked as A'_5, A'_6, A'_7 and A'_8 in Fig. 31(b), which are shifted by multiples of $1/12<1\bar{1}00>_{B12As2}$ from the A_1 sites. Direct evidence of such rotational variants can be seen from the TBs in Fig. 29. As a result, there are eight distinct nucleation sites in total. According to this bonding analysis, it can be seen that though each step on the 3.5° offcut substrate surface is significantly narrower than the atomically flat single terrace of the on-axis c-plane 6H-SiC surface, it is wide enough to provide eight possible nucleation sites for $B_{12}As_2$ to nucleate, which then give rise to the eight possible structural variants in the film.

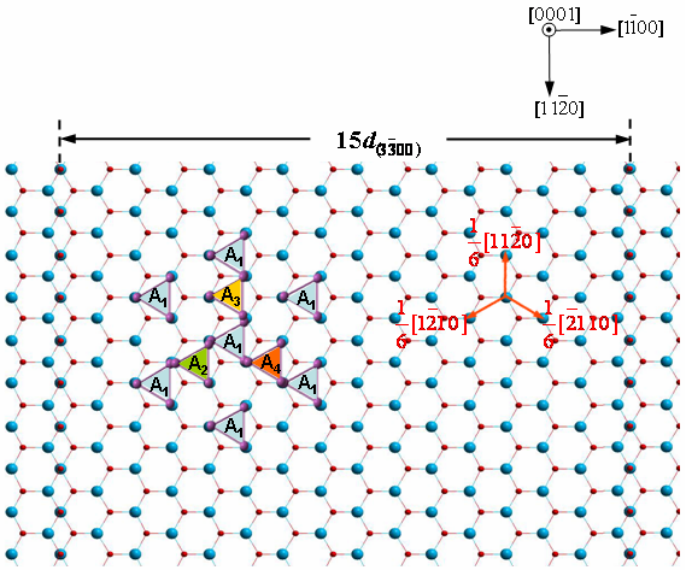

(a)

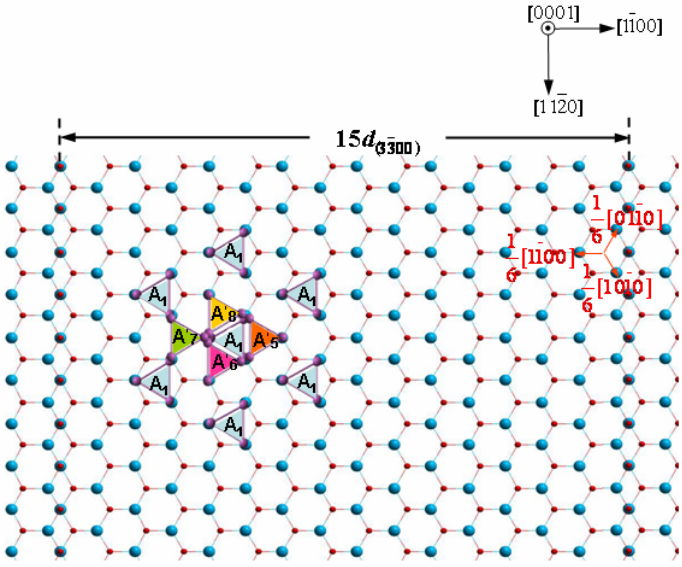

(b)

Fig. 31 (a) Plan view of four possible translationally variant $B_{12}As_2$ nucleation sites (A_1, A_2, A_3 and A_4) on the 3.5 ° off-cut Si-face (0001) 6H-SiC. Si atoms are exposed on the step surface while C atoms are located beneath the Si atoms. (b) Plan view of the four possible rotationally variant nucleation sites (A'_5, A'_6, A'_7 and A'_8) for $B_{12}As_2$ in twinned orientation.

4.5. Conclusions

$B_{12}As_2$ epitaxial layer grown on a 3.5° off-cut (0001) 6H-SiC substrate is characterized by using SWBXT, SEM, conventional and high resolution TEM. Similar to the growth on on-axis c-plane 6H-SiC, the epitaxial relationship is also identified to be $(0001)_{B12As2}< 11\bar{2}0 >_{B12As2}||(0001)_{6H\text{-}SiC}< 11\bar{2}0 >_{6H\text{-}SiC}$. It is also revealed that the epilayer consists of a solid solution of $B_{12}As_2$ twinning domains. The 3.5° off-cut angle breaks the surface symmetry of c-plane 6H-SiC, but the surface steps are wide enough to provide eight possible nonequivalent nucleation sites so as to accommodate various structural variants for the growth of $B_{12}As_2$. Consequently, the offcut angle has little effect in the reduction of possible structural variants in the epilayer and thus may not be an excellent substrate to grow high quality $B_{12}As_2$ film.

5. $B_{12}As_2$ grown on m-plane (1-100) 6H-SiC

5.1. Outline

Microstructure of $B_{12}As_2$ epitaxial layers grown on m-plane 6H-SiC substrates has been studied with the aid of optical microscopy, SEM, SWBXT and HRTEM. Multiple domains, including (1-21) $B_{12}As_2$, (2-12) $B_{12}As_2$, (353) $B_{12}As_2$ and their respective twins, are found to exist in the epilayer. The choice of the various growth orientations are suggested to arise from several factors: (1) the tendency for $B_{12}As_2$ to grow with a low energy surface orientation; (2) the tendency to reduce the in-plane lattice mismatch between $B_{12}As_2$ planes oriented approximately parallel to the SiC (0001) planes to minimize local strain in the film/substrate interface; (3) the tendency to nucleate on closed-packed atomic facets on the substrate surface.

5.2. Introduction

Growth of a lower symmetry epilayer on a higher symmetry substrate often produces a mixture of structural variants (rotational and translational) in the film, a phenomenon which has been referred to as degenerate epitaxy. A numeration of these variants can be obtained by analysis of the 2D point groups of the substrate surface and the epilayer surface which grows on the particular substrate orientation. For the growth on c-plane 6H-SiC, as analyzed in Chapter 3, only polycrystalline films with a high density of defects and numerous $B_{12}As_2$ twin boundaries are possible, as the films adopt multiple orientations (involving both translational and rotational) relative to the substrate. Consequently, finding a suitable substrate is a key strategy to grow single crystalline $B_{12}As_2$. The influence of the substrate surface symmetry on the generation of structural variants can be diminished by the presence of facets which can break up the symmetry of the surface. For example the use of offcut substrates potentially enables manipulation of the relative populations of the multiple variants although such studies on offcut (0001) 6H-SiC substrates have so far been largely unsuccessful.[Error! Bookmark not defined.] An alternative strategy is to use substrates with completely different orientation, for example, a-plane and m-plane 6H- SiC, or similarly oriented substrates of a different polytype such as 15R. According to the epitaxial relation of the growth on c-plane 6H-SiC, it's expected that $B_{12}As_2$ would adopt (1-21) growth orientation on m-plane 6H-SiC. The surface symmetry of the m-plane 6H-SiC and the one of (1-21) $B_{12}As_2$ are both *m*, as illustrated in Fig. 32, in which {11-20} mirror planes are shown to exist in both $B_{12}As_2$ and 6H-SiC. Based on the degenerate study of possible rotational variants by Chan *etc*, it's predicted that only one rotational variant will be present in the film grown on m-plane 6H-SiC. In consequence, m-plane 6H-SiC has been attempted to grow single crystalline $B_{12}As_2$.

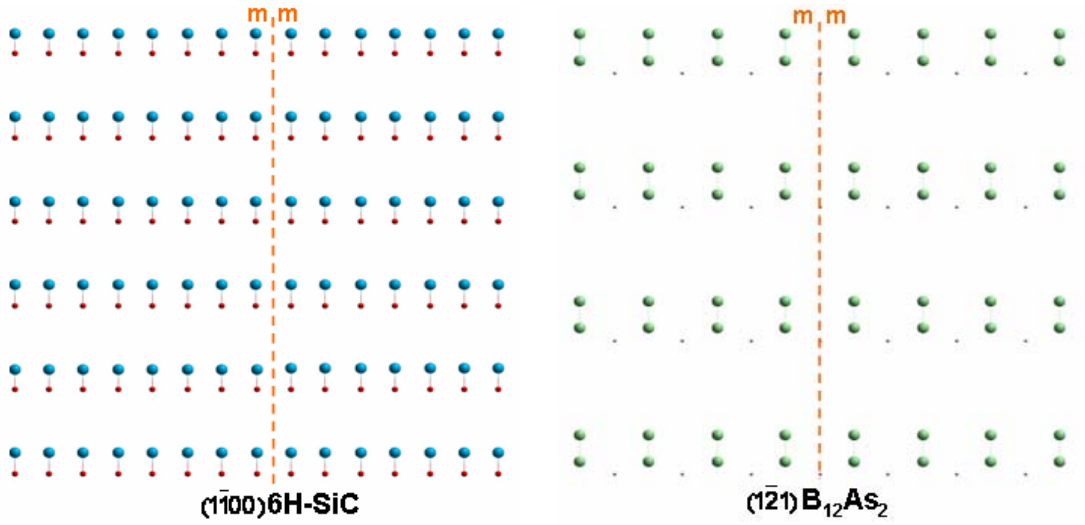

(a) (b)

Fig. 32 Surface symmetry of (a) m-plane 6H-SiC and (b) (1-21) $B_{12}As_2$.

5.3. Experimental

A commercially available (1-100) 6H-SiC substrate was used for the CVD growth of $B_{12}As_2$. SWBXT revealed the presence of (1-100) 15R-SiC inclusions exposed on the surface of this substrate, which will be discussed later in Chapter 6. The $B_{12}As_2$ film was synthesized with gaseous precursors of 1% B_2H_6 in H_2 and 2% AsH_3 in H_2. The $B_{12}As_2$ was deposited at 1200°C and 500 Torr of reactor pressure for 60 minutes. The epitaxial $B_{12}As_2$ film had a nominal thickness of 3 µm. The cross-sectional TEM samples were made parallel to $(\mathbf{11\bar{2}0})_{6H\text{-}SiC}$ since this orientation clearly reveals the $B_{12}As_2$ twin boundaries. The sample was mechanically thinned down and polished using the standard T-tool technique employing 30 µm, 15 µm, 6 µm, 3 µm, 1 µm and 0.5 µm diamond lapping films and then ion milled to electron transparency. High resolution TEM was carried out using a JEOL 3000EX system (300KeV) and JEOL 4000F system (400KeV) at the Center for Functional Nanomaterials at Brookhaven National Laboratory. SWBXT was performed on as-grown films at the Stony Brook synchrotron topography facility at the National Synchrotron Light Source. It was utilized to determine the epitaxial relationships involved during the epitaxy of $B_{12}As_2$ on both 6H-SiC and 15R-SiC. Small incident beam area (0.5mm x 0.5mm) enabled the films grown on the 6H region and the 15R region to be examined separately. Furthermore, diffraction patterns from both regions were overexposed (by a factor of 10-12) in order to maximize the intensity from the more diffuse $B_{12}As_2$ diffraction spots. The transmission Laue patterns were recorded on Kodak SR5 X-ray films at a sample to film distance of 15cm.

5.4. Results and discussion

5.4.1. SWBXT, optical and SEM results

Fig. 33 shows the transmission synchrotron x-ray Laue patterns recorded from the $B_{12}As_2$ epitaxial layers grown on the m-plane 6H-SiC region. The 6H-SiC produced well

defined, strong diffraction spots while the $B_{12}As_2$ produced only diffuse, weak and streaked diffraction spots indicative of mosaicity. The $B_{12}As_2$ diffraction spots are labeled with the polytype of the SiC that they are grown on (in this case 6H, in order to compare with the SWBXT Laue pattern from 15R region in Chapter 6), the rhombohedral (*hkl)* indices of the $B_{12}As_2$, and with superscripts indicating the growth orientation of the $B_{12}As_2$. Detailed indexing analysis shows that the polycrystalline nature of the $B_{12}As_2$ film in this region with four distinct orientations: (1-21) and its twin, (-12-1); (2-12) and its twin, (010). The twin orientations are related by a 180^o (or equivalently 60^o) rotation about the (111) plane normal (for the (1-21) grains the [111] twin axis is parallel to the substrate surface while in the (2-12) grain it is oriented at an angle of 24° to the surface). Although the film completely covers the substrate, the area of the $B_{12}As_2$ diffraction spots appears different from that of the SiC spots due to the presence of mosaicity in the film. This leads to an overall divergence in the diffracted beams emanating from the various $B_{12}As_2$ grains leading to a mostly radial asterism or streaking on the film. The $B_{12}As_2$ spots have much lower intensities and are more diffused than those recorded from the film grown on m-plane 15R-SiC (as will be discussed in Chapter 6). This effect is mostly due to the fact that the diffracted intensities from the film grown on the m-plane 6H-SiC are divided amongst more different types of domain. Optical observation (Fig. 34) and SEM observation (Fig. 35) revealed the rough surface and polycrystalline domains (a few μm wide) of the film, which agree with the result from SWBXT. Detailed investigation of the microstructures of the films is carried out using cross-sectional HRTEM.

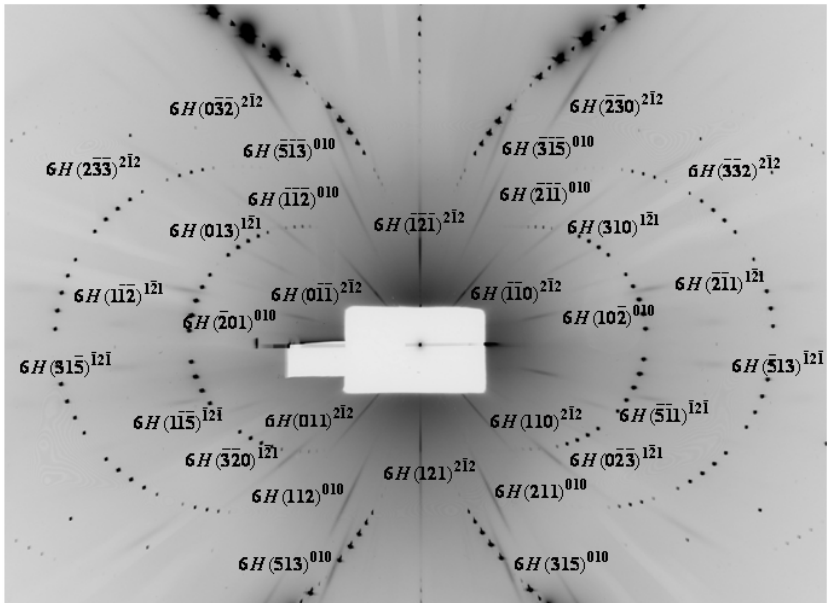

Fig. 33 Transmission Laue pattern of a pure 6H area showing the presence of (1-21) $B_{12}As_2$, (2-12) $B_{12}As_2$ and their corresponding twins (-12-1) and (010).

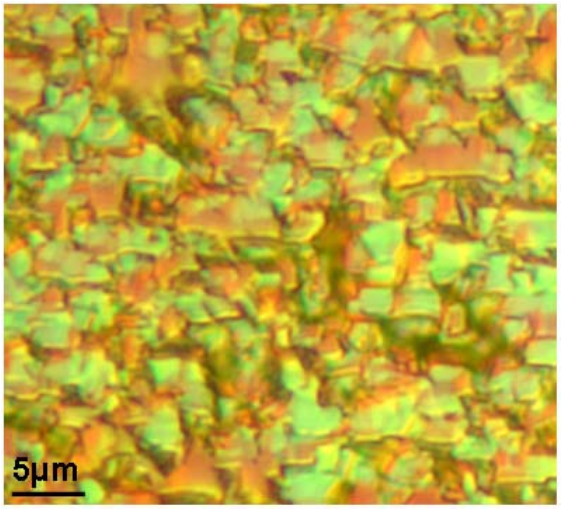

Fig. 34 Optical micrograph of the surface of the $B_{12}As_2$ epilayer grown on 6H-SiC.

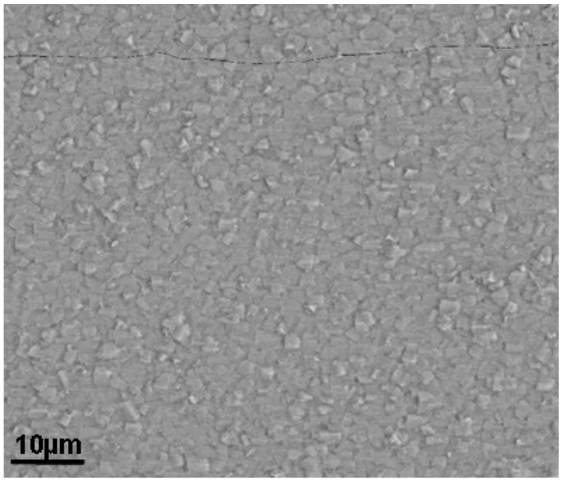

Fig. 35 SEM image showing the polycrystalline surface morphology of the $B_{12}As_2$ epilayer grown on m-plane 6H-SiC.

5.4.2. TEM results

Cross-sectional HRTEM observation along the [**11$\bar{2}$0**] zone axis reveals an approximately 5 nm thick transition layer between the film and the substrate, as shown in Fig. 36(a)&(b). Detailed and accurate measurements of inter-planar angles confirm the existence of $B_{12}As_2$ grains of (1-21) and (2-12) surface orientations, and their respective {111} twins. Evidently, the (1-21) $B_{12}As_2$ twin domains have the (111) twinning plane parallel to the growth direction (Fig. 36(c)) while the (2-12) $B_{12}As_2$ twin domains have the (111) twinning plane tilted from the growth direction by around 24^o (Fig. 36(d)). In addition, lamella like narrow twinning bands consisting of one to a few atomic layers are occasionally observed, such as shown in Fig. 36(d)&(e). Thus the growth orientations obtained from HRTEM are consistent with those from SWBXT. Furthermore, the HRTEM observation from Fig. 36(c) also reveals the presence of (353) $B_{12}As_2$ and its twin, (212) $B_{12}As_2$. Based on the HRTEM observation, these three types of domain structures generated by the twinning processes can

be represented schematically in Fig. 37(a)-(c). As a result, the $B_{12}As_2$ on m-plane 6H-SiC has grown with six distinct orientations rather than the expected single growth orientation. Further detailed comparison between the HRTEM images recorded from the films and CaRine structural projections provides much insight into the operative growth mechanisms.

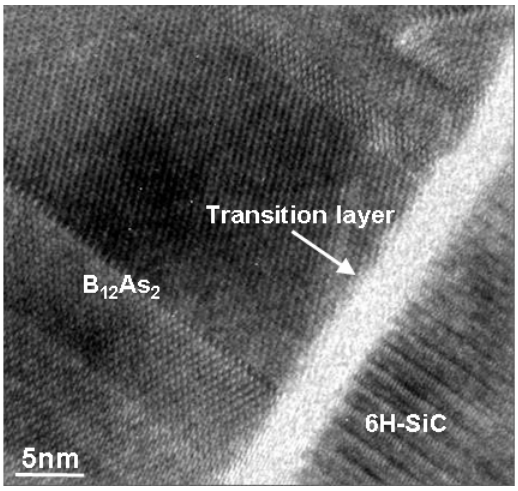

(a)

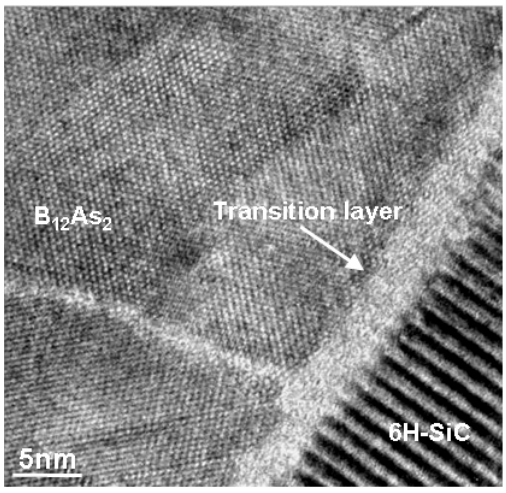

(b)

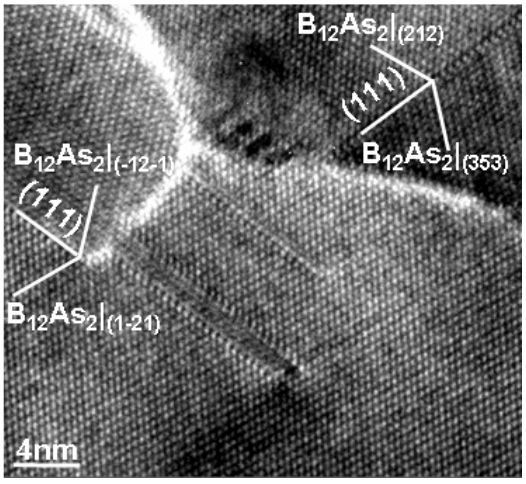

(c)

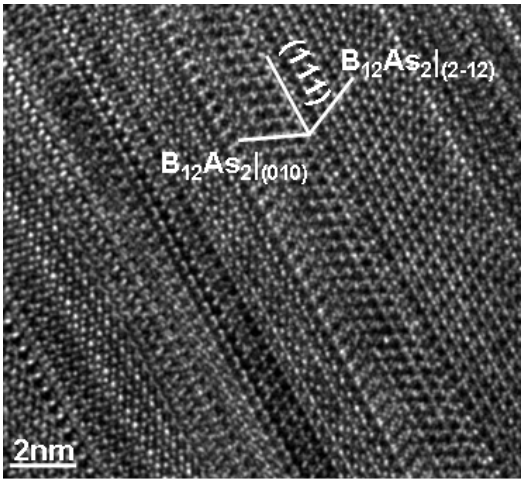

(d)

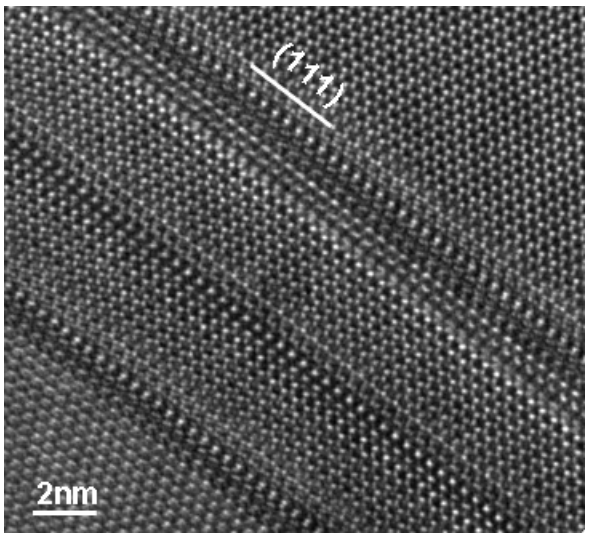

(e)

Fig. 36 HRTEM images from m-plane 6H region taken along [10-1] zone axis. (a) Interface between (1-21) $B_{12}As_2$ twin domains and 6H-SiC; (b) Interface between (353) $B_{12}As_2$ twin domains and 6H-SiC; (c) (1-21) and (353) $B_{12}As_2$ twin domains in the epilayer; (d) (2-12) $B_{12}As_2$ twin domains in the epilayer. (e) Lamella twin bands of (1-21) $B_{12}As_2$ twin domains in the epilayer.

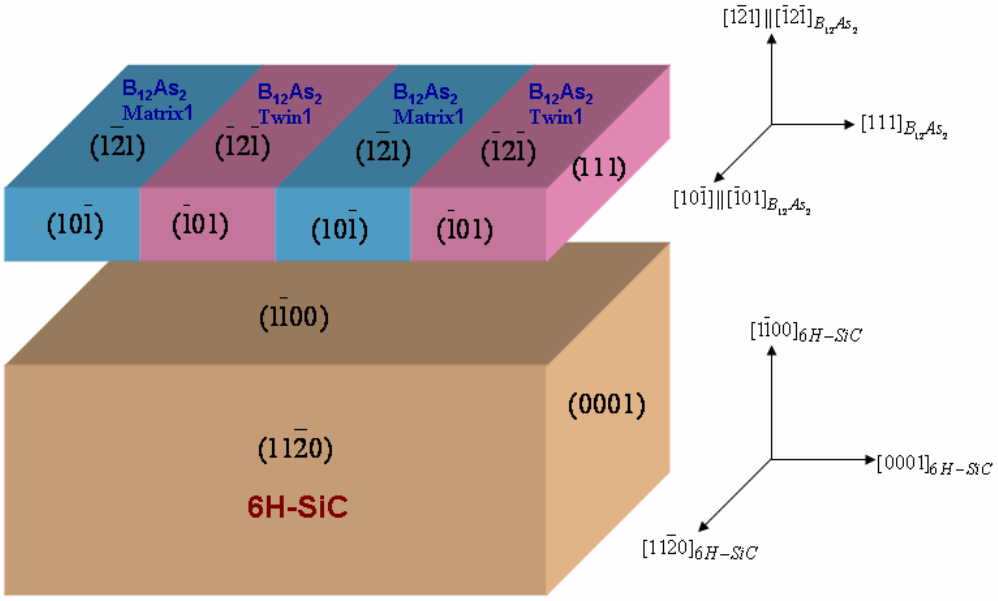

(a)

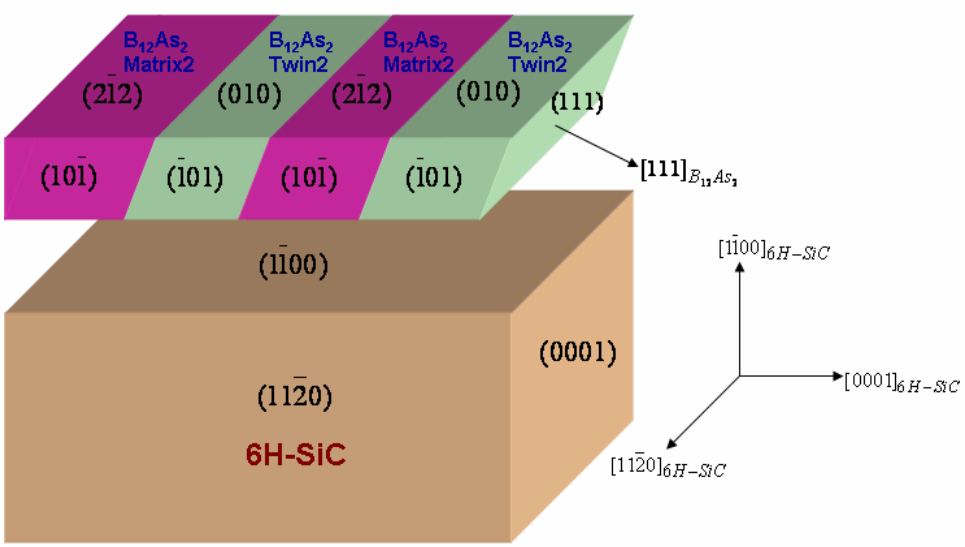

(b)

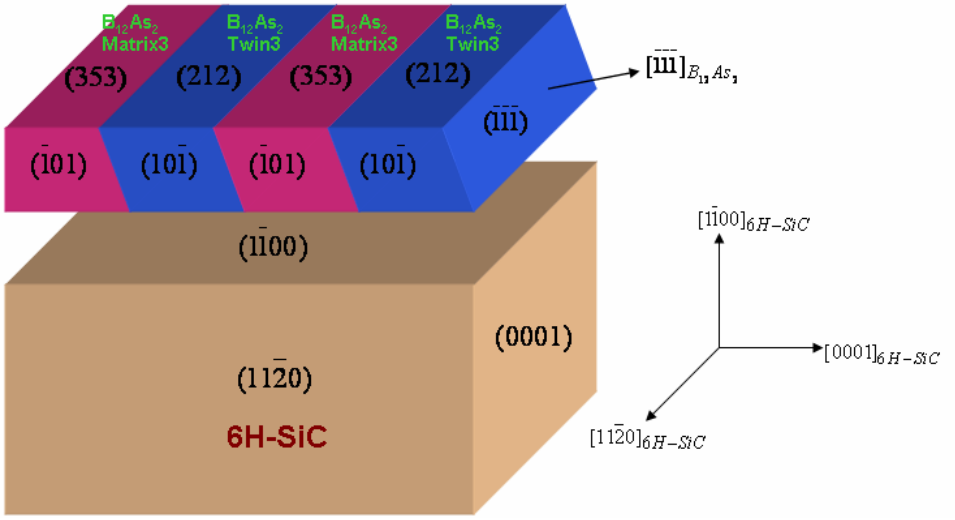

(c)

Fig. 37 Schematics of (a) (1-21) $B_{12}As_2$ twin domains grown on m-plane 6H-SiC, (b) (2-12) $B_{12}As_2$ twin domains grown on m-plane 6H-SiC and (c)) (353) $B_{12}As_2$ twin domains grown on m-plane 6H-SiC.

5.4.3. Growth mechanism

If considering the theory of degenerate epitaxy, it is predicted that no twinning structures will be present in the epilayer. From Fig. 38, it is shown that each of the (1-21) $B_{12}As_2$, (2-12) $B_{12}As_2$, (353) $B_{12}As_2$ and m-plane 6H-SiC has { **11$\bar{2}$0** } mirror planes (equivalent to {10-1} in rhombohedral system) and exhibits *m* surface symmetry. According to the number of possible rotational variants given in Table 1, there will be only one rotational variant expected for each of the growth orientations, which indicates the absence of twins. In consequence, this theory is conflicted with the experimental results and is not

suitable to be applied to the growth on m-plane 6H-SiC. Then it's necessary to consider other possible factors for the growth mechanisms.

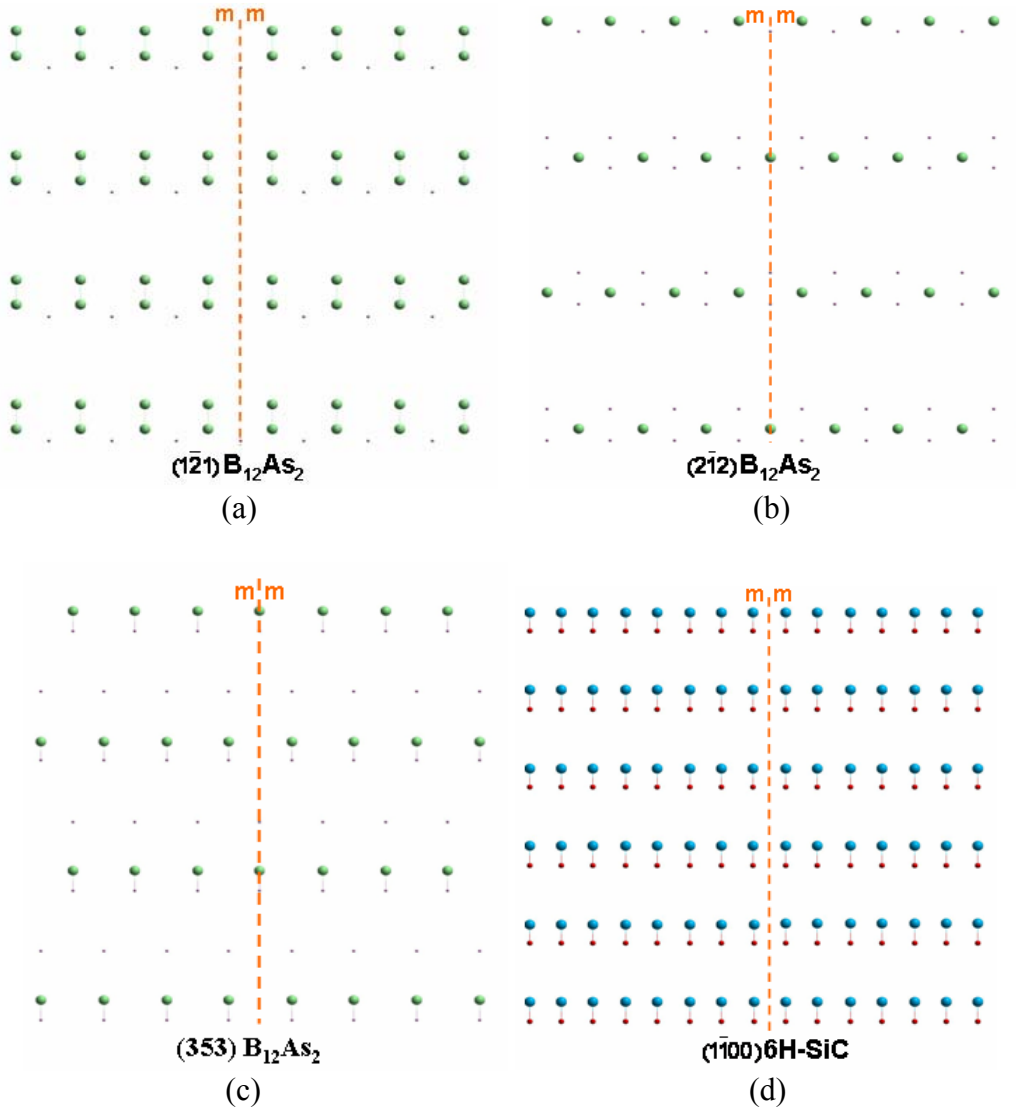

Fig. 38 Projections of (a) (1-21) $B_{12}As_2$; (b) (2-12) $B_{12}As_2$; (c) (353) $B_{12}As_2$ as well as (d) m-plane 6H-SiC showing the surface symmetry of *m*.

If the epitaxial relationship observed in $B_{12}As_2$ films grown on (0001) orientation 6H-SiC (Chapter 3) is preserved for films grown on the m-plane 6H-SiC substrate, one would expect the films to adopt (1-21) orientation and for the film to be twinned (as produced by a 180° rotation about [111]). HRTEM and SWBXT do, in fact, confirm the presence of twinned gains of this orientation. However, (2-12) and (353) as well as their twinned orientations are also observed. In attempting to understand why the other two orientations and their twins should appear, it is vital to consider factors that, in the general case, may potentially contribute to the choice of surface orientation in these heteroepitaxial films. These factors include: (1) the tendency for $B_{12}As_2$ to grow with a low energy surface orientation; (2)

the tendency to reduce the in-plane lattice mismatch between $B_{12}As_2$ planes oriented approximately parallel to the 6H-SiC (0001) planes to minimize local strain in the film/substrate interface; (3) the tendency to nucleate on symmetric closed-packed atomic facets on the substrate surface.

Considering factor (1), SEM of facets observed on $B_{12}As_2$ grown on on-axis and offcut (0001) 6H-SiC has shown that (1-21) and its twinned orientation, (-12-1), are preferred and therefore low energy facets (as shown in Fig. 9&Fig. 23). Thus if $B_{12}As_2$ islands nucleate on the m-plane 6H-SiC substrate in (1-21) twinned orientations, preserving the expected epitaxial relationship, the low energy of the (1-21) surface facet may contribute to the stabilization of that growth orientation.

Considering factor (2), which is related to the film/substrate lattice mismatch, for the (1-21) and its twin orientation, the (111) $B_{12}As_2$ planes align themselves with the (0001) planes of the substrate and the in-plane lattice mismatch between $(111)_{B12As2}$ and $(0003)_{6H\text{-}SiC}$ is 26.3% (Fig. 39(a)), which indicates in this case the film/substrate interface has to endue a large amount of stress and thus strain. In contrast, for the (2-12) orientation, the $(121)_{B12As2}$ planes align themselves approximately parallel (offset by 6°) to the (0001) substrate planes and the in-plane mismatch between $(121)_{B12As2}$ and the $(0006)_{6H\text{-}SiC}$ is dramatically reduced to 3.7%, as shown in Fig. 39(b). Similarly, for the twin orientation of (2-12), (010) $B_{12}As_2$, the $(212)_{B12As2}$ planes are aligned nearly parallel (offset by 1°) to the (0001) substrate planes and the in-plane mismatch between $(212)_{B12As2}$ and the $(0006)_{6H\text{-}SiC}$ is around 5.5% (Fig. 39(b)), which is also significantly smaller than the lattice mismatches in (1-21) and (-12-1) orientations. Meanwhile, for the case of the (353) $B_{12}As_2$, the $(1\text{-}11)_{B12As2}$ planes align themselves nearly parallel (offset by 6°) to the (0001) substrate planes and the in-plane mismatch between $(1\text{-}11)_{B12As2}$ and the $(0006)_{6H\text{-}SiC}$ is as small as 3.4% (Fig. 39(c)), comparable to the one on (2-12) orientation. (212) $B_{12}As_2$, the twin of (353) $B_{12}As_2$, has $(010)_{B12As2}$ planes lining up with $(0003)_{6H\text{-}SiC}$ and the lattice mismatch is around 3.7% (Fig. 39(c)). As a conclusion, from the point of lattice mismatch, (2-12), (353) and their twin orientations have apparent advantages over (1-21) and its twin during the Epitaxial growth. Therefore, minimization of in-plane lattice mismatch to reduce local strain may account for the presence of (2-12), (353) and their twin orientations on the m-plane 6H-SiC substrate.

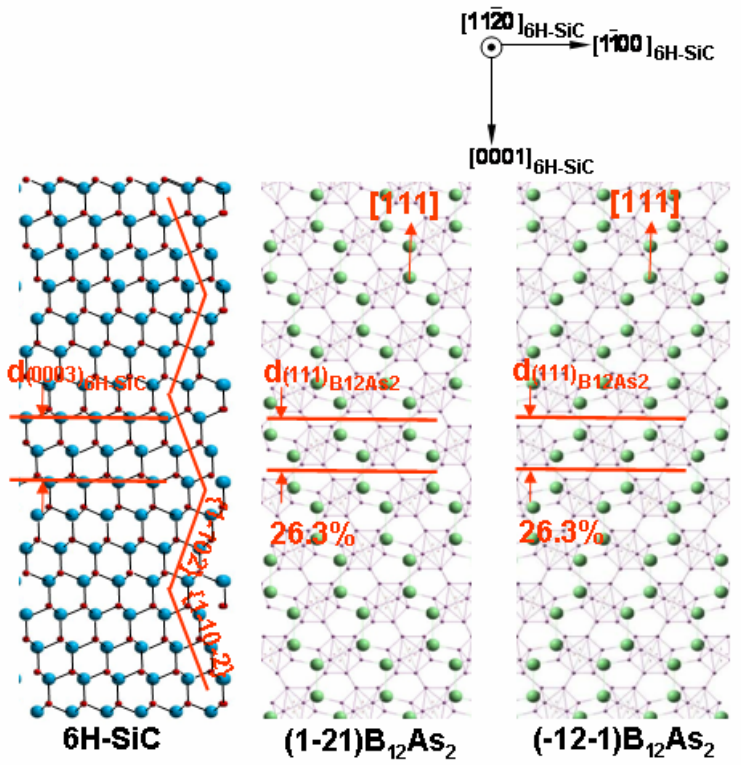
[11$\bar{2}$0]6H-SiC
[1$\bar{1}$00]6H-SiC
[0001]6H-SiC
[111]
[111]
d(0003)6H-SiC
d(111)B12As2
d(111)B12As2
26.3%
26.3%
6H-SiC
(1-21)B12As2
(-12-1)B12As2

(a)

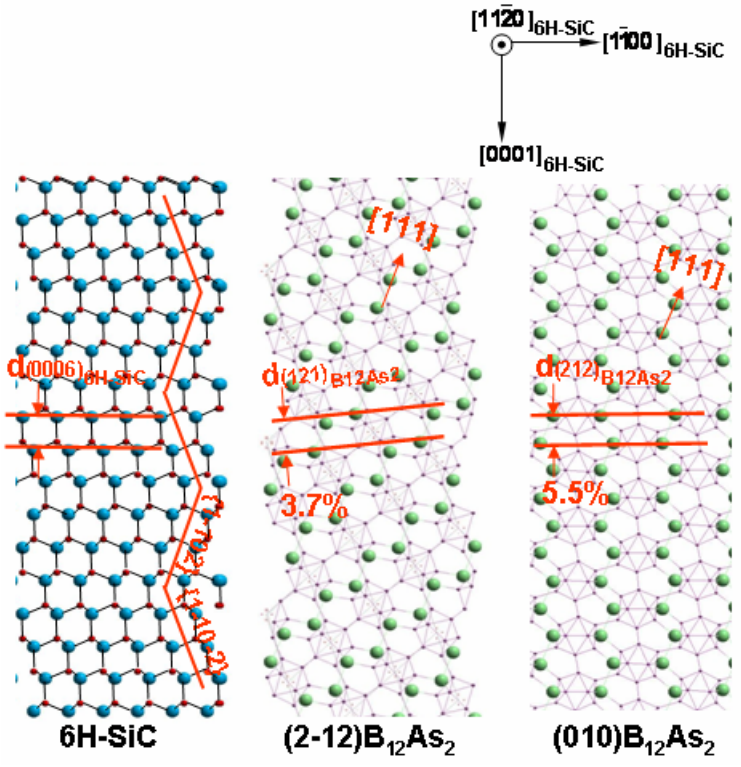
[11$\bar{2}$0]6H-SiC
[1$\bar{1}$00]6H-SiC
[0001]6H-SiC
[111]
[111]
d(0006)6H-SiC
d(121)B12As2
d(212)B12As2
3.7%
5.5%
6H-SiC
(2-12)B12As2
(010)B12As2

(b)

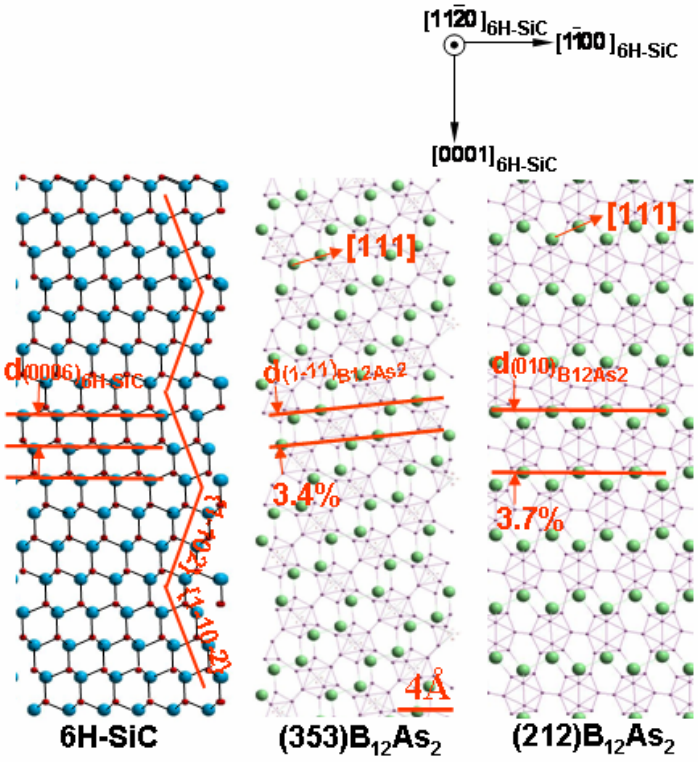

(c)

Fig. 39 Crystal visualization along [11-20] showing the film/substrate lattice mismatch in (a) (1-21) $B_{12}As_2$ and (-12-1) $B_{12}As_2$; (b) (2-12) $B_{12}As_2$and (010) $B_{12}As_2$; (c) (353) $B_{12}As_2$ and (212) $B_{12}As_2$.

Looking deeper into the nature of the formation of (353) $B_{12}As_2$ and its twin, (212) $B_{12}As_2$, factor (3), the tendency to nucleate on symmetric closed-packed atomic facets on the substrate surface needs to be considered as well. Viewed along [11-20], m-plane 6H-SiC follows a symmetric 3-3 stacking sequence (Fig. 40). Hydrogen etched prior to growth, m-plane 6H-SiC is expected to display a faceted structure featuring two types of equal area, close-packed facets, (1-102) and (1-10-2), which are three bilayers wide and form a symmetric corrugation on the surface (Fig. 40). Thus the substrate surface offers two types of possible nucleation terraces with equal width which can accommodate the large dimension of the in-plane repeat unit of the $(111)_{B12As2}$ (twice that of the close-packed SiC planes).

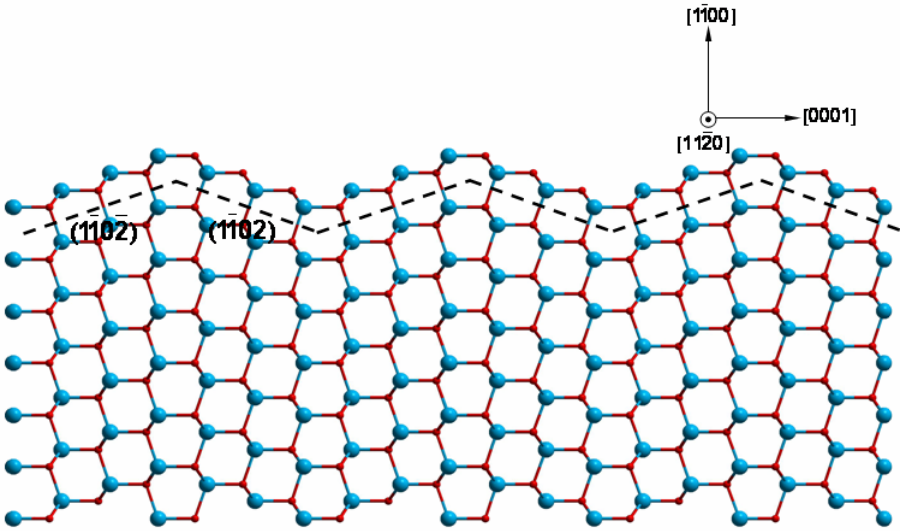

Fig. 40 Projections of m-plane 6H-SiC, viewed along [11-20], showing symmetric 3-3 atomic steps on the substrate surface.

If the C-face (1-102) terraces are considered for nucleation, the (111) planes of the $B_{12}As_2$ orient themselves parallel to the (1-102) facet planes of the 6H-SiC substrate and would result in the (353) surface orientation (Fig. 41) or (212) orientation. In this case, (353) $B_{12}As_2$ is proposed to be much more preferred than (212) $B_{12}As_2$ by considering the in-plane lattice mismatch on the closed-packed substrate facets. Fig. 42(a)-(c) shows the plan view of the top surface of the 6H-SiC with C-face (10-12) planes, the bottom surfaces of (353) $B_{12}As_2$ and (212) $B_{12}As_2$ constructed by the boron triangular configurations which contribute to the atomic bonding between the film and the substrate (see Chapter 3). Apparently, the in-plane lattice mismatch in (353) $B_{12}As_2$ (~1.8%) is much smaller than the one in (212) $B_{12}As_2$ (~12.7%). This indicates the formation of (353) $B_{12}As_2$ would be more favorable than (212) $B_{12}As_2$ for the growth on the C-face (1-102) 6H-SiC surface planes. On the contrary, if the Si-face (1-10-2) terraces are considered for the nucleation of $B_{12}As_2$, the film would adopt (212) surface orientation (Fig. 43) rather than (353) orientation. Similar approach associated with the in-plane film/substrate mismatch on the closed packed substrate terraces can also be applied to this case. As illustrated in Fig. 44(a)-(c), (212) orientation offers a significantly smaller lattice mismatch (~1.8%) than (353) orientation (~12.7%). Therefore, to minimize the strain present in film/substrate interface, (212) $B_{12}As_2$ is more energetically favorable than (353) $B_{12}As_2$ for the growth on Si-face (1-102) substrate facets.

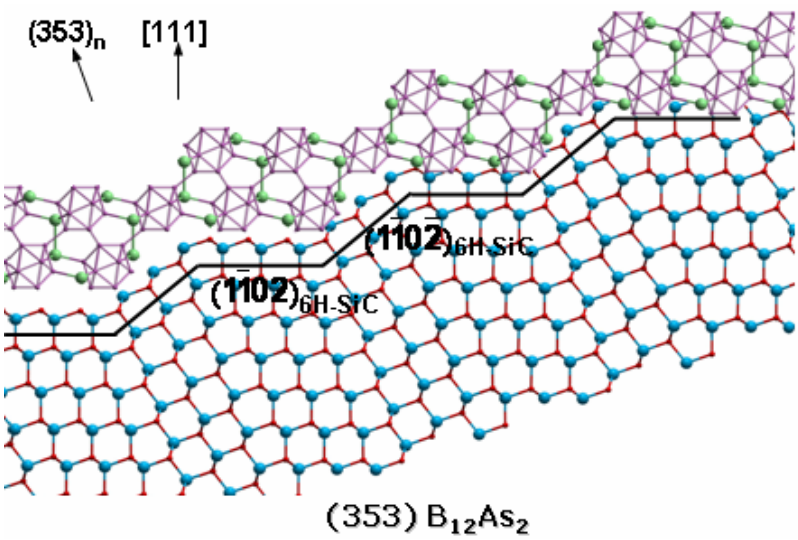

Fig. 41 [10-1] crystal visualization of (353)$B_{12}As_2$ on C-face (1-102) closed packed facets on the m-plane 6H-SiC surface.

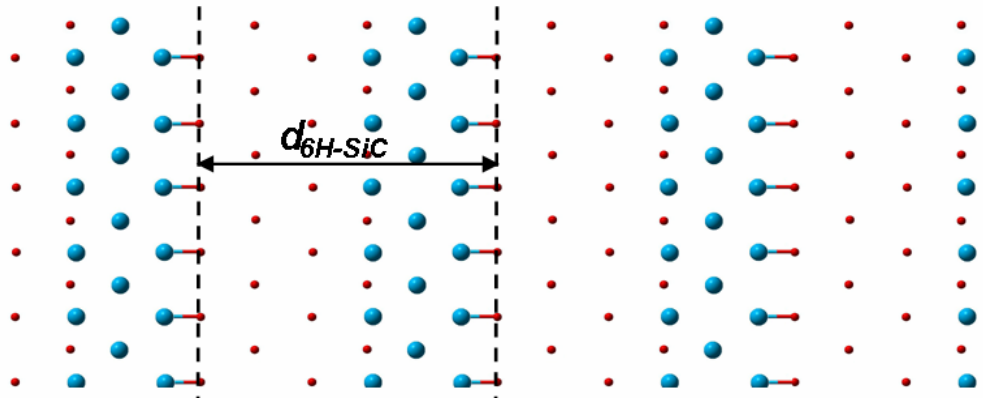

(a)

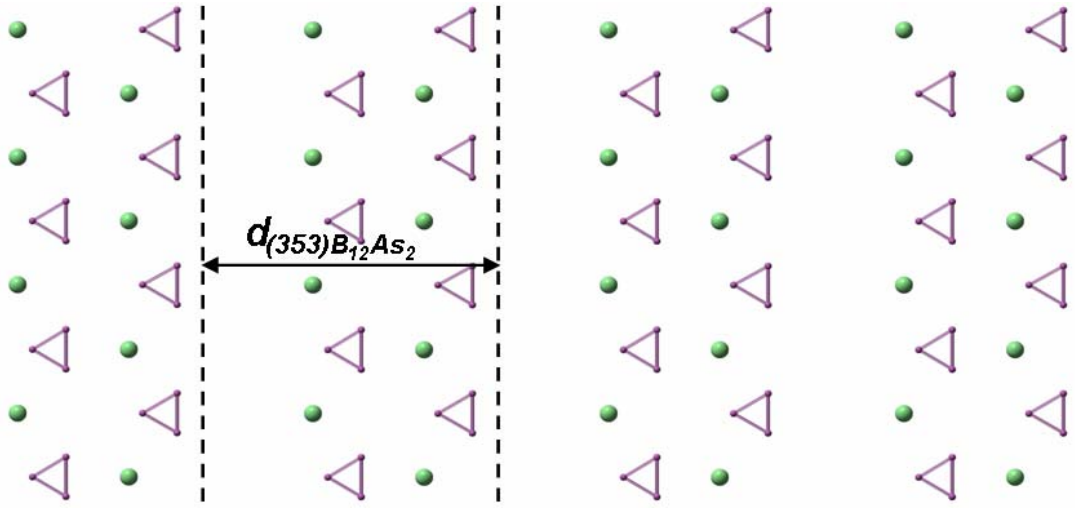

(b)

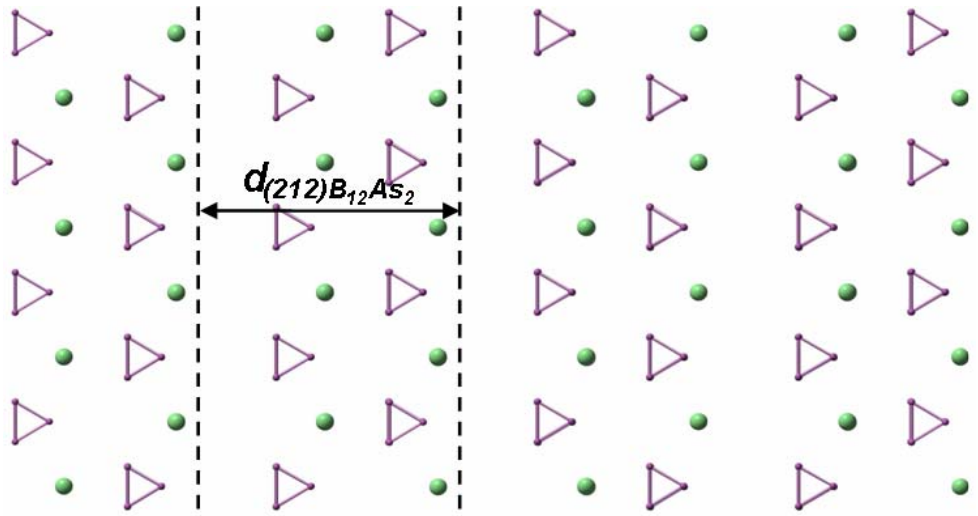

(c)

Fig. 42 $[111]_{B12As2}$ plan view of (a) m-plane 6H-SiC with C-face (1-102) surface steps as nucleation terraces, (b) $(353)B_{12}As_2$ and (c) $(212)B_{12}As_2$, showing the significant difference between the lattice mismatch of (353) $B_{12}As_2$/15R-SiC and the one of (212) $B_{12}As_2$/15R-SiC.

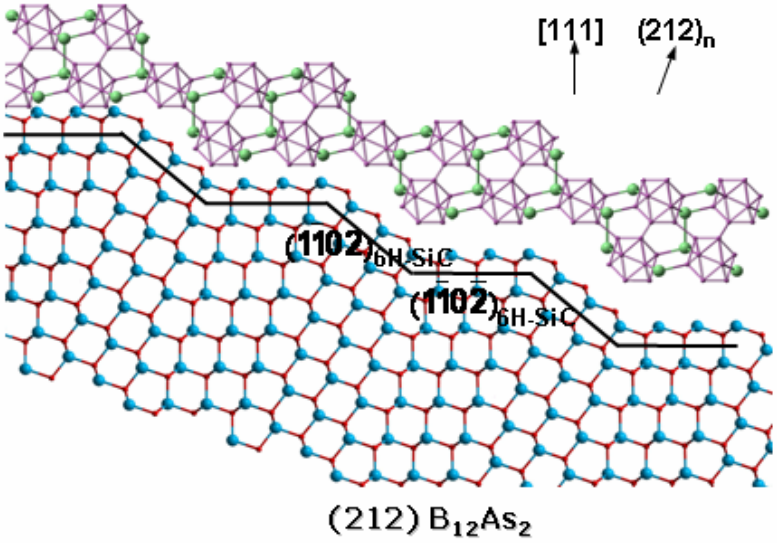

Fig. 43 [10-1] crystal visualization of (212) $B_{12}As_2$ on Si-face (1-10-2) closed packed facets on the m-plane 6H-SiC surface.

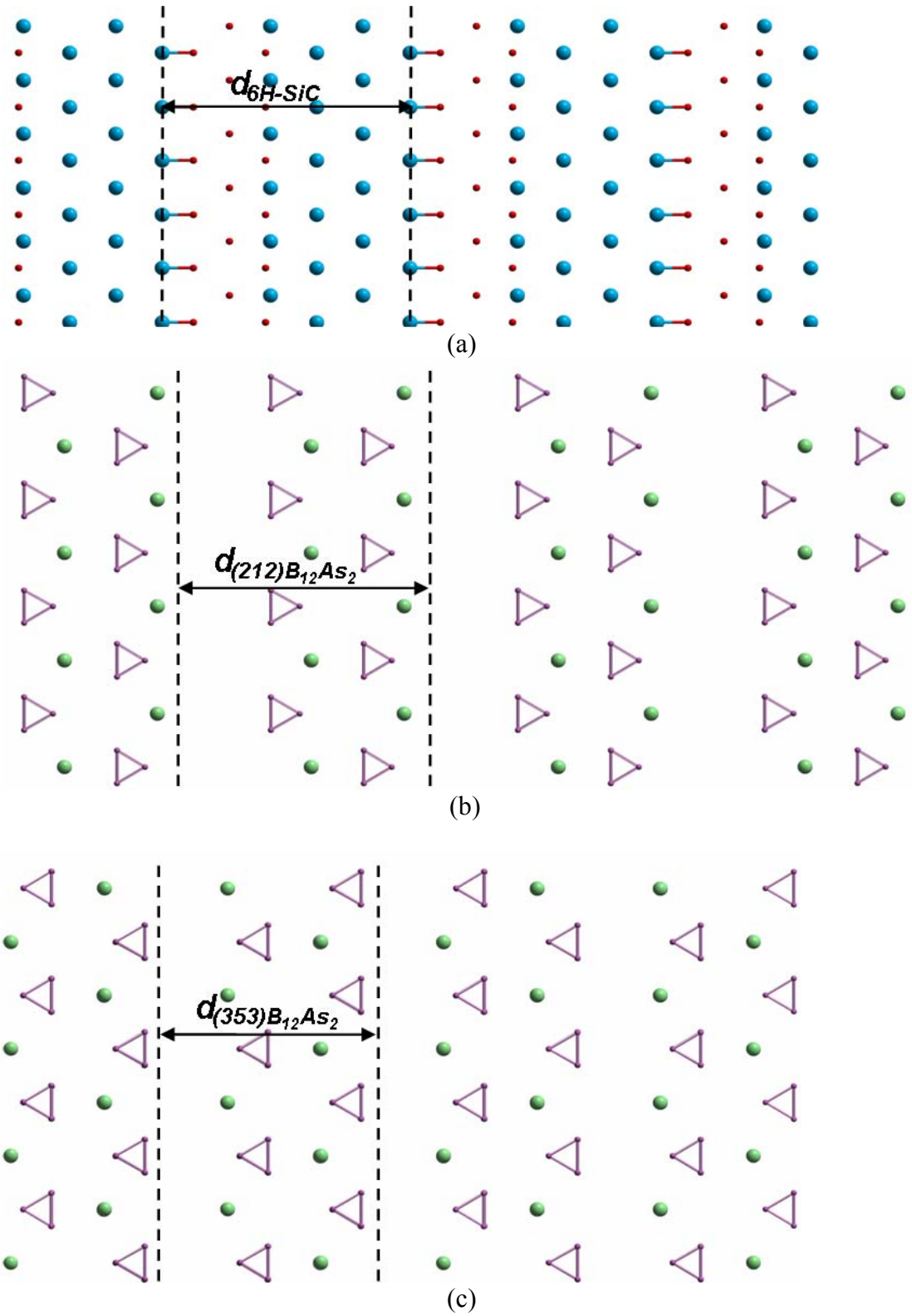

Fig. 44 $[111]_{B12As2}$ plan view of (a) m-plane 6H-SiC with Si-face (1-10-2) surface steps as nucleation terraces, (b) $(212)B_{12}As_2$ and (c) $(353)B_{12}As_2$, showing the significant difference between the lattice mismatch of (212) $B_{12}As_2$/15R-SiC and the one of (353) $B_{12}As_2$/15R-SiC.

Therefore, the growth orientation of $B_{12}As_2$ on 6H-SiC can be considered to result from the competition between the factors proposed above. For the growth of the (2-12) and (010) orientated $B_{12}As_2$ grains, minimizing in-plane lattice mismatch between the epilayer and the substrate acts as a dominant factor. On the other hand, the growth of (1-21) and (-12-1) orientated $B_{12}As_2$ grains preserves the expected epitaxial relationship and is promoted by the tendency to form low energy (1-21) surface facets. The sum of these factors appears to be enough to override the influence of reducing lattice mismatch between the epilayer and the substrate. Furthermore, the choice of (353) and its twin orientation, (212), arises from the nucleation on (1-102) and (1-10-2) closed packed facets on the hydrogen etched m-plane 6H-SiC substrate surface.

5.4. Conclusions

Microstructure of $B_{12}As_2$ epitaxial layers grown on m-plane 6H-SiC substrates has been examined. SEM shows the polycrystalline rough surface of the film. SWBXT and HRTEM reveals the existence of multiple domains, which include (1-21) $B_{12}As_2$, (2-12) $B_{12}As_2$, (353) $B_{12}As_2$ and their respective {111} twins, in the epilayer. The choice of the various growth orientations has been proposed to originate from the competition among the tendency for $B_{12}As_2$ to grow with a low energy surface orientation, the tendency to reduce the in-plane lattice mismatch between $B_{12}As_2$ planes oriented approximately parallel to the 6H-SiC (0001) planes to minimize local strain in the film/substrate interface and the tendency to nucleate on closed-packed atomic facets on the substrate surface.

6. $B_{12}As_2$ grown on m-plane 15R-SiC

6.1. Outline

Single crystal, heteroepitaxial growth of icosahedral $B_{12}As_2$ on m-plane 15R-SiC is demonstrated. In contrast to the polycrystalline and twinned epilayers produced on c-plane 6H-SiC and m-plane 6H-SiC, single crystalline and untwinned $B_{12}As_2$ was achieved on m-plane 15R-SiC. Synchrotron white beam X-ray topography, Raman spectroscopy and high resolution transmission electron microscopy confirm the high quality of the films. High quality growth is shown to be mediated by ordered nucleation of $B_{12}As_2$ on (474) substrate facets. This work demonstrates the $B_{12}As_2$ grown on m-plane 15R-SiC is free from structural variants and is of high single crystalline quality, which indicates m-plane 15R-SiC is a good substrate choice to grow high-quality untwinned $B_{12}As_2$ epilayers for future device applications.

6.2. Introduction

In the absence of native substrates, $B_{12}As_2$ has been heteroepitaxially grown on substrates with compatible structural parameters. To date, this has been attempted on substrates with higher symmetry than $B_{12}As_2$ such as Si and 6H-SiC. Unfortunately, growth of a lower symmetry epilayer on a higher symmetry substrate often produces structural variants, a phenomenon known as degenerate epitaxy. These variants are expected to have a detrimental effect on device performance, and have severely hindered progress of this material to date. An enumeration of these variants can be obtained by analysis of the 2D point groups of the substrate surface and the epilayer surface. For the case of $B_{12}As_2$ grown on Si with (100), (110) and (111) orientation and (0001) 6H-SiC, rotational and translational variants are both predicted and observed. The effect of degenerate epitaxy, however, can also be used to advantage by choosing substrates for which no variants are predicted. Single terrace, m-plane 15R-SiC fulfils this requirement for $B_{12}As_2$. As can be seen from Fig. 45, 6H-SiC exhibits a 3-3 symmetric stacking sequence while 15R-SiC displays a 3-2-3-2-3-2 asymmetric stacking sequence. If the closed packed atomic facets are exposed on m-plane 15R-SiC substrate surface, the symmetry of the surface steps which exists in m-plane 6H-SiC is not expected to be present in 15R-SiC. As large scale 15R-SiC substrates are presently not readily available, the same m-plane 6H-SiC substrate used in Chapter 5 is employed, which contained m-plane 15R-SiC inclusions of about 300-500 μm diameter.

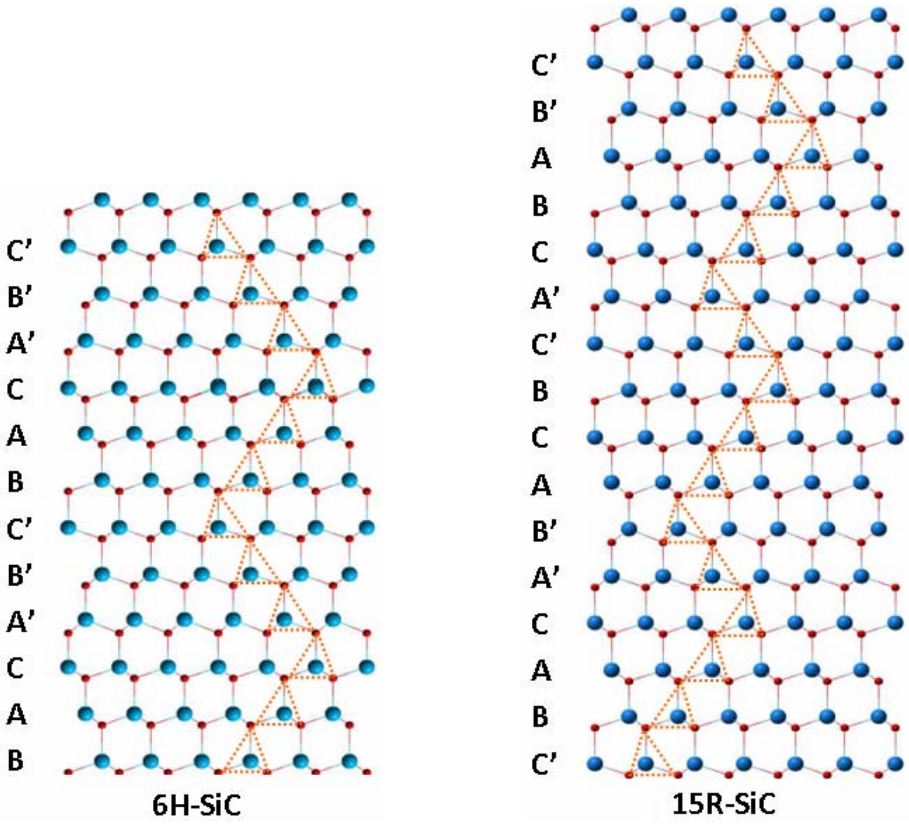

(a) (b)

Fig. 45 [11-20] projections showing the 3-3 symmetric stacking sequence in 6H-SiC ((a)) and 3-2-3-2-3-2 asymmetric stacking sequence in 15R-SiC ((b)).

6.3. Experimental

The m-plane 15R-SiC used for the $B_{12}As_2$ epitaxial growth are inclusions embedded in the m-plane 6H-SiC substrate used in Chapter 4, therefore the growth conditions are identical to the one on m-plane 6H-SiC, which include growth temperature of 1200°C, reactor pressure of 500 Torr, deposition time of 1 hour, 1% B_2H_6 in H_2 and 2% AsH_3 in H_2 as sources. The epitaxial $B_{12}As_2$ film also has a nominal thickness of 3 μm. The macroscopic epitaxial relationship was determined by SWBXT. Raman spectroscopy analysis of the films using a Renishaw InVia micro-Raman system with 488nm laser excitation provided information on the SiC polytype and the relative quality of the $B_{12}As_2$. The interfaces between the $B_{12}As_2$ and the SiC were examined by high-resolution transmission electron microscopy (HRTEM) using a 300keV JEOL 3000EX system at Brookhaven National Laboratory.

6.4. Results and discussion

Fig. 46 shows a transmission synchrotron X-ray Laue pattern from the $B_{12}As_2$ epitaxial layer grown on the m-plane 15R-SiC inclusion recorded with the epilayer as the x-ray exit surface. In contrast to the film grown on m-plane 6H-SiC, the $B_{12}As_2$ grown on the 15R-SiC region, produced much stronger and less streaked diffraction spots indicating

improved mosaicity. The corresponding diffraction spots are marked with three indices shown as 15R(*hkl*). The overall appearance of the $B_{12}As_2$ diffraction spots is consistent with a highly single crystalline and homogenous domain of (353) orientation. The Laue pattern of the epifilm also lacked any evidence for the existence of twins which would be manifested as (212) orientation $B_{12}As_2$. In addition, the degree of asterism in the $B_{12}As_2$ spots is much lower than observed from the film grown on m-plane 6H-SiC. The absence of twinning and the lower observed mosaicity constitutes a significant improvement over films grown under identical conditions on m-plane 6H-SiC, which has been discussed in Chapter 4. Raman spectra, as shown in Fig. 47, confirm this improvement with the Raman linewidth being narrower for the $B_{12}As_2$ film grown on 15R-SiC, and in particular Raman intensity is significantly stronger, despite both films having similar thickness. This illustrates that phonon properties and therefore also more macroscopic properties of the film are improved. Both Normaski optical observation (Fig. 48) and SEM observation (see Fig. 49) demonstrate a structure comprising only one type of equilateral triangular feature with a dimension of ~10μm, which suggests the film is single crystalline and agree with the result from SWBXT. Further microstructural information associated with the growth mechanism, was provided by HRTEM studies carried out on cross-sectional samples.

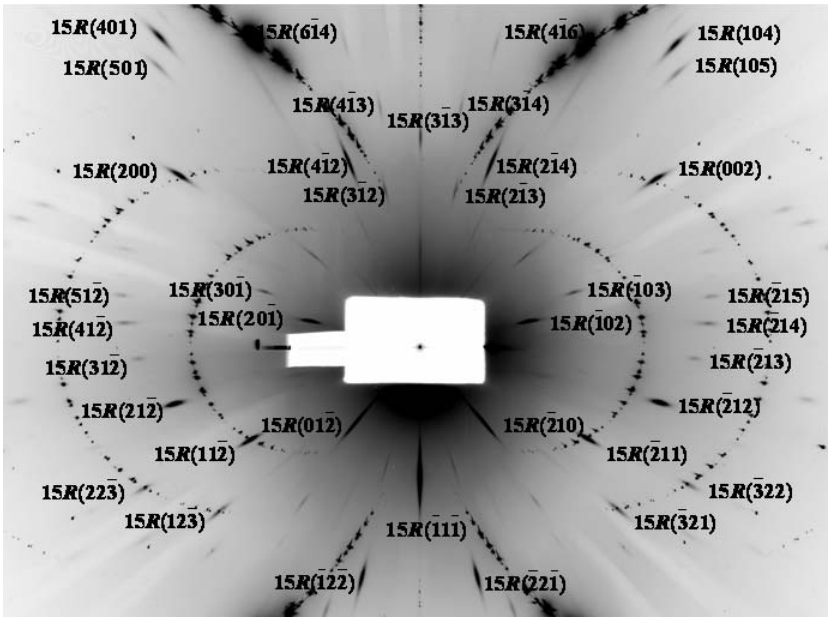

Fig. 46 Laue pattern of a $B_{12}As_2$ film grown on m-plane 15R-SiC showing (353) single growth orientation of the film.

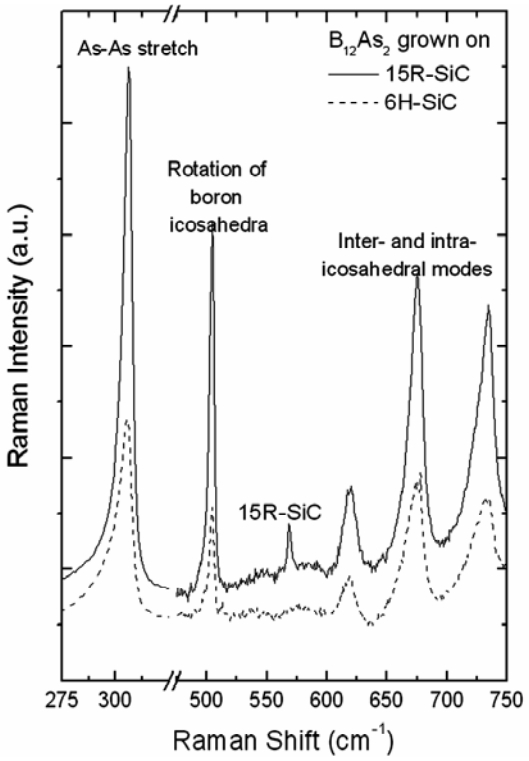

Fig. 47 Raman spectra recorded from $B_{12}As_2$ grown on m-plane 15R- and 6H-SiC. There are no 6H-SiC substrate modes in the spectral range shown, but one 15R-SiC mode.

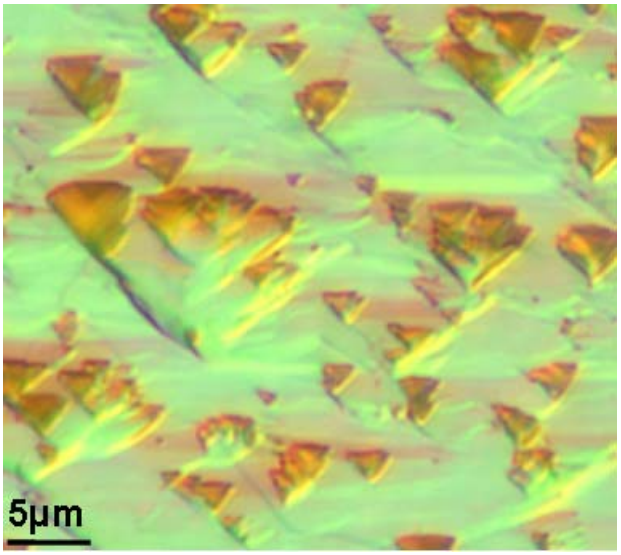

Fig. 48 Optical observation of a local area recorded from the film surface.

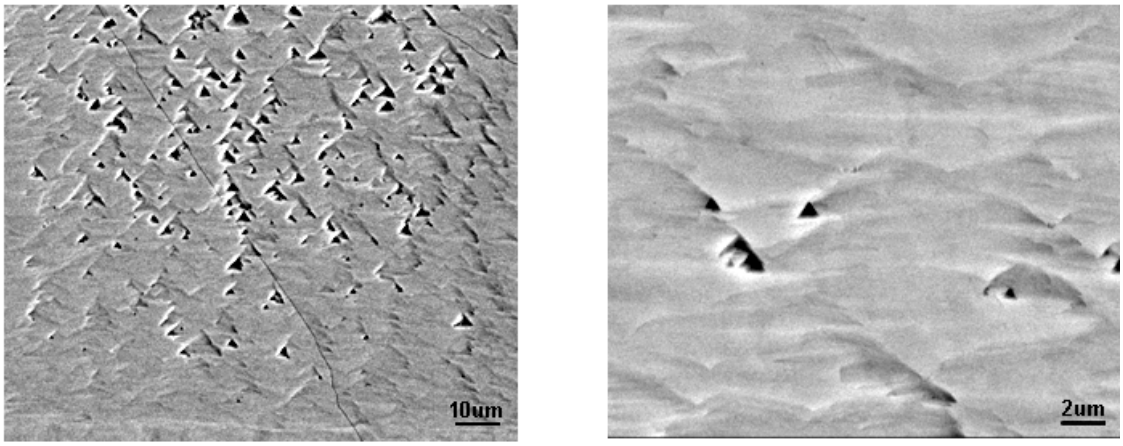

Fig. 49 SEM images showing one type of triangular defects on the surface of the epilayer grown on the 15R inclusion.

Excellent twin-free crystal quality was confirmed using HRTEM. Representative images in Fig. 50(a)&(b) show an abrupt, clean interface and no twins, in contrast to results from m-plane 6H-SiC, as discussed in Chapter 4. Structural correspondence was confirmed using multislice simulation[28] and the lattice orientation observed is consistent with (353) film orientation. A single m-plane terrace of the 15R-SiC substrate surface exhibits a 2D point group *m* (Fig. 51(a)), while that of the (353) $B_{12}As_2$ is also *m* (Fig. 51(b)), so that no structural variants are predicted in agreement with the observed absence of twins. However, the 15R-SiC substrate surface, hydrogen etched prior to growth, is expected to display a faceted structure featuring alternating close-packed (474) and (212) facets that are three and two bilayers wide, respectively, analogous to the behavior observed in m-plane 6H-SiC[29], and why $B_{12}As_2$ growth is single-crystalline and untwinned therefore needs further explanation.

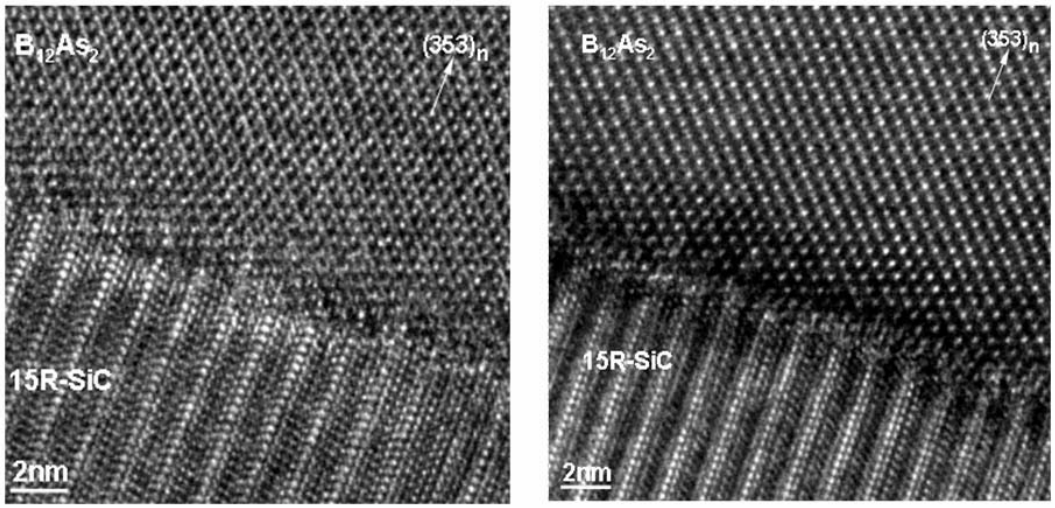

(a) (b)

Fig. 50 HRTEM images recorded from two local areas along the [$\mathbf{10\bar{1}}$] zone axis (parallel to [$\mathbf{11\bar{2}0}$] in the hexagonal system) showing a sharp $B_{12}As_2$/15R-SiC interface and the (353) surface orientation of $B_{12}As_2$.

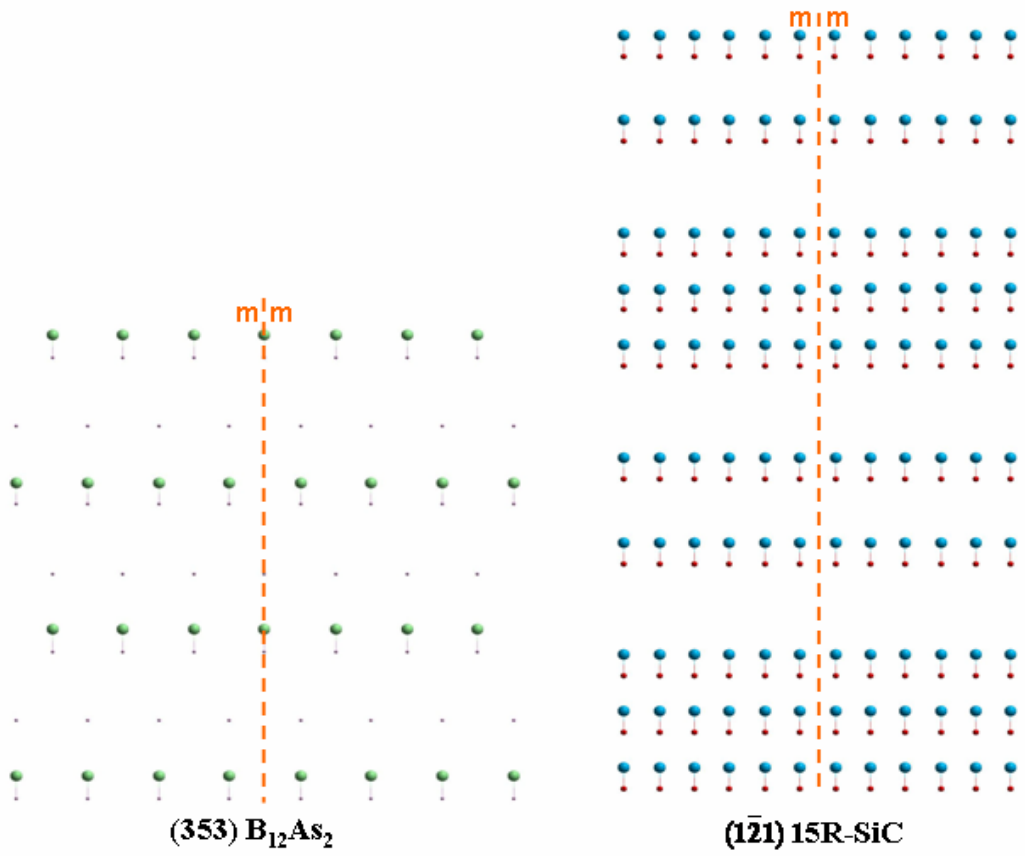

(a) (b)

Fig. 51 Projection of (a) (353) $B_{12}As_2$ surface showing *m* symmetry and (b) (1-21)15R-SiC surface also showing *m* symmetry.

Hydrogen etched m-plane 15R-SiC surface is expected to display an asymmetric close-packed facet structure exclusively composed of (474) and (212) facets that are successively 3-2-3-2-3-2 bilayers wide. The asymmetry in their widths would result in a ~3° offset from m-plane orientation (see Fig. 52, middle line). The periodic appearance of (11·8·11) facets would compensate for this asymmetry and produce an "on-axis" surface, as shown in Fig. 52 (upper line). This latter surface can be considered as quasi-vicinal with the (474) facets acting as terraces and the other facets as step risers. The stacking sequence below each (474) facet is identical such that the facets expose a series of equal thickness, lamellar nano-domains of 3C (cubic) structure leading to identical nucleation possibilities (Fig. 52). This therefore breaks the symmetry of the m-plane surface thus eliminating the associated advantage for $B_{12}As_2$ growth.

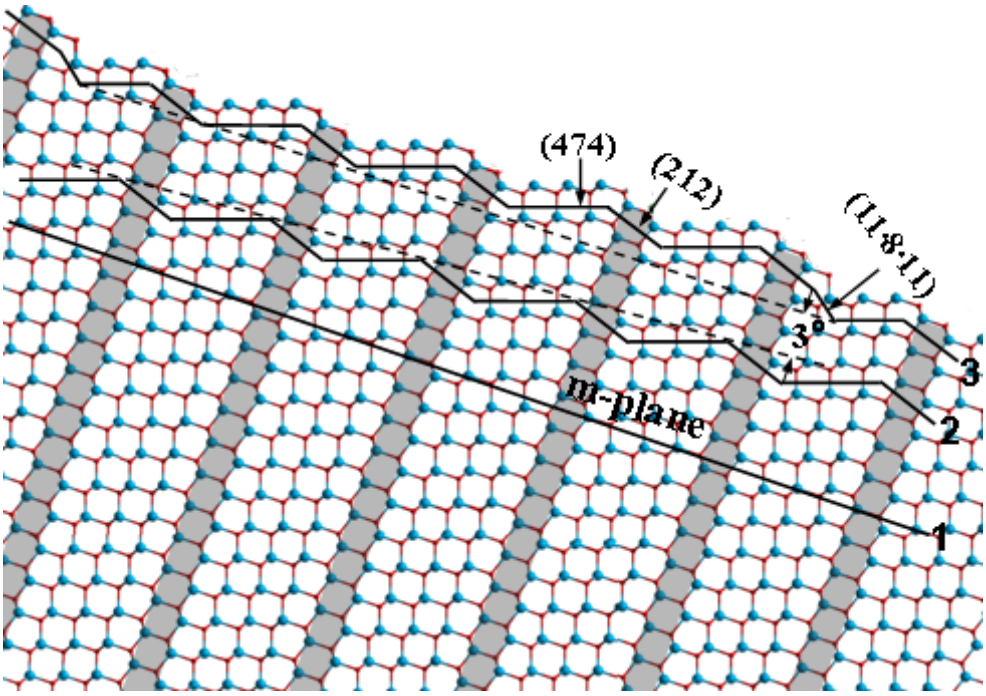

Fig. 52 Cross-sectional visualization along [$\mathbf{10\bar{1}}$] of the 15R-SiC structure. The uppermost black line indicates the on-axis, facet configuration comprising closed-packed (474) atomic terraces and coupled (212) and (11·8·11) step risers. The middle black line indicates the surface comprising only (474) and (212) facets which results in a 3° misorientation from m-plane and the lower line indicates the m-plane itself (unfaceted). Note the lamellar nano-domains of 3C-SiC structure bounded by the (474) facets and the shaded domain boundaries parallel to the (111) plane ((0001) in hexagonal system).

In order to understand why the $B_{12}As_2$ adopts a highly crystalline, untwinned configuration on this substrate, it is instructive to consider the details of the substrate and $B_{12}As_2$ structures and in particular the dangling bond configurations exhibited at the interface. Straightforward consideration of in-plane lattice mismatch reveals the significant difference between the lattice mismatch in (353) and (212) surface orientations. As shown in Fig. 53(a)-(c), the film/substrate mismatch (~1.8%) of untwinned configuration, (353) $B_{12}As_2$, is apparently much smaller than the one (~12.7%) of its twinned configuration, (212) $B_{12}As_2$, which would be too big for crystal growth and thus not favorable). that (353) oriented $B_{12}As_2$ is preferred for growth.

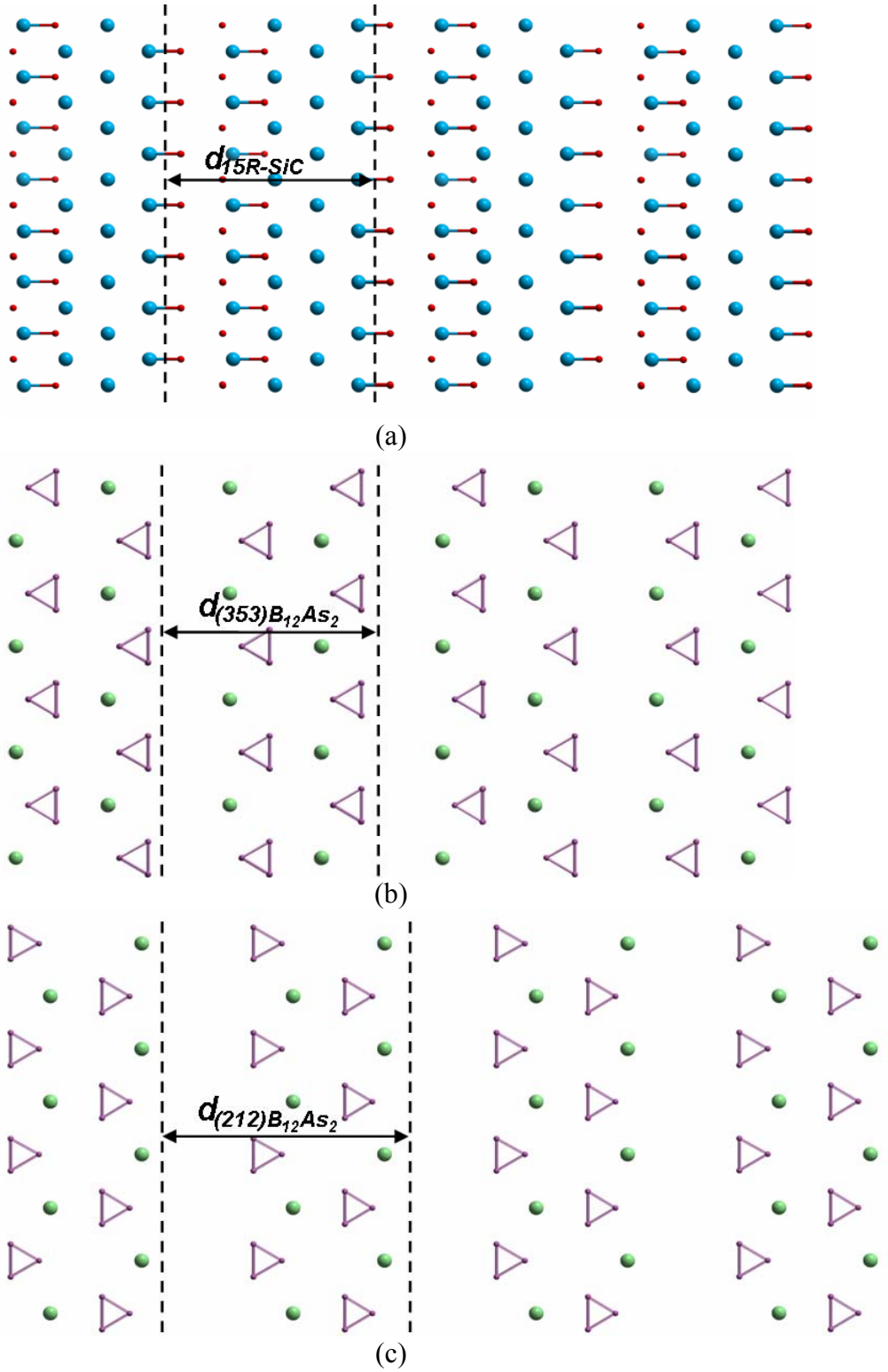

Fig. 53 Plan view of (a) top surface of m-plane 15R-SiC, (b) bottom surface of (353)$B_{12}As_2$ and (c) bottom surface of (212)$B_{12}As_2$, showing the significant difference between the lattice mismatch of (353) $B_{12}As_2$/15R-SiC and the one of (212) $B_{12}As_2$/15R-SiC.

On the other hand, considering lattice geometry, one can find that if the $B_{12}As_2$ nucleates on either the broader $(474)_{15R\text{-}SiC}$ or the narrower $(212)_{15R\text{-}SiC}$ facets with the $(111)_{B12As2}$ planes aligned to the facets, the film would adopt $(353)_{B12As2}$ orientation in agreement with observations although if nucleation occurs simultaneously on both types of facet the film would be polycrystalline. However, the large dimension of the in-plane repeat unit of the $(111)_{B12As2}$ (twice that of the close-packed SiC planes) requires that the facet width be large enough to accommodate nuclei of $B_{12}As_2$ which are at least two icosahedra wide (see Fig. 54(a)) so that preferential nucleation on the broader $(474)_{15R\text{-}SiC}$ facets is expected. Additional stabilization for nucleation on the $(474)_{15R\text{-}SiC}$ facets is provided by the fact that the $B_{12}As_2$ is able to simultaneously bond to the $(474)_{15R\text{-}SiC}$ terrace and the adjacent $(212)_{15R\text{-}SiC}$ step riser, as shown in Fig. 54(a) and (b). In contrast such stabilization is absent for $B_{12}As_2$ nuclei in twinned orientation thus preventing nucleation of twins (see also Fig. 54). Therefore, the choice of $(353)_{B12As2}$ orientation is dominated by the tendency to nucleate in $(111)_{B12As2}$ orientation on close-packed substrate facets of sufficient breadth.

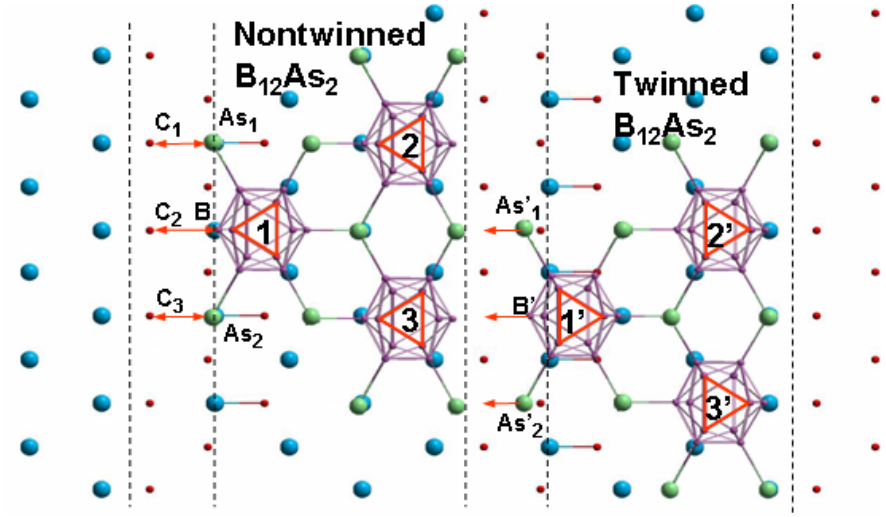

(a)

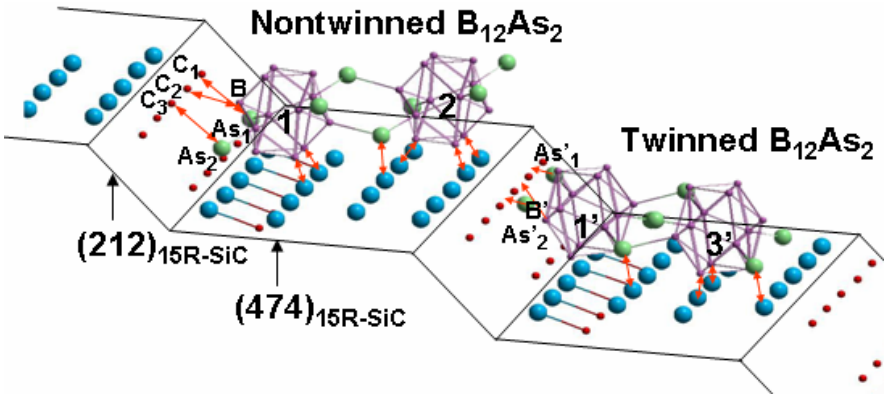

(b)

Fig. 54 Plan view ((a)) and 3-D perspective view ((b)) of nontwinned and twinned (353) $B_{12}As_2$ nucleated on m-plane 15R-SiC surface facets. For the non-twinned $B_{12}As_2$, the triangular configuration of B atoms at the bottoms of icosahedra 1, 2 and 3 bond to the

similarly oriented triangular configurations of Si atoms exposed on the $(474)_{15R\text{-}SiC}$ terrace (see (a) and (b)). In addition, atoms As_1, B, and As_2 can be well bonded to atoms C_1, C_2, and C_3, respectively, on the neighboring $(212)_{15R\text{-}SiC}$ step riser. In contrast, while the triangular configuration of B atoms at the bottoms of icosahedra 1', 2' and 3' can similarly bond to the $(474)_{15R\text{-}SiC}$ terrace, atoms As'_1, B', As'_2 are not able to reasonably bond to the corresponding C atoms on the neighboring $(212)_{15R\text{-}SiC}$ step riser.

Growth then proceeds via step flow whereby the $B_{12}As_2$ layer nucleated on one facet overgrows that nucleated on the facet below. This is possible since the spacing of the $(111)_{B12As2}$ planes is within 15% of the height difference between adjacent $(474)_{15R\text{-}SiC}$ facets. Help in accommodating this 15% out-of-plane disregistry between film and substrate is provided by the periodic presence of the deeper step riser comprising the coupled $(212)_{15R\text{-}SiC}$ and $(11{\cdot}8{\cdot}11)_{15R\text{-}SiC}$ facets. In addition, the in-plane lattice mismatch (~1.8%) can be well accommodated by the periodic appearance of interfacial dislocations (with one extra (555) half-plane on the SiC side, see Fig. 55(a) and its example Fig. 55(b)). Thus both in-plane and out-of-plane mismatch is accommodated. For $B_{12}As_2$ monolayer nucleated on adjacent $(474)_{15R\text{-}SiC}$ terraces, there is a small mutual sideways disregistry along the terrace. As shown in Fig. 56(a), on each of the terraces which are separated by the dotted lines, $B_{12}As_2$ monolayer can be represented by the boron triangular configurations which constitute the bottom ends of each boron icosahedron. Adopting the approach in Chapter 3.4.4., $B_{12}As_2$ is considered as an (0001) layered structure comprising the *ABC* stacking sequence which has been depicted in Fig. 17(a). If the monolayer on the most left terrace is accommodated at A_1 sites (Fig. 56(a)), the ones on the right neighboring lower terraces are accommodated at C_2, B_3 and A_4 sites respectively. For each individual atomic terrace, when growth proceeds to next upper $B_{12}As_2$ layer which overgrows the one nucleated on the atomic facet below, the corresponding stacking sequence is expected to be the A_2 (for C_2), C_3 (for B_3) and B_4 (for A_4) respectively. Comparing the relative positions of A_1 and A_2, C_2 and C_3, B_3 and B_4, one can find there is a small shift, $1/4[10\text{-}1]_{B12As2}$ (equivalent to $1/12[11\text{-}20]_{B12As2}$ in the hexagonal system) or $1/4[\text{-}101]_{B12As2}$, between each pair of the stacking positions (Fig. 56(b)). This is thought small enough so that it can be accommodated elastically. For example, perfect registry will be attained if successive layers displace in opposite directions by $1/8[10\text{-}1]_{B12As2}$. Partial nucleation on the narrower $(474)_{15R\text{-}SiC}$ facet just below the deeper step riser is expected to facilitate the overgrowth process between nuclei originating on the two broader $(474)_{15R\text{-}SiC}$ facets just above and below this narrower $(474)_{15R\text{-}SiC}$ facet. In this way, the $B_{12}As_2$ is able to quickly self-adjust its structure near the film/substrate interface while maintaining good bonding with the substrate allowing it to subsequently grow with nearly perfect structure (Fig. 55(b)).

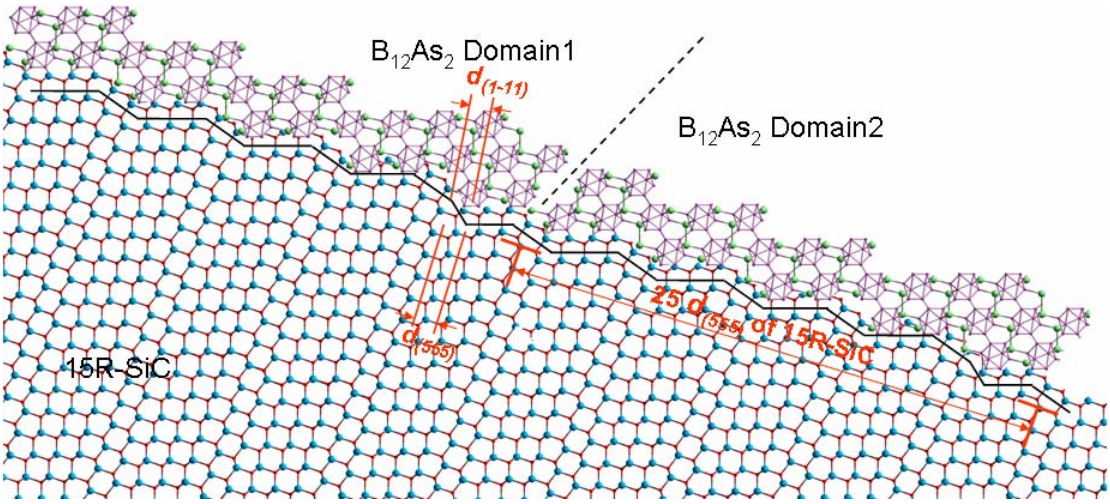

(a)

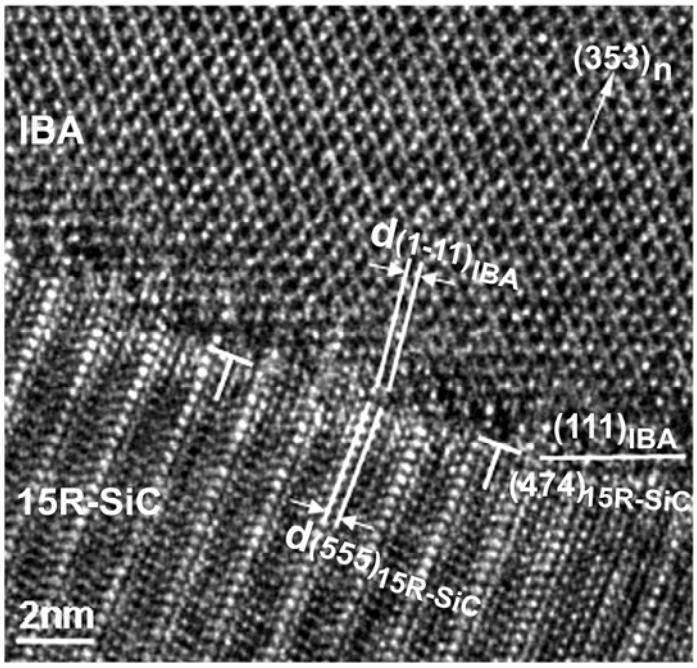

(b)

Fig. 55 (a) Cross-sectional crystal visualization of $B_{12}As_2$ grown on (474) facets with coupled (212) and (11·8·11) step risers expected on m-plane 15R-SiC surface, where the blue lines represent the extra half planes existing in the SiC; (b) HRTEM observation along $[\mathbf{10\bar{1}}]$ showing the presence of extra half planes in SiC. The symbol ⊥ marks the location of interfacial dislocations with extra half-planes in the 15R-SiC substrate.

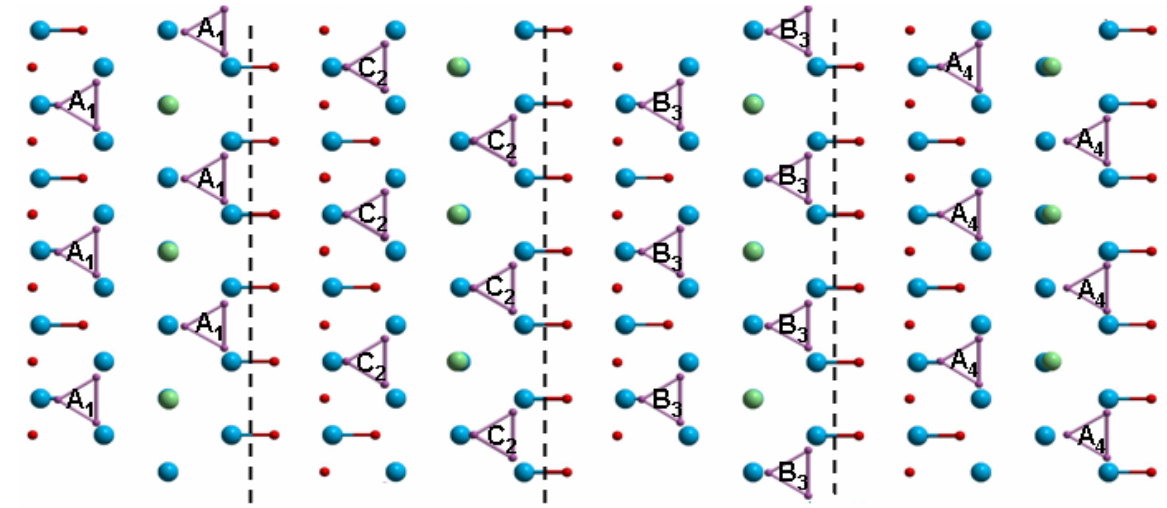

(a)

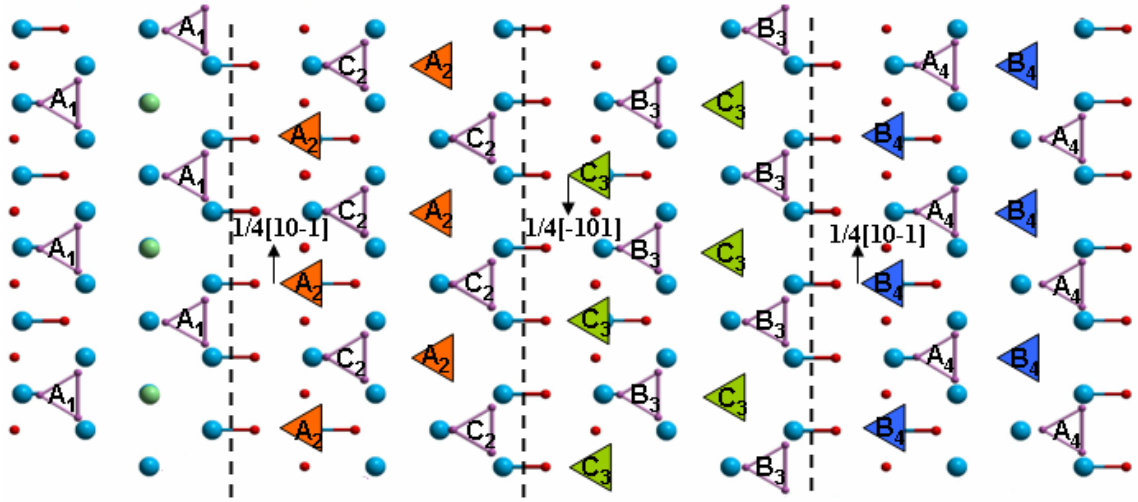

(b)

Fig. 56 (a) Plan view of the projections of $B_{12}As_2$ monolayer, represented by boron triangular configurations with *ABC* stacking sequence, nucleated on (474) terraces on the m-plane 15R-SiC substrate surface; (b) Plan view of the projections of $B_{12}As_2$ with an additional layer overgrowing on the one nucleated on the substrate facet below. The triangles highlighted in orange marked by A_2, represents the stacking sequence of the layer grown on C_2. The triangles highlighted in green marked by C_3, represents the stacking sequence of the layer grown on B_3. The triangles highlighted in orange marked by B_4, represents the stacking sequence of the layer grown on A_4.

6.5. Conclusion

Epitaxial growth of single crystalline $B_{12}As_2$ has been achieved on m-plane 15R-SiC inclusions embedded in a 6H-SiC substrate wafer. SWBXT and cross-sectional HRTEM revealed untwinned (353) orientated $B_{12}As_2$, with significantly improved macroscopic properties as probed optically. It was found that the choice of film orientation substantially resulted from the tendency to nucleate in $(111)_{B12As2}$ orientation on $(474)_{15R\text{-}SiC}$ close-packed

facets that are exposed on the m-plane 15R-SiC surface. A model illustrating stable bonding configuration across the film/substrate interface has been constructed and proposed to further favor the formation of (353) orientated $B_{12}As_2$. Therefore, m-plane 15R-SiC could be an excellent substrate to grow high quality single crystalline $B_{12}As_2$ film for future device application.

7. Conclusions

Defect structures and growth mechanisms of $B_{12}As_2$ epilayers grown on on-axis c-plane 6H-SiC, 3.5° off-axis c-plane 6H-SiC, m-plane 6H-SiC and 15R-SiC have been studied using SWBXT, SEM, HRTEM and CaRine 4.0 software.

I) For the growth on on-axis c-plane 6H-SiC, the epitaxial relation between film and substrate is identified as $(0001)_{B12As2}<1\bar{1}\bar{2}0>_{B12As2}||(0001)_{6H\text{-}SiC}<1\bar{1}\bar{2}0>_{6H\text{-}SiC}$. The $B_{12}As_2$ epilayer is twinned and the twin relationship consisted of a 180° (or equivalently 60°) rotation about $[0001]_{B12As2}$. The disordered mosaic transition layer is found to be a result from the competition among eight possible types of translationally and rotationally variant domains available on the substrate surface. Boundaries between translationally variant domains are shown to have unfavorable high-energy bonding configurations while the formation of a $1/3[0001]_{B12As2}$ Frank partial dislocation enabled elimination of these high energy boundaries during mutual overgrowth. (0003) twin boundaries in the regions beyond 200nm are shown to possess fault vectors such as $1/6[1\bar{1}00]_{B12As2}$ which are shown to originate from the mutual shift between the nucleation sites of the respective domains.

II) For the growth on 3.5° off-axis c-plane 6H-SiC, the epitaxial relation between film and substrate is also determined to be $(0001)_{B12As2}<1\bar{1}\bar{2}0>_{B12As2}||(0001)_{6H\text{-}SiC}<1\bar{1}\bar{2}0>_{6H\text{-}SiC}$. The epilayer contains $B_{12}As_2$ twin domains related by a 180° (or equivalently 60°) rotation in (0001) plane. Stable low energy (0003) twin boundaries and high energy lateral twin boundaries are also observed in the epilayer. The film quality is not substantially improved due to the eight possible types of translationally and rotationally variant domains still available on the slightly off-cut substrate surface.

III) For the growth on m-plane 6H-SiC, multiple grains are found to be present in the epilayer, which include (1-21) $B_{12}As_2$, (2-12) $B_{12}As_2$, (353) $B_{12}As_2$ and their respective twins. The choice of (1-21) $B_{12}As_2$ and its twin results from the tendency for $B_{12}As_2$ to grow with a low energy surface orientation. (2-12) surface orientation and its twinned orientation is suggested to be controlled by the tendency to reduce the in-plane lattice mismatch between $B_{12}As_2$ and SiC (0001). In contrast, the tendency to nucleate on closed-packed atomic facets on the substrate surface is dominate for the formation of (353) $B_{12}As_2$ and its twin.

IV) For the growth on m-plane 15R-SiC, single crystalline and untwined (353) orientated $B_{12}As_2$ film is obtained. The choice of film orientation results from the tendency to nucleate in $(111)_{B12As2}$ orientation on $(474)_{15R\text{-}SiC}$ close-packed facets exposed on m-plane 15R-SiC substrate surface. This indicates m-plane 15R-SiC could be a potentially excellent substrate to grow high quality $B_{12}As_2$ single crystalline film for future device fabrication.

8. Future work

We have shown the defect analysis and growth mechanisms of $B_{12}As_2$ grown on various types of SiC substrates, e.g., there are eight possible distinct nucleation sites on on-axis c-plane 6H-SiC substrate surface, which result in the various unavoidable structural variants in the epilayer. However, the effect of growth temperature on these growth mechanisms and the film quality, e.g., how the defect density in the film varies under different growth temperatures, hasn't been studied. Therefore, it is important to study how the temperature impacts the epitaxial growth.

In Chapter 4, it has been shown that 3.5° offcut angle on the c-plane 6H-SiC substrate surface does not have significant effect in reducing the number of possible structural variants in the film in that the width of each single step on the substrate surface is still large enough to accommodate the eight nonequivalent nucleation sites for to $B_{12}As_2$ grow. A larger offcut angle, i.e., 7°, which can further narrow the terrace width of each step on the substrate surface, may contribute to alleviating the problem of structural variants by limiting the number of possible nucleation sites on the substrate surface. In consequence, it is of great importance to study the effect of a larger offcut angle on the epitaxial growth of $B_{12}As_2$.

In Chapter 6, single crystal growth of $B_{12}As_2$ has been shown to achieve on small m-plane 15R-SiC inclusions embedded in m-plane 6H-SiC. However, since such growth occurred in small areas of about 300-500 μm diameter, it remains uncertain that if the single crystal growth can be also achieved on much larger area, i.e., 2cm x 2cm, for device fabrication. Thus it is vital to seek available m-plane 15R-SiC substrates with large area and study the corresponding $B_{12}As_2$ epitaxial growth on them.

$B_{12}As_2$ has been proposed to be potentially useful for the application of high temperature semiconductor devices and space electronics. It will be instructive to fabricate $B_{12}As_2$ devices so as to study the device performance and their behavior under electron irradiation.

References

[1] W. J. Choyke, H. Matsunami and G. Pensl editors, Silicon Carbide (Springer, 20004)
[2] O. Ambacher, J. Phy. D. Appl. Phys., **31**, 2653 (1998)
[3] D. C. Look, Mater. Sci. Eng. B **80**, 383 (2001)
[4] D. Emin, Physics Today, **January**, 55 (1987)
[5] G. A. Slack, D. W. Oliver and F. H. Horn, Phys. Rev. B, **4**, 1714, (1971)
[6] Ordered Boron Arsenide, P. D. Ownby, Journal of the American Ceramic Society, **58**, 7-8, 359 (1975)
[7] J. R. Michael, T. L. Aselage, D. Emin and P.G. Kotula, J. Mater. Res., **20** (11), 3004 (2005)
[8] D. Emin, J. Sol. Sta. Chem., **179**, 2791 (2006)
[9] D. Emin and T. L. Aselage, J. App. Phys., **97**, 013529 (2005)
[10] D. Emin, J. Sol. Sta. Chem., **177**, 1619 (2004)
[11] M. Carrard, D. Emin and L. Zuppiroli, Phys. Rev. B, **51**(17), 11270 (1995)
[12] R.H. Wang, D. Zubia, T. O'Neil, D. Emin, T. Aselage, W. Zhang and S.D. Hersee, J. Electronic Materials, **29** (11), 1304 (2000)
[13] W.M. Vetter, R. Nagarajan, J. H. Edgar and M. Dudley, Mater. Lett., **58**, 1331 (2004)
[14] T.L. Aselage, D. Emin, US Patent No. 6,479,919, (2001)
[15] P. Rappaort, J. J. Loferski and E. G. Linder, RCA Rev., **17**, 100 (1956)
[16] D. Emin and T. L. Aselage, J. Appl. Phys. **97**, 013529 (2005)
[17] M. Dresselhaus, G. Chen, M. Y. Tang, R. Yang, H. Lee, D. Yang, Z. Ren, J. Fleurial, and P. Gogna, Int. Mater. Rev., **48**, 45 (2005)
[18] X. Zhou, J. H. Edgar and S. Speakman, J. Crystal Growth, **293**, 162 (2006)
[19] R. Nagarajan, Z. Xu, J. H. Edgar, F. Baig, J. Chaudhuri, Z. Rek, E. A. Payzant, H. M. Meyer, J. Pomeroy and M. Kuball, J. Crystal Growth., **273**, 431 (2005)
[20] M. Dudley and X. Huang, Materials Science Forum 338, 431, 1998.
[21] X. R. Huang, M. Dudley, W. M. Vetter, et al., J. App. Crys., **32**, 516 (1999)
[22] M. Dudley, X. R. Huang and W. Huang, J. Phys. D: App. Phys., **32**, A139 (1999)
[23] X. R. Huang, M. Dudley, J. Y. Zhao, Philosophical Transactions of the Royal Society of London. A, 357, 2659, (1999)
[24] J. M. Cowley and A. F. Moodie, Acta Cryst., **10**, 609 (1957)
[25] C. P. Flynn and J. A. Eades, Thin Soild Films, **389**, 116 (2001)
[26] S.W. Chan, J. Phys. Chem. Solids, **55**, 1137 (1994)
[27] N.W. Johnson, Canadian J. Mathematics, **18**, 169 (1966)
[28] H. Chen, G. Wang, M. Dudley, L. Zhang, L. Wu, Y. Zhu, Z. Xu, J.H. Edgar and M. Kuball, J. Appl. Phys., **103 (12)**, (2008)
[29] J. Takahashi, N. Ohtani, M. Katsuno, and S. Shinoyama, J. Crystal Growth., **181**, 229 (1997)

Appendix I Studies on the correlation between defects and electrical properties of 4H-SiC Schottky diodes

Outline

An 8° off-axis 4H-SiC wafer with circular Schottky contacts fabricated on a CVD grown 4H-SiC homoepitaxial layer was studied to investigate the influence of various defects, including small (closed-core) screw dislocations (Burgers vector of 1*c* or 2*c*), hollow-core (micropipes; Burgers vector larger than 2*c*), threading edge dislocations (from conversion of basal plane dislocations from the substrate into the epilayer), grain boundaries and triangular defects, on the device performance in the form of breakdown voltages. The defects were examined using synchrotron white beam x-ray topography (SWBXT) based techniques and molten KOH etching. The devices commonly contained basal plane dislocations, small screw dislocations and threading edge dislocations, the latter two of which could give rise to low breakdown voltages for the devices. In addition, less commonly observed defects such as micropipes, grain boundaries and triangular defects are much more destructive to device performance than closed-core screw dislocations and threading edge dislocations.

Introduction

In last few decades, silicon carbide (SiC) has become a prominent material for various applications, such as high temperature, high-power electronics and radiation-hard electronic technologie. SiC technology has advanced rapidly with steady improvements in quality and size. Despite these achievements, several factors currently limit the overall crystalline quality of SiC and as a consequence the device performance. In particular, defects in SiC crystals are considered to be a major roadblock to further development. As it is widely recognized that defects in SiC degrade device performance, it would be useful to characterize the effect each defect type has on the device properties. SWBXT is a powerful tool which has high strain sensitivity and provides suitable spatial resolution to image dislocations in crystals. Molten KOH etching has also been proven to be a fast and convenient method to reveal dislocations in SiC, especially screw dislocations (both 1*c*/2*c* and micropipes) and threading edge dislocations. To this end, a combination of SWBXT and KOH etching has been applied to investigate the influence of different defects, including dislocations, grain boundaries and triangular defects, on Schottky devices fabricated on 4H-SiC homoepitaxial layers deposited on an 8° off-axis 4H-SiC wafer. These defect types were examined using a correlation between grazing incidence and back reflection SWBXT, KOH etching and electrical measurements. Back reflection geometry was adopted to map the distribution of screw dislocations. In order to distinguish dislocations in the epilayer from those in the substrate, grazing incidence geometry was employed to record dislocation information exclusively from the epilayer.

Experimental details

The 10μm-thick and lightly doped 4H-SiC epilayer (N_D=5x10^{15} cm^{-3}) was grown on an n^+ 4H-SiC substrate (N_D=8x10^{18} cm^{-3}) with 8^o off-cut from [0001] toward the [11-20] direction. Unterminated circular Schottky contacts were formed by evaporation of 500 Å Ni/3000 Å Au

through a shadow mask on the wafer, with diameters from 200 to 1000 µm. The breakdown measurements were performed using a Keithley model 237 source-measure unit. The breakdown voltage is defined as the voltage yielding a current density of 0.1 A/cm^2. The metallization was chemically removed on both sides of the sample after breakdown measurements to reduce noise in the SWBXT images. The back side of the wafer was then chemically-mechanically polished to reduce strain. The molten KOH etching was carried out at 500 ^{o}C for 5 minutes.

After KOH etching, SWBXT experiments were carried out at the Stony Brook Topography Facility (Beamline X-19C) at the National Synchrotron Light Source, at Brookhaven National Laboratory. The x-ray beam had a wavelength spectrum ranging from 0.1 to 2.00 Å, with peak intensity at around 0.8 Å. The specimen-film distances were set to be 10-25 cm depending on background noise and desired diffraction patterns. The optical Nomarski microscopy was performed on a Nikon Ellipse E600 JSL Optical Microscope.

Discussion

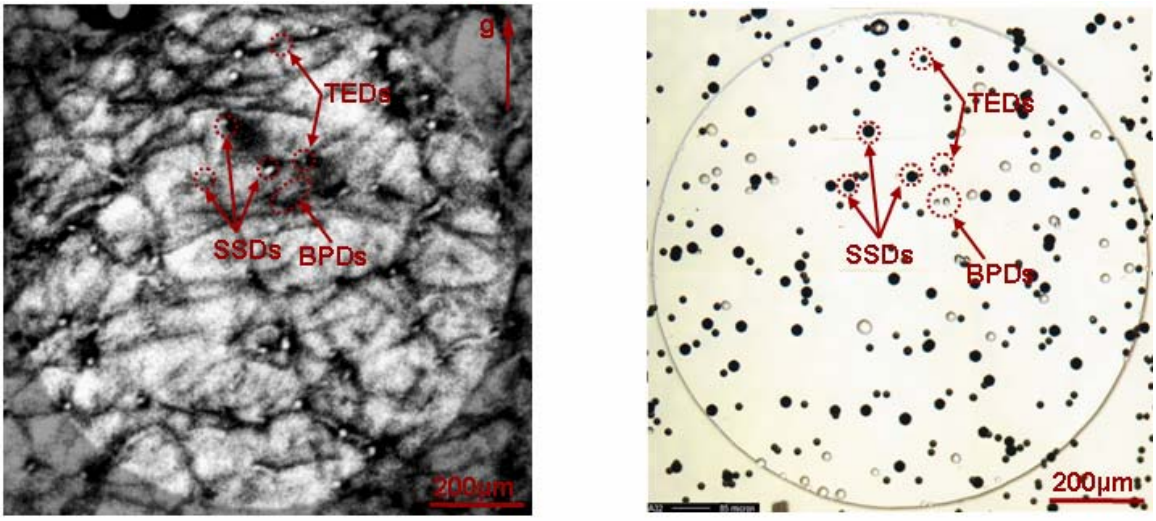

(a) **(b)**

Fig. 57. (a) Grazing incidence x-ray topograph of defect structure in a typical circular device with g=$11\bar{2}8$; (b) Nomarski optical micrograph of the same device as (a) after molten KOH etching.

Small screw dislocations (SSDs), threading edge dislocations (TEDs) and basal plane dislocations (BPDs) are the major defects present in all the studied devices. Figures 1(a) and (b) show a one-to-one correspondence between defects and their related etch pits in a typical circular Schottky device. As shown in the x-ray topograph [Fig. 52(a)], SSDs and TEDs exhibit white circular contrast with diameters of more than ten microns and a few microns, respectively, and BPDs appear as dark lines. In Fig. 52(b), the SSD-related etch pits appear as large black hexagons, TED-related etch pits appear as smaller black hexagons and BPD-related etch pits appear as white seashell shapes. The SSDs propagate from the substrate into the epilayer in a nearly perpendicular direction to the surface and are thus readily revealed by KOH etching. This conclusion has been confirmed by correlation of the SWBXT and KOH etching results. In contrast, BPDs can propagate from the substrate into the epilayer in two different ways. Some remain in the basal plane and directly propagate into the epilayer while

others are converted into TEDs in the epilayer due to image forces. The TEDs thread almost normal to the epilayer surface and are again be as readily etched as SSDs by molten KOH.

Apart from the three commonly occurring defects discussed above, micropipes (MPs), grain boundaries (GBs) and triangle-shaped defects (TDs) exist in a few devices. Figures 53 and 54 illustrate a device that contains a MP, a GB and a TD. Micropipes are open-core screw dislocations having Burgers vectors larger than 2*c* in 4H-SiC crystals. This causes their strain fields to be correspondingly larger than those of SSDs. Therefore, their etch pits are relatively large and they appear as white contrast features that are larger than SSDs in Figs. 54(a) and (b). The GBs can be formed by a row of BPDs or TEDs, which have Burgers vectors in the basal plane. For $\mathbf{g} = 000 \cdot 16$, $\mathbf{g} \cdot \mathbf{b} = 0$ and $\mathbf{g} \cdot \mathbf{b} \times \mathbf{l} = 0$ for threading edge dislocations, so such dislocations should be invisible in this reflection. This condition is consistent with the threading edge boundary being visible in Fig. 54(b) and invisible in Fig. 54(a). The TDs in this sample are found to have a base which intersects the sample surface and is perpendicular to the off-cut direction. Okada *et al.* observed that at the base of the triangular defect, there was a stacking fault (SF) bounded by two partial dislocations. One perfect dislocation oriented in a $[1\bar{1}20]$ direction dissociated into the two partial dislocations to form the base of the 3C-polytype inclusion and the associated stacking fault. Zhou *et al.* suggested that TDs were linked to a 4H to 3C polytype phase transformation initiated by stacking faults that intersect a vertical step ledge during epitaxial growth. The replication of their partial dislocation ledge intersections can give rise to the formation of 3C platelets.

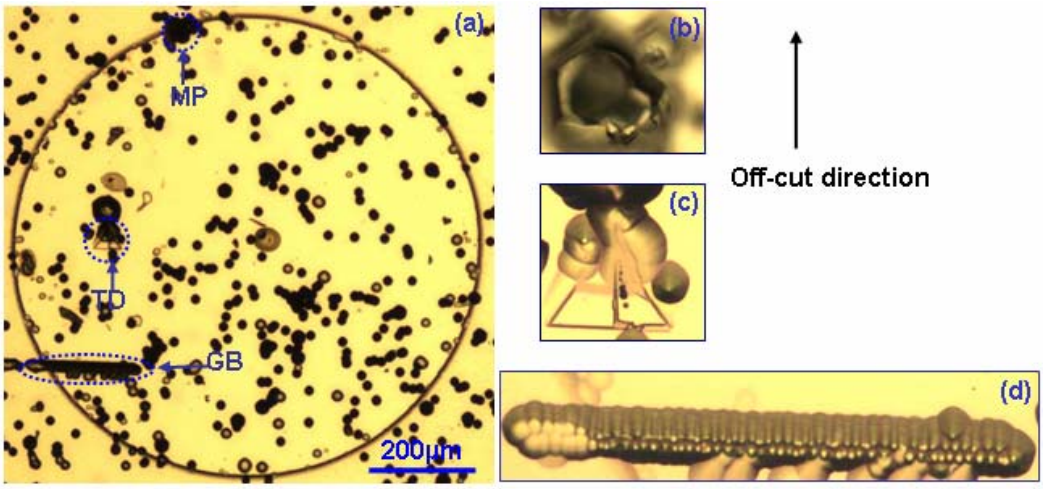

Fig. 58. Optical micrograph of defect structure in a device after KOH etching. (a) Overview of the device; (b) Enlargement of the MP etch pit in (a); (c) Enlargement of the TD etch pit in (a); (d) Enlargement of the GB etch pit in (a).

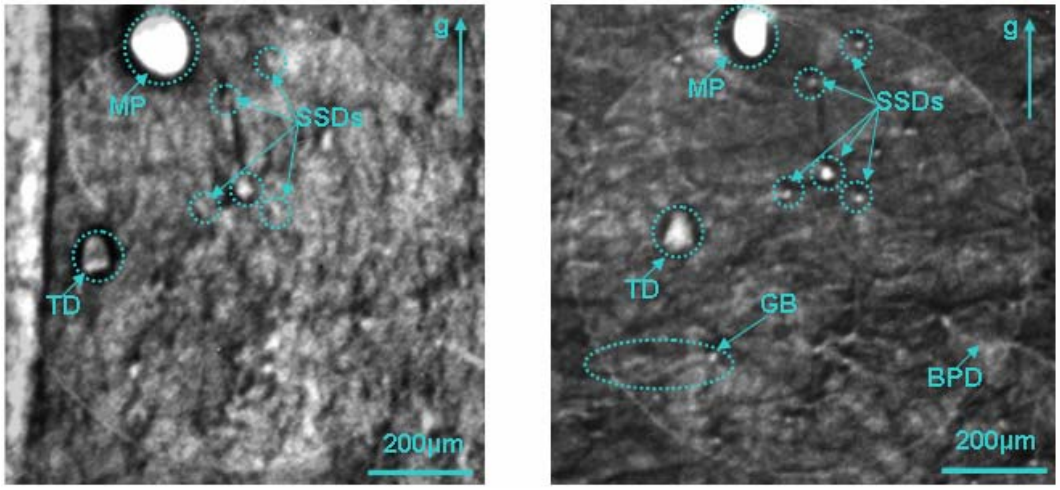

(a) **(b)**

Fig. 59. X-ray topographs of structural defects in the same device as Fig.2. (a) Back reflection topograph with $g=000\bullet16$; (b) Grazing incidence topograph with $g=11\bar{2}8$.

The density of each defect type (except for BPDs) was determined from the results of SWBXT and KOH etching to examine the influence of each defect type on the breakdown behavior of the devices. Since every device has SSDs and TEDs, in order to better study their effects on the electrical properties, the devices containing only those two types of defect were chosen. Fig.55 shows the relationship between the numbers of SSDs and the breakdown voltage in devices of five different sizes. For each device size, the breakdown voltages tend to decrease as the densities of SSDs increase. Therefore, high densities of SSDs can lead to low breakdown voltages, in agreement with the results from Wahab's group. It can also be seen from Fig. 56 that as the number of TED goes up, the breakdown voltage is reduced. The breakdown voltages in these devices are certainly limited by the lack of edge termination, but the low values seen in certain specific devices are likely due to defects rather than to edge effects, which should not change much from device to device.

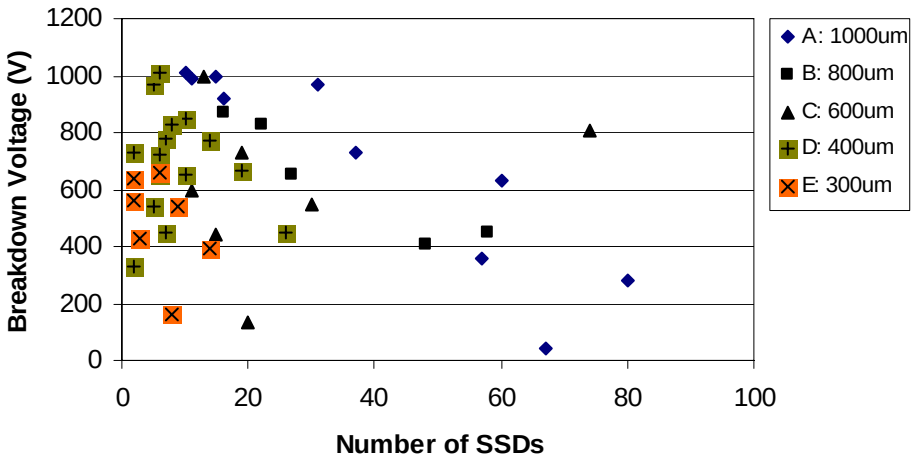

Fig. 60. Correlation between numbers of SSDs and breakdown voltages for different device sizes

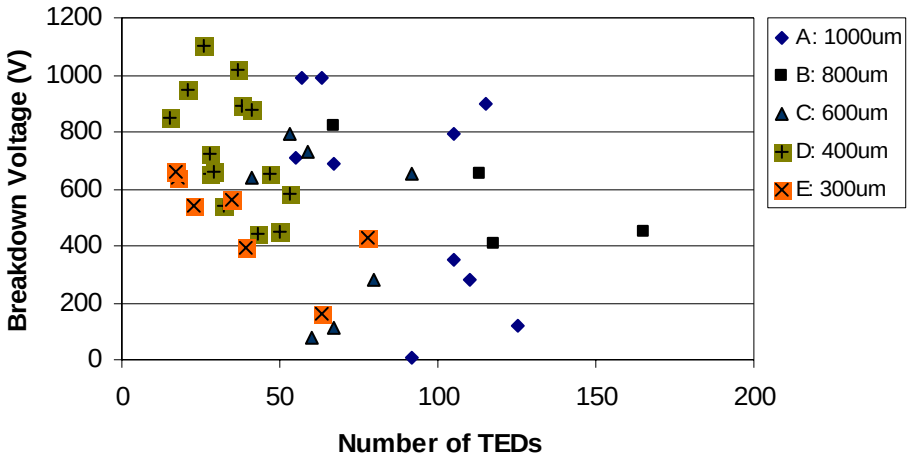

Fig. 61. Correlation between numbers of TEDs and breakdown voltages for different device sizes

Even though the devices containing micropipes, grain boundaries and triangular defects also contain SSDs and TEDs, the effects of these additional defects on device performance could be tentatively explored. Table 2 lists the correlation between the defect densities and the breakdown voltages of the related devices.

Table 2. Summary of the effects of various defects on breakdown voltages in the studied wafer

Defect type	Defect density	Median $V_{breakdown}$ (V)
Threading edge dislocations [a]	1.9×10^4 cm^{-2} (42)[e]	604 (42)[e]
Small screw dislocations [a]	6.3×10^3 cm^{-2} (42)	566 (42)
Micropipes [b]	1 /device (16)	308 (16)
Grain boundaries [c]	5 cm^{-1} (11)	314 (11)
Triangular defects [d]	1 /device (5)	130 (5)

[a] Devices chosen only contain SSDs and TEDs.
[b] Devices chosen only contain SSDs, TEDs and MPs.
[c] Devices chosen only contain SSDs, TEDs and GBs.
[d] Devices chosen only contain SSDs, TEDs and TDs.
[e] Numbers in parentheses represent the numbers of devices from which the averages are obtained.

TEDs and SSDs are much more densely distributed in the devices than other defects, but they have less effect on the breakdown behavior. On the contrary, despite the much lower densities, MPs, GBs and especially TDs influence device performance far more significantly than TEDs and SSDs. Micropipes have been well documented to degrade device performanc. However, few papers have reported the influence of GBs on SiC devices. The GBs in the present sample comprise continuous rows of TEDs or BPDs. Whereas individual TEDs have a small influence on device performance, tightly spaced arrays such as in a grain boundary are proposed to be much more harmful. Although they have the lowest density, TDs have the most profound effect on device performance. The much lower breakdown voltages in devices

having TDs were proposed to result from the fact that the 3C structure has a lower barrier height than the 4H structure. In general, MPs, GBs and TDs are highly detrimental to device performance.

Conclusions

Small screw dislocations and threading edge dislocations are the most common defects observed in the devices studied. As their densities increase, the device performance deteriorates. On the other hand, while micropipes, grain boundaries and triangular defects were much less commonly observed, they drastically degrade the device performance.

Appendix II Conversion between the stereoprojections of rhombohedral system and hexagonal system

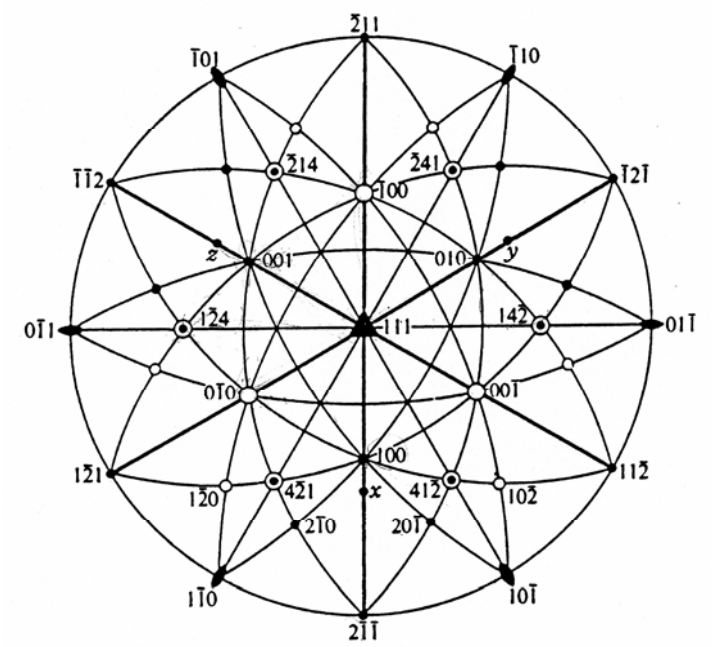

Stereo projection of rhombohedral system

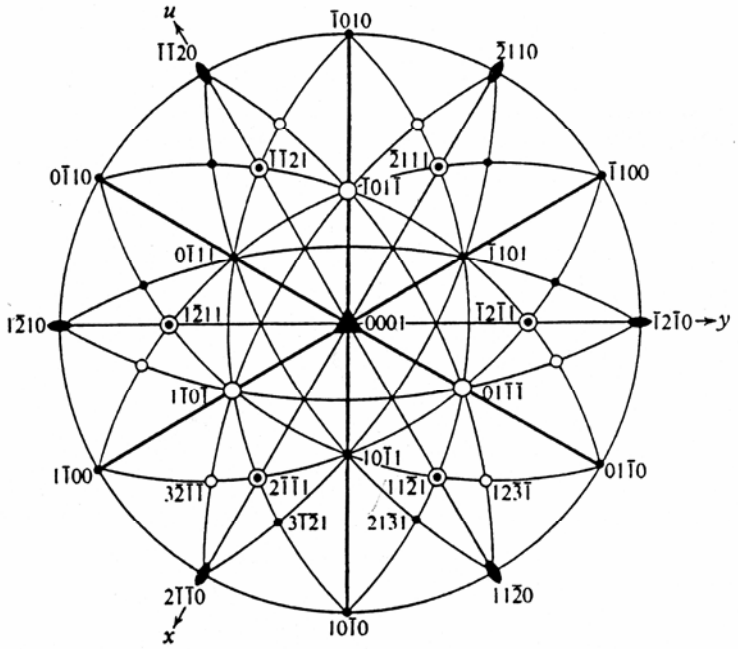

Stereo projection of hexagonal system

Appendix III Unit cells of $B_{12}As_2$, 6H-SiC and 15R-SiC generated by CaRine4.0

1. $B_{12}As_2$

a	b	c	
5.3370	5.3370	5.3370	(Å)

α	β	γ	
70.216	70.216	70.216	(°)

Atom	X	Y	Z	Occupation
As	0.39999	0.39999	0.39999	1
As	0.60001	0.60001	0.60001	1
B	0.8208	0.8208	0.2755	1
B	0.2755	0.8208	0.8208	1
B	0.8208	0.2755	0.8208	1
B	0.1792	0.1792	0.7245	1
B	0.7245	0.1792	0.1792	1
B	0.1792	0.7245	0.1792	1
B	0.9826	0.9826	0.6755	1
B	0.6755	0.9826	0.9826	1
B	0.9826	0.6755	0.9826	1
B	0.0174	0.0174	0.3245	1
B	0.3245	0.0174	0.0174	1
B	0.0174	0.3245	0.0174	1

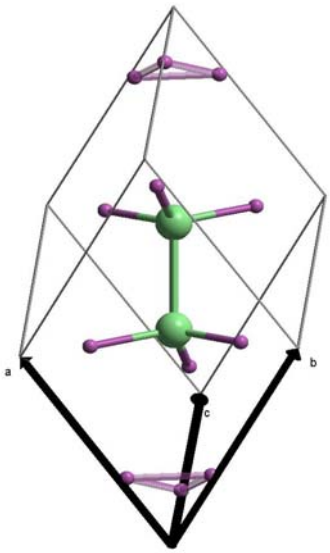

2. 6H-SiC

a	b	c	
3.0806	3.0806	15.1173	(Å)

α	β	γ	
90	90	120	(°)

Atom	X	Y	Z	Occupation
C	0	0	0.125	1
C	0	0	0.625	1
C	0.333333	0.666667	0.458333	1
C	0.333333	0.666667	0.791667	1
C	0.666667	0.333333	0.958333	1
C	0.666667	0.333333	0.219667	1
Si	0	0	0	1
Si	0	0	0.5	1
Si	0.333333	0.666667	0.333333	1
Si	0.333333	0.666667	0.666667	1
Si	0.666667	0.333333	0.166667	1
Si	0.666667	0.333333	0.833333	1

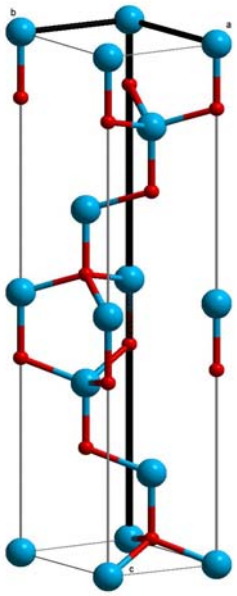

3. 15R-SiC

a	b	c	
12.69	12.69	12.69	(Å)

α	β	γ	
13.917	13.917	13.917	(°)

Atom	X	Y	Z	Occupation
Si	0.00000	0.00000	0.00000	1
Si	0.13333	0.13333	0.13333	1
Si	0.40000	0.40000	0.40000	1
Si	0.60000	0.60000	0.60000	1
Si	0.86667	0.86667	0.86667	1
C	0.05000	0.05000	0.05000	1
C	0.18333	0.18333	0.18333	1
C	0.45000	0.45000	0.45000	1
C	0.65000	0.65000	0.65000	1
C	0.91667	0.91667	0.91667	1

Appendix IV Simulated selective area diffraction (SAD) patterns of $B_{12}As_2$ along various zone axes

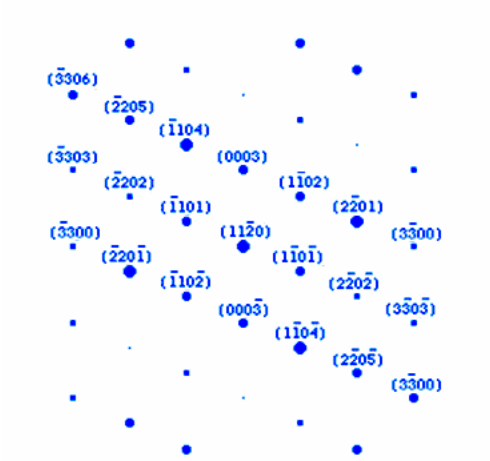

(11-20) SAD pattern

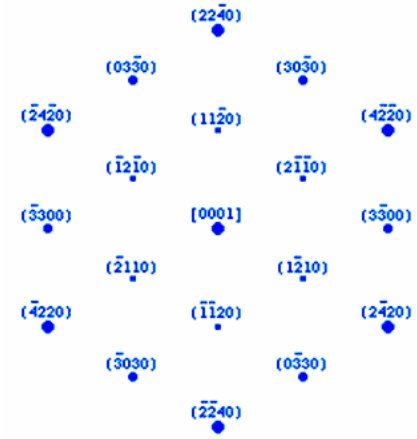

(0001) SAD pattern

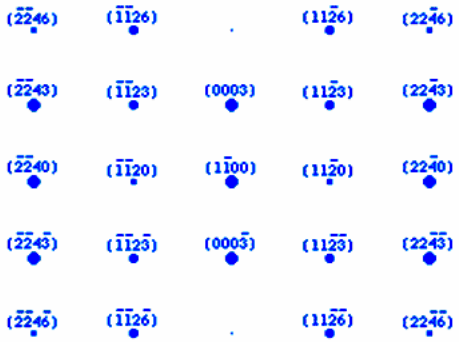

(1-100) SAD pattern

Appendix V Stereoprojections of $B_{12}As_2$

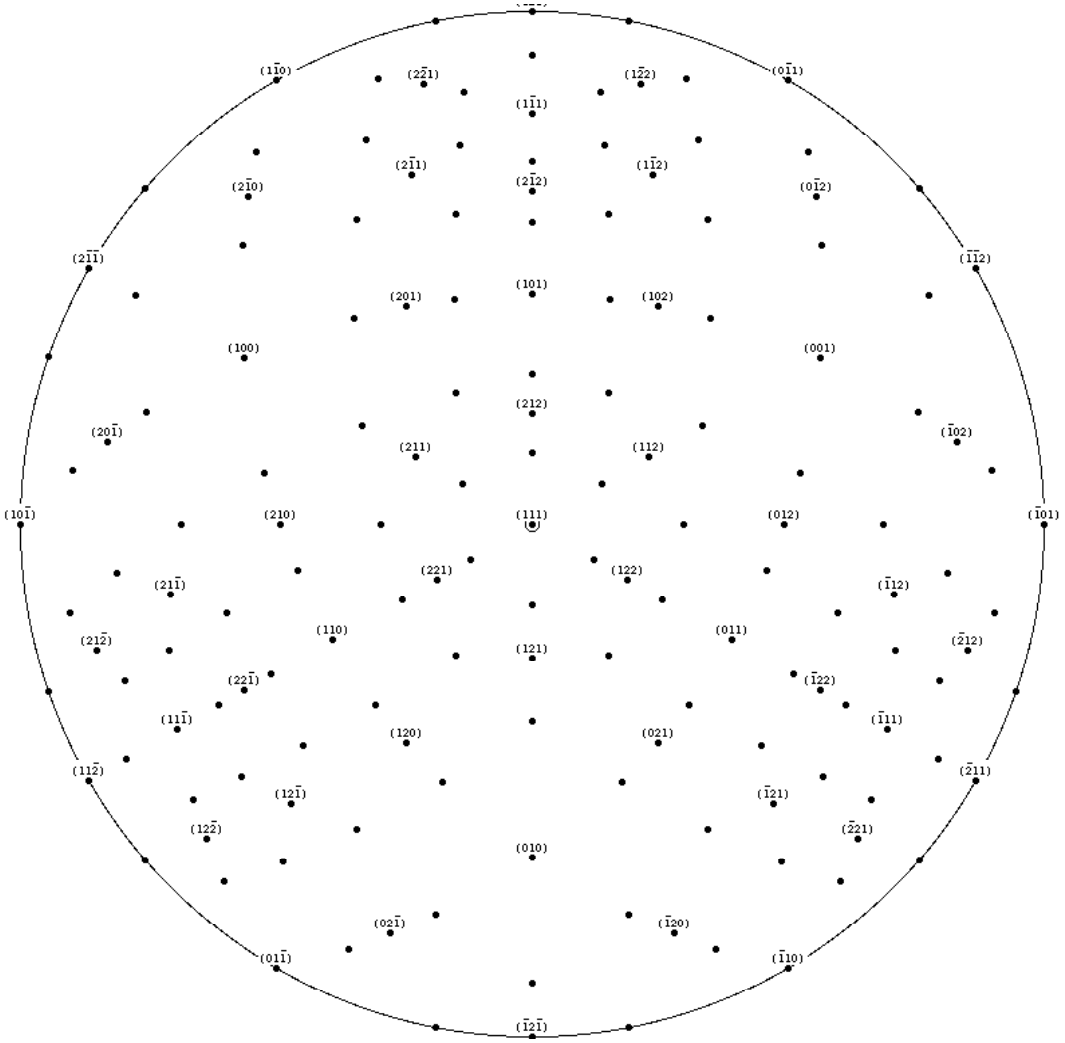

(111) stereo projection

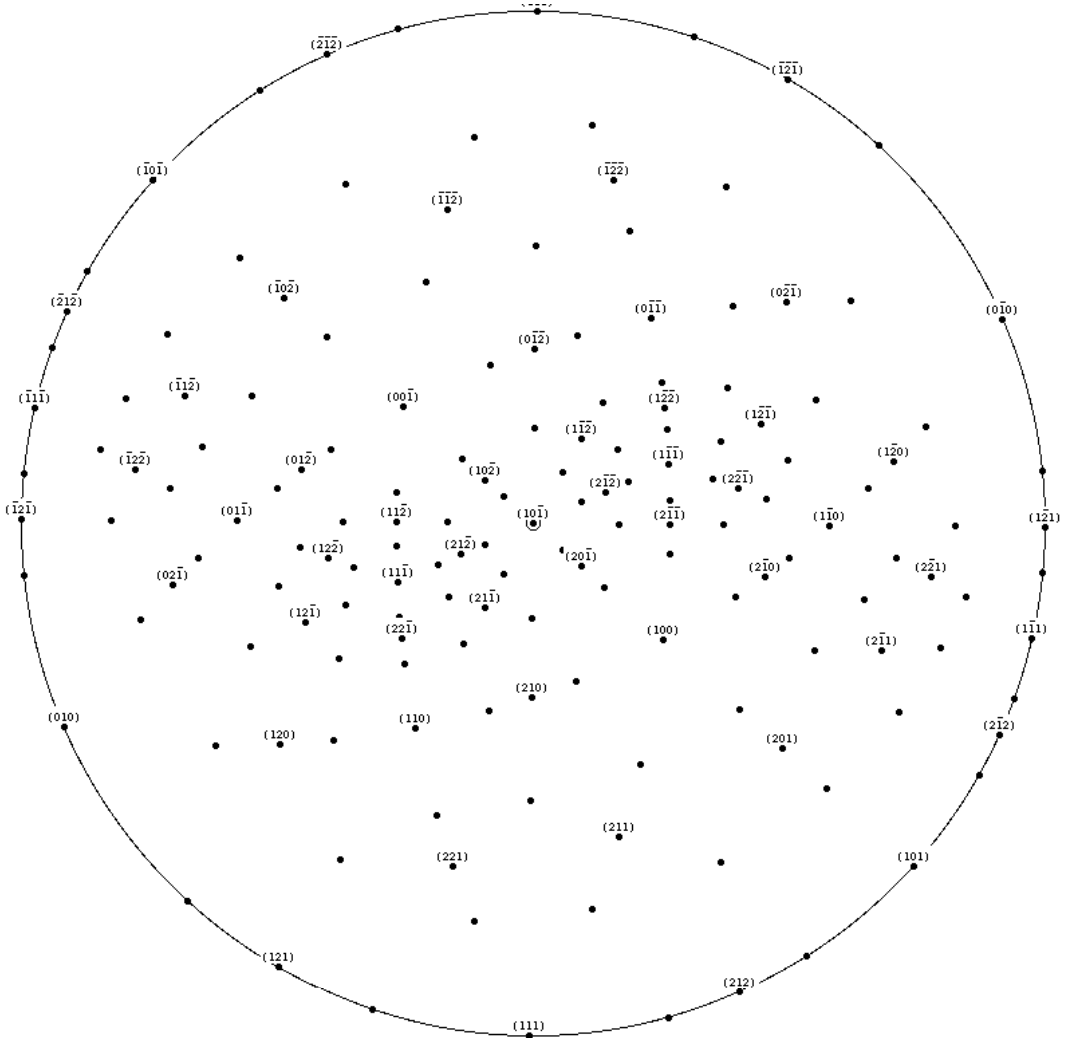

(10-1) stereo projection

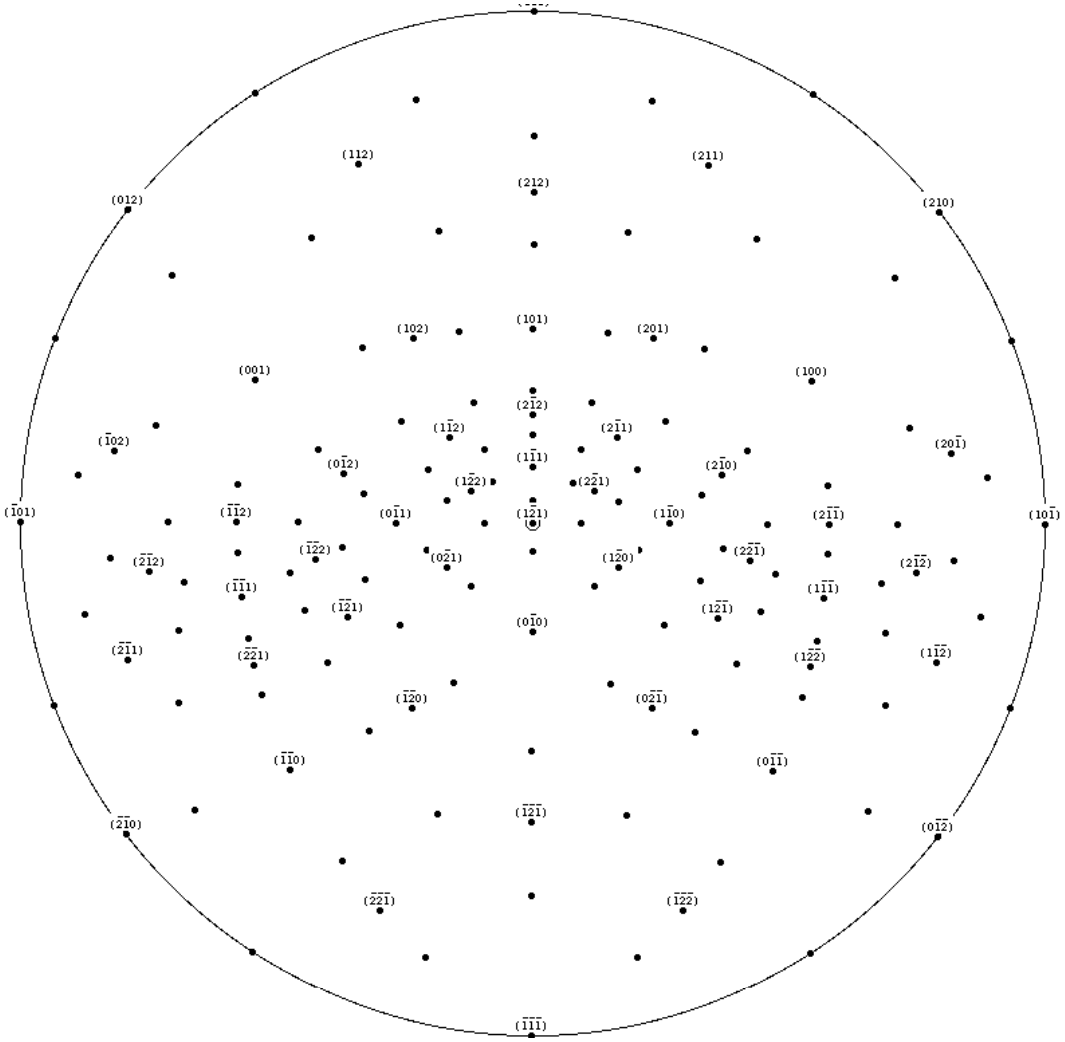

(1-21) stereo projection